# Development of remote monitoring system of rainfall-induced lahar at Mount Merapi

MAGFIRA SYARIFUDDIN

Kobe University

# Doctoral Dissertation

# Development of remote monitoring system of rainfall-induced lahar at Mount Merapi

メラピ山における降水起源ラハールの遠隔監視システムの開発に関する研究

January 2018

Graduate School of Engineering,
Kobe University

MAGFIRA SYARIFUDDIN

# ABSTRACT

Debris flow in the slope of volcano happens not only by the effects of melting water but also by the overflow of crater-lake or by the flood runoff of severe rainfall. This event is sometimes called "lahar", which is a wet mass of volcanic fragments flowing rapidly downhill. At Mt. Merapi of Indonesia, lahar occurs mostly as secondary disasters that happens almost every year during the rainy season. The lahar monitoring in this area mainly consists of some ground-based measurement by several instruments: seismograph, wire sensor installed at river perimeter, automatic water level recording (AWLR), automatic rain gauges, and video camera. Although the operation of those instruments is useful for precise lahar monitoring, the risks carried in an active volcano caused those instruments were unable to monitor lahar happened following the eruption in 2010.

The occurrence of lahar in several volcanoes in Indonesia is strongly related to the rainfall. At Mt. Merapi, lahars are commonly triggered by rainfall having an average intensity of 40 mm in 2-hours. It usually occurs in the rainy season from November to April. During the rainy season after 2010 Mt. Merapi eruption, more than 50 lahars happened in the rivers at Mt. Merapi. The frequency of post-eruptive lahars (cold lahars) depends on the rainfall characteristics and the total volume of the grain size distribution of fresh volcanic deposits.

The study of lahar has two main problems. The first problem is lahar usually generates in a relatively inaccessible and dangerous area at an elevation higher than 1200 m above mean sea level (amsl). This problem causes difficulties on direct lahar monitoring. The second problem is the uncertainty of rainfall data at Mt. Merapi. This problem is causes by the unavailability of upstream rainfall information, great spatial distribution of rainfall, and the potency of destructive eruption impacts from an active volcano.

This study was conducted to solve those problems by developing a remote monitoring system of lahar by the utilization of X-band multi-parameter (X-MP) weather radar and a numerical hydraulic model. The application of X-MP radar is able to give a more reliable and wider coverage area of real-time rainfall and lahar potency information at Mt. Merapi. Several activities were conducted to develop the remote monitoring system of lahar, which are (1) Applying a graphical user interface of a numerical model of debris flow to simulate lahar at Mt. Merapi; (2) Integrating rainfall data estimate by X-MP radar to optimize the numerical model of lahar performance; (3) Applying an ensemble short-term rainfall prediction to the critical rainfall of lahar to know the potency of lahar occurrence; (4) Improving a distributed hydrological model performance by integrating X-MP radar rainfall, modifying the flow stoppage mechanism and applying some lahar empirical equations to simulate lahar flow; and (5) Applying the predicted rainfall values to a distributed hydrological model for lahar flow simulation based on a real lahar event.

The HyperKANAKO model, a debris flow simulator equipped with a graphical user interface (GUI) was used to simulate the lahar flow at Mt. Merapi. The objectives were to get the best

resolution of digital elevation models (DEMs) for lahar simulation and to understand the effect of rainfall to the lahar initiation and magnitude. Three DEMs resolution levels and two rainfall data measured by rain gauge in the Gendol catchment were used. The simulation found that one-dimensional (1D) flow was more affected by rainfall than DEM quality, while two-dimensional (2D) lahar flow were best simulated by using the finest resolution at 5-m mesh.

Simulation was improved by applying the X-MP radar data to the HyperKANAKO model for a simulation of a real lahar event in Gendol catchment on 17 February 2016. A lahar happened in the upstream region of the Gendol River on the southeastern flank of Mt. Merapi after a maximum rainfall intensity of 69 mm/h was monitored on the peak of Mt. Merapi by X-MP radar. The rainfall intensity estimates from X-MP radar were applied to generate boundary discharge of a numerical model of debris flow at the catchment scale. The numerical simulation was able to estimate volcanic debris flow occurrence and magnitude. The radar showed good reliability to ground measurement, even so, the attenuation was suspected on rainfall observation. The numerical lahar simulation showed relevant results that were comparable to the real condition. Thus, it demonstrated the effectiveness of remote monitoring of rainfall combined with numerical debris flow modeling for applied practical use in disaster management.

A short-term analysis of lahar potency was proposed by applying mean values of predicted rainfall from an ensemble rainfall forecasting to a snake line analysis. Real-time lahar estimation requires an earlier rainfall information. An ensemble rainfall forecasting was applied to the same day event. The predicted rainfall values still had poor spatial distribution, but in general, the average areal rainfall were in agreement with real observed data. A further application to the snake line analysis could determine the potency of lahar occurrence. The plotting resulted in the snake line exceeded the critical line and hence indicated the potency of future rainfall to trigger the lahar in Gendol catchment.

Applying the mean ensemble forecast rainfall to a hydrological model of Rainfall-runoff and inundation (RRI) model, earlier lahar information could be obtained. The potency of lahar is analyzed by applying the mean ensemble predicted rainfall to the snake line analysis. The RRI model was modified by giving more resistant to the flow in the discharge formula by adjusting the Manning roughness coefficient and integrating some empirical equations of lahar properties. This study becomes the first study to couple the rainfall information from X-MP radar for distributed lahar model. The Manning coefficient roughness adjustment was applied to each of the stream cell in the terrain data. It caused the flow to have higher shear stress in the flatter elevation, hence acted as stoppage mechanism. The mean-ensemble rainfall-based model gave the same simulation results with the observed X-MP radar data-based model. The validation of the water depth from the simulation of X-MP radar based models and means ensemble based model were also in agreement with the measured water depth. On the other hand, the rain gauged-based model gave overestimation results. The calibration in the Putih catchment also showed the superiority of X-MP radar comparing to the ground-based measurement.

Overall the present framework offered suggestions for better treating the uncertainty of lahar disaster based on hydro-meteorological condition and thus could serve as reliable and effective

system for better remote lahar monitoring. The key research outcomes that allow the system to be delivered are

1) The procedure and requirements of remote lahar simulation based on rainfall condition and terrain data information
2) The practical use of X-MP radar rainfall for giving better spatial information on remote monitoring technique of lahar at a catchment scale
3) The faster and earlier analysis of lahar potency by applying the short-term rainfall prediction into snake line analysis
4) The framework of remote hydro-meteorological analysis and modeling of volcanic area for lahar occurrence simulation.

This study is an initial attempt to introduce the effectiveness of X-MP radar for lahar analysis and the procedure of remote lahar monitoring. Although the proposed method still has some limitations in understanding the physical properties of lahar, it can give lahar properties information efficiently; which is important in disaster mitigation and adaptation. In the future, better understanding on rainfall characteristic at Mt. Merapi by analyzing more cases of lahar occurrences should be done parallel to the development of better lahar mechanistic model.

# TABLE OF CONTENTS

## Chapter VII Application Example for the Proposed Method

## Chapter VIII Summary and Future Work

# LIST OF FIGURES

# LIST OF TABLES

# CHAPTER 1
# INTRODUCTION

## 1.1 Background of the study

Before 1964, among human victims of total water-related hazards, 32% happens due to sediment disaster. Since 1965, this percentage has increased to approximately 50% (Takahashi, 2009). Amongst all of the sediment disasters, debris flows are the most frequent natural hazards, especially in mountainous, volcanic, semi-arid, and sub-polar regions (Santi et al., 2011; Takahashi et al., 1981). Debris flows cover wide range of sediment movement events include debris torrents, debris floods, mudflows, mudslides, mudspates, hyper-concentrated flows, and lahars. In principle, the flows involve the interaction between solid and fluid particles, which plays an important role on the mechanism of the flow process (Iverson, 2010).

Volcanic debris flow or lahar is an Indonesian word that is defined as a rapidly flowing, high-concentration, and poorly sorted sediment-laden mixture of rock debris and water from a volcano, that is usually triggered by rainfall. It belongs to a continuum flow type, which covers debris flows, hyper-concentrated flows, and mudflows (Lavigne et al., 2007; Neal, 1976). Typically, lahar flows enter a river valley at a velocity of 2.5−11 m/s (Lavigne et al., 2007).

Lahar flow includes the direct and indirect effects of the eruptions. The direct one is the hazard happens created by some large eruptions (Major et al, 2000). The indirect or secondary lahar is also known as the post-eruption lahar. The secondary lahar can occur even without an eruption and the initiation is a function of rainfall parameters, source material characteristic, and time since eruptive activity (Jones et al., 2017).

Between 17th to 19th centuries, lahars are responsible for 17% of deaths due to the volcanic disasters, especially in Indonesia. In the 20th century, lahar takes a toll of 31,500 victims from two deadly disasters at Mount Kelud (1919) in Java and Nevado del Ruiz (1985) in Colombia (Lavigne et al., 2007). Lahar and pyroclastic flow contribute to the highest rate of erosion in the world ($10^5$-$10^6$ $m^3$ $km^{-1}$ $yr^{-1}$) (Milliman and Syvitski, 1992; Major et al., 2000).

The precise timing of lahar events is unpredictable and working with active flows can be hazardous. This problem makes much of present knowledge of lahar flow behavior is inferred

from the study of lahar deposits. Lee et al. (2015) simulates lahar deposition based on the satellite image and LAHARZ model, without considering the involvement of rainfall within the process. Lavigne and Thouret (2003) discusses the sediment yield of lahar in the downstream area of Mount Merapi by using rainfall information derived from rain gauges. More studies have been invested in studying critical rainfall leads to lahar initiation (Fitriyadi, 2009; Yulinsa, 2015; Fibriyantoro, 2015), but most of them rely on rainfall information in the downstream, which do not represent the direct effect of rainfall in the upstream.

At Mt. Merapi of Indonesia, lahar occurs mostly as secondary disasters that happens almost every year during the rainy season (Lavigne et al., 2002). The lahar monitoring in this area mainly consists of some ground-based measurement by several instruments such as seismograph, wire sensor installed at river perimeter, automatic water level recording (AWLR), automatic rain gauges, and video camera (Lavigne et al., 2000a; Legowo, 1981). Although the operation of those instruments are useful for precise lahar monitoring, the risks carried in active volcanoes caused those instruments to be unable to monitor lahar occurrences following the eruption in 2010 (Hardjosuwarno, 2014).

The development of simulation techniques in recent years has allowed lahar modeling and simulation to be an assessment tool for understanding the debris flow and lahar behavior. The simulation technique helps to understand debris flow process by studying the geologic settings, triggering mechanisms, transport processes, and deposition characteristics (Castrucci and Claverro, 2015; Jones et al., 2017; Procter et al., 2010). Nevertheless, the application in the catchment scale is still limited.

Lahar occurrences happen mostly under severe rainfall intensity and significantly increase during the rainy season. Thus, rainfall information becomes the fundamental element for lahar model application in the catchment-scale studies (Jones et al., 2017; Castruccio and Claverro, 2015). However, the study of lahar has two main problems. The first is that lahars usually occur at higher than 1200 m amsl elevation (Legowo, 1981), whereas most rainfall monitoring instruments are available only at lower elevations. The second problem is that lahars following an eruption are usually initiated in a relatively inaccessible and dangerous area, making the direct verification difficult (Nikolopaulus et al., 2014; Staley et al., 2013).

Recent studies have shown the effectiveness of remote monitoring; such as by weather radar, for debris flow estimation and risk management. Weather radar provides finer spatial and

higher temporal resolution of rainfall, which is desirable for debris flow and lahar studies. It offers the advantage of being able to monitor rainfall in the area where lahars initiate (Chiang and Chang, 2009; David-Novak et al., 2004). Marra et al. (2014) confirm that the scarcity of rain gauges has resulted in the underestimation of the rainfall threshold for debris flow occurrence, and weather radar performs well for monitoring debris flow occurrence during short-duration convective storms.

Furthermore, population growth has driven development further to the debris flow prone areas (Jakob and Hungr, 2005). In Indonesia, an old paradigm of living together with disaster is still alive in volcanic areas especially Mt. Merapi. The people who live in this area are at extreme risk from the regular eruption and frequent secondary lahar events. Although they have understood the consequences of living in the hazard area, the disaster awareness remains an important issue. Hence, a non-structural countermeasure by a system developed to monitor the rainfall and the potency of lahar occurrences is urgently required.

## 1.2 Objectives of this study

The objective of this research is to develop a real-time lahar monitoring system at Mt. Merapi by the utilization of the X-MP radar into a distributed hydrological model. The main objective is obtained by conducting these activities:

(1) Applying a graphical user interface of a numerical model of debris flow to simulate lahar at Mt. Merapi;

(2) Integrating rainfall data estimate by the X-MP radar to optimize the numerical model of lahar performance;

(3) Applying an ensemble short-term rainfall prediction to the lahar critical rainfall lahar potency analysis;

(4) Improving a distributed hydrological model performance by integrating X-MP radar rainfall, modifying the flow stoppage mechanism, and applying some lahar empirical equations to simulate lahar flow; and

(5) Applying the mean-ensemble prediction of rainfall to a modified distributed hydrological model for lahar flow simulation based on a real lahar event.

## 1.3 Research methodology

This study aims to develop a lahar assessment system based on rainfall data and the terrain data information/Digital Elevation Model (DEM). Hence, the first step is to apply rainfall data from rain gauge as the triggering force to get the discharge data, which is used as the boundary condition in a debris flows numerical model. The discharge then combine with several different quality of DEMs as the inputs in a lahar simulation model. This step reassures the relationship between lahar, rainfall, and the optimum resolution of the spatial data (**Chapter III**).

Next, the improvement on lahar simulation is done by integrating X-MP radar data to calculate the discharge in the upstream area of Mt. Merapi. This chapter also discusses the reliability of rainfall measured by rain gauges and X-MP radar (**Chapter VI**).

Short-term rainfall condition is predicted by an ensemble rainfall prediction model. This step aims to know the potency of predicted rainfall to be used on a short-term lahar assessment. It is done by the snake line analysis to determine earlier lahar potency information (**Chapter V**).

The last part is a direct application of X-MP radar to a distributed hydrological model. Lahar properties are calculated based on empirical equations (**Chapter VI**). The mean ensemble prediction of rainfall is used as the input to the modified distributed lahar model to get real-time lahar information at Mt. Merapi. The simulation is done following a real lahar event (**Chapter VII**). **Figure 1.1** describes these steps in a chart.

## 1.4 Organization of the dissertation

The following chapters of this dissertation elaborate the problems and methodology adopted to discuss the remote monitoring system of lahar at Mt. Merapi (**Figure 1.2**). This dissertation consists of 8 chapters, outlined as follows.

**Chapter I     Introduction**

This chapter gives the background of the study, the research objectives, and the structures of the thesis.

**Chapter II     Basic concept and site description**

This chapter explains various kind of sediment transport, debris flow definition, the profile of Mt. Merapi and its eruption, lahar definition, and lahar mechanism.

**Chapter III**    **Debris flow model by a single-phase continuum approach**

This chapter explains the physics of debris flow from several approaches: Newtonian fluid, Bingham fluid, and dilatant fluid model. An application from a numerical model based on dilatant fluid rheology is also presented.

**Chapter IV**    **Integrating X-MP radar for lahar simulation**

This chapter explains the utilization of remote monitoring of lahar by X-MP radar and a numerical model of debris flows. Exsisting lahar monitoring system and the advantageous of X-MP radar are also discussed.

**Chapter V**    **Short-term rainfall prediction at Mt. Merapi**

This chapter discusses an ensemble rainfall prediction at Mt. Merapi and its application to the snake line analysis and the critical rainfall of lahar to determine the lahar occurrence.

**Chapter VI**    **Lahar assessment at Mt. Merapi by a distributed hydrological model**

This chapter explains a modification of a distributed hydrological model to perform as numerical lahar model. The modification done by assuming lahar as a turbulent hyper-concentrated flow, which resulted in more friction applied to the flow. The system also includes empirical equations to estimate lahar properties.

**Chapter VII**    **Application example for developed system**

In order to evaluate the developed system, an application by combining the ensemble short-term rainfall prediction and the modified hydrological model for rainfall triggered lahar analysis is done in two rivers: Gendol and Putih Rivers.

**Chapter VIII**    **Summary of the study**

This chapter summarizes the study with conclusions, finding, and the outlook for further studies.
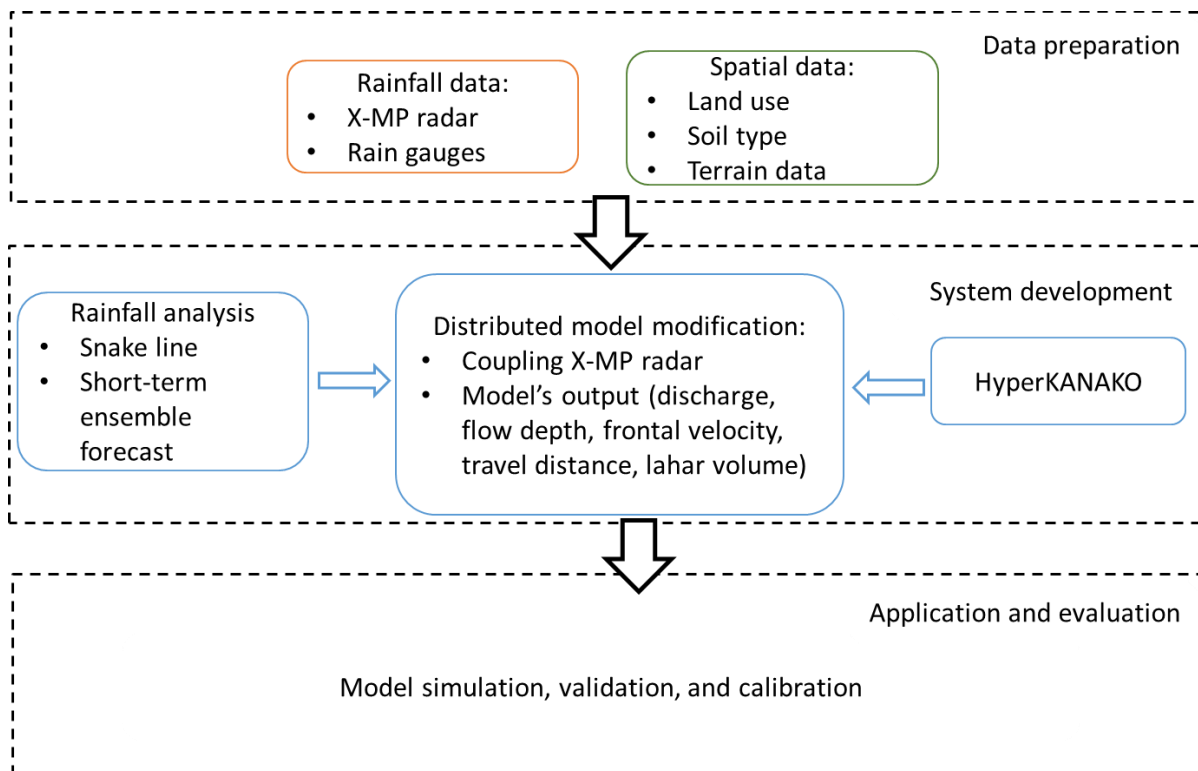
**Figure 1.1** The major steps and approach for developing remote monitoring of real-time lahar estimation at Mt. Merapi.
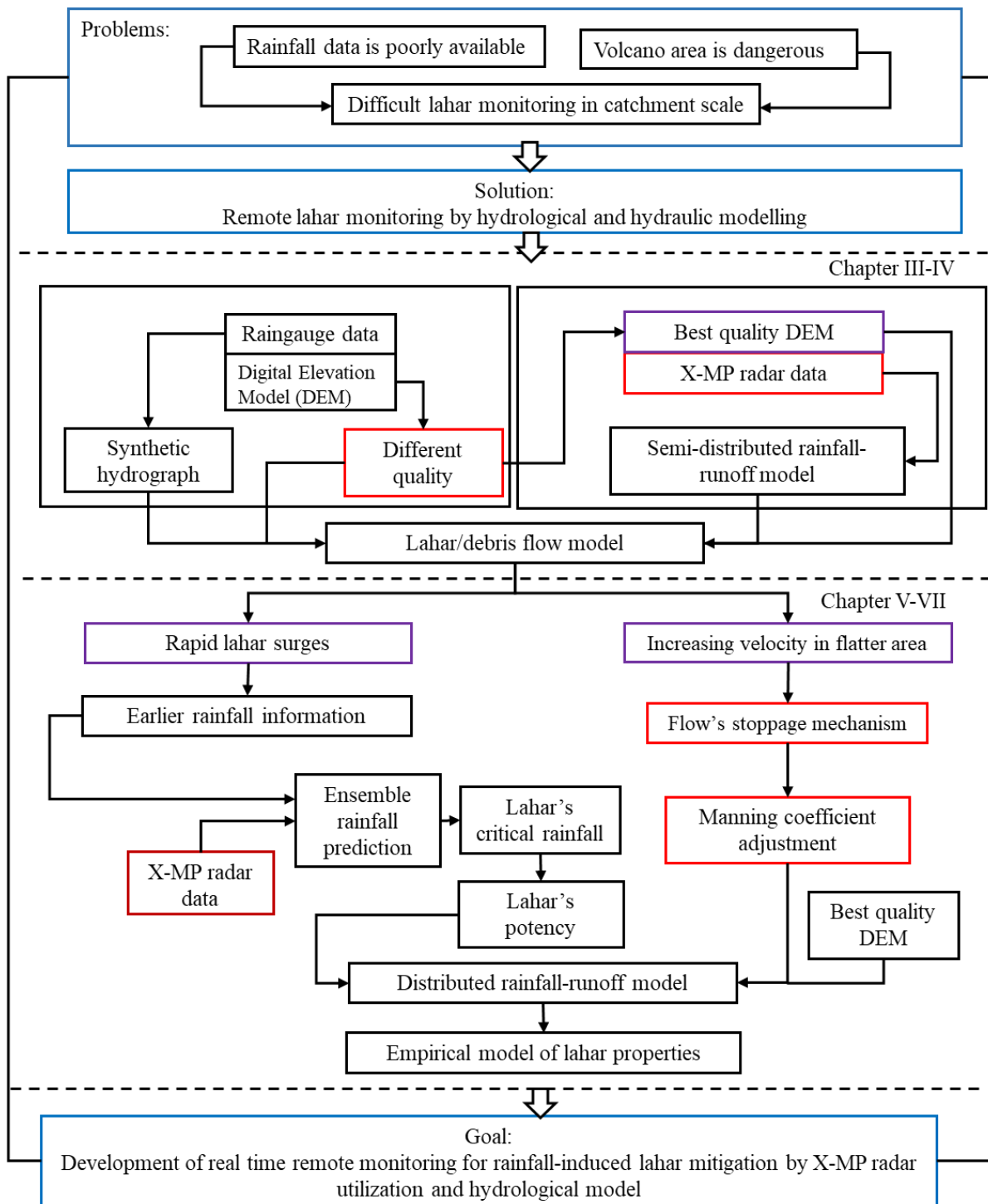
**Figure 1.2** Problems identification and the research frame goals.

# CHAPTER II
# BASIC CONCEPT AND SITE DESCRIPTION

## 2.1 Sediment Related Disasters

The classification of the flowing sediments is primarily based on relative, qualitative differences in the style and rate of the movement, and as well in the morphology and sedimentology of deposits. In terms of sediment transport on the earth-surface slope, relative velocity and relative concentration are considered to differentiate a suite of flow processes. Takahashi (2014) classifies this sediment transport into two types of flow. The first type is the gravity driven and moved altogether and the second type is driven by fluid dynamic forces and moves as an individual particle motion. The second type includes bed load, suspended load, and wash load in river flows. In general, sediment transportation could take in one of the following forms:

a. landslide and landslips,
b. debris avalanches,
c. pyroclastic flow,
d. debris flow and immature debris flow (**Figure 2.1**).

Landslide and landslip happen when the gravitational mass of rock, debris, or earth move downslope. The debris avalanche is a term to describe the large-scale collapse of a mountain body that reaches distant flat areas of a low slope. The pyroclastic flow is a dry granular flow produced by the collapse of a lava dome (Takahashi, 2014). While the third group is in contrast to the other flows, severe rainfall intensity is the major triggering cause of landslide, debris avalanche, and debris flows happen in the mountainous area (Chen et al., 2013).

In many studies (Cannon, 1988; Chen and Chuang, 2014; Corominas and Moya, 1999), a landslide was identified as one of the factors to induce debris flow. Three landslides happened after Typhoon Morakot and triggered debris flows in southern Taiwan in 2009 (Chen and Chuang, 2009). Although it can be the source of debris flow, the physical properties and flow deformation of a debris flow are indeed different with the landslide and debris avalanche.
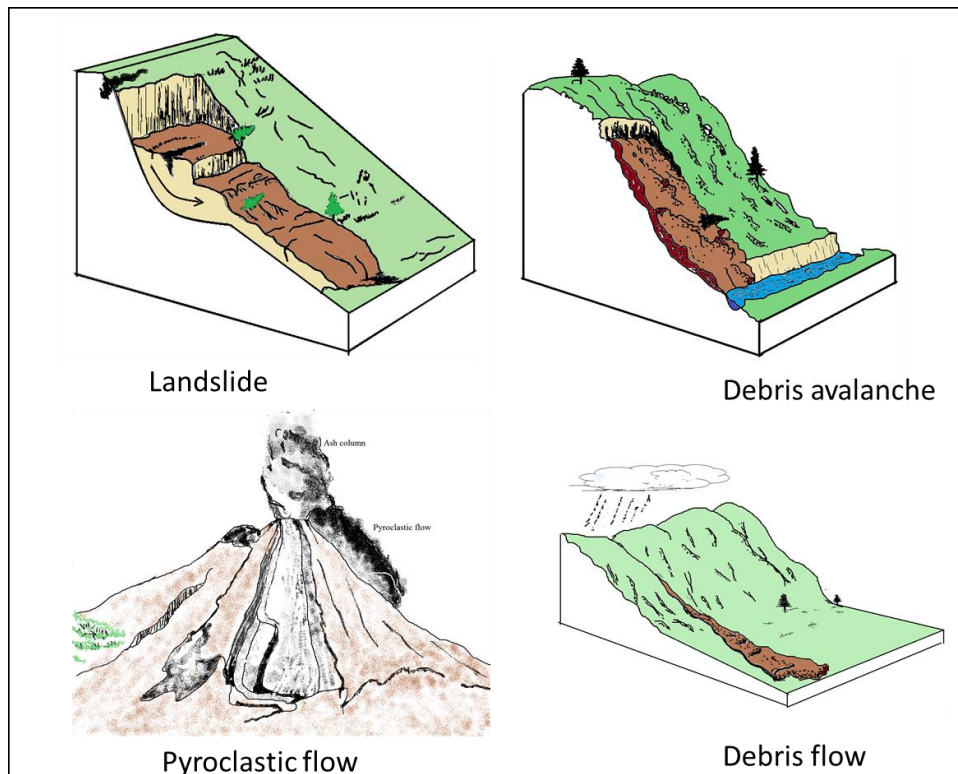
**Figure 2.1** Classification of sediment transportation on the earth surface. Images are redrawn from United States Geological Survey, USGS (https://pubs.usgs.gov/fs/2004/3072/images/), and Global Volcanism Program, Smithsonian Institute for the pyroclastic flow image (https://volcano.si.edu/reports_bgvn.cfm?IssueYear=1996&IssueMonth=09).

The rheology of debris flows is debatable, but most of the studies are in agreement that debris flows contain higher concentration than hyper-concentrated flows (Julien and Leon, 2000; Lavigne and Suwa, 2003). A hyper-concentrated flow is an intermediate flow between fluvial flow and debris flow, which contains sediment concentration about 5-60 % (Pierson, 2005). Hyper-concentrated flows can take forms in the mud floods and mudflows (Julien and Leon, 2000).

Mud floods are typically hyper-concentrations of non-cohesive particles (e.g. sands) flows, which display fluid behavior for the range of sediment concentrations by volume as high as 40%. Mud floods are turbulent and the flow resistance depends on the boundary roughness similar as for the turbulent flows with clear water. At a volumetric sediment concentration of 0.05, the sediment concentration of small particles tends to be uniform than described by Rouse vertical concentration profiles. Increased buoyancy and fluid viscosity reduce the settling velocity of sediment particles (Julien and Leon, 2000).

Mudflows are characterized by a sufficiently high concentration of silts and clays (sediment size < 0.0625 mm). The high concentration of both particles changes the properties of the fluid matrix and help support rage clastic material. Mudflows behave as highly viscous fluid mass, where the high concentration makes rafting boulders near the flow surface. Based on laboratory results, the volumetric sediment concentration of a mudflow fluid matrix ranges from approximately 45 % to 55 % (O'Brien, 1986). Mudflows exhibit high viscosity and yield stress. They can travel long distances on mild slopes at slow velocities to and leave lobate deposits on alluvial fans. In this study, the term hyper-concentrated flow represents mud floods and mudflows.

Debris flow is a mixture of the clastic material including boulders and woody debris, where the lubricated inter-particle collision is the dominant mechanism for energy dissipation. Knowledge of debris flow is largely contributed by Bagnold and Takahashi's studies (Bagnold, 1954; Takahashi, 2014; Arattano and Savage, 1994; Hutter et al., 1996). Takahashi (2014) defines debris flow as a flow of sediment and water mixture in a manner as it flows of continuous fluid driven by gravity and attained large mobility from the enlarged void space saturated with water or slurry. The buoyancy acting on particles must have some effects on the large mobility as it can flow even on a gentle slope as flat as 3°. According to Iverson (2014), debris flows are water-laden masses of soil and fragmented rock that rush down mountainsides, funnel into stream channels, entrain objects in their paths, and form lobate deposits when they spill onto valley floors.

Based on those definitions, a debris flow should meet these criterions:
 (1) A two-phase flow consists of poorly sorted fluid and sediment;
 (2) Generally, the volumetric sediment concentration is higher than 55%;
 (3) The entrainment process happens during the flow goes down in the channel and makes it attains large mobility;
 (4) The large mobility keeps it flows even on gentle slope as about 3°;
 (5) The flow will form an alluvial fan of deposits when they spill onto valley floors.

Debris flows are one of the most frequent natural hazards, especially in mountainous, volcanic, semi-arid, and sub-polar regions (Santi et al., 2011). Schuster et al. (2002) concluded that most casualties in Latin America were due to "… high-velocity debris avalanches and high-, to medium-velocity long-runout debris flows and mudflows". Li (2004) reported many lethal and destructive debris flows happened in the mountains of China and placed them among the

most severe sources of damage. Debris flows are one the most commonly reported hazards in the highland areas of New Zealand (Selby, 1993). Nakano (1974) ranked ''mudflows and rocky mudflows'' high among the other damaging mass movements in the mountainous and hilly areas of Japan.

Multiple debris flows happened and destroyed the city's street and houses in Dongchuan, a district of Kunning Yunnan province, Xiaojiang River valley. The total area classified to be in the danger zone was 5.21 km$^2$, which equaled to a total value loss of 488.9 million Yuan (Tiang and Zhang, 2009). Debris flow is an important hazard in Japan for the society and economy (Ikeya, 1989). This phenomenon has been recognized since ancient time and the occurrences during 2000 to 2012 are increasing (MLIT, 2012 in Kim et al., 2014). On 20 August 2014, high intensity of a localized rainfall triggered numerous shallow slides and debris flows in northern part of Hiroshima. These disasters caused 74 deaths, 44 injuries, 133 destroyed houses, and 296 severely damaged houses (MLIT, 2014 in Wang et al., 2015).

Indonesia is subject to many different natural hazards, where sediment disasters include debris flow, landslide, and slope failure are the well-known natural disasters. They are mostly triggered due to the mechanical processes of water, soil, and human activities. In Indonesia, sediment disasters have occurred in both volcanic area (debris flow, lahar flow, landslide, and slope failure) and non-volcanic area (debris flow and landslide).

## 2.2 Debris Flow Classification

In general, criteria for defining debris flows emphasizes sediment concentrations, grain size distributions, flow front speeds, shear strengths, and shear rates (Beverage and Culbertson, 1964; Varnes, 1978; Pierson and Costa, 1987). However, the necessity of the interacting solid and fluid forces makes a broader and more mechanistic distinction. This definition makes many events identified as debris slides, debris torrents, debris floods, mudflows, mudslides, mud spates, hyper-concentrated flows, and lahars may be regarded as debris flows (Johnson, 1984).

The diverse nomenclature reflects the diverse origins, compositions, and appearances of debris flows from quiescently streaming, sand-rich slurries to tumultuous surges of boulders and mud. Based on the appearance, Takahashi (2014) classifies debris flow as stony debris flow, turbulent-muddy type debris flow, and viscous debris flow.

1) Stony-type debris flow

   Stony-type debris flows are common in mountain torrents and in gravel-bedded channel originate in the scree slopes located at the base of rock fall faces. Stony-type debris flows are usually triggered by surface runoff following an intense rainfall event. Hydrodynamic forces destabilize the gravel bed surface, determining the dispersion of sediment grains throughout the entire water depth. Due to the inertia, the large masses of mobilized sediment can travel for long distance and eventually deposit where friction actions prevail, namely for low enough hillslopes, or when discharging in broad alluvial fans and in a less steep channel (Takahashi, 2014).

   In the stony-type debris flows, the distribution of particle sizes consists mainly of boulders, cobbles, and gravels. Finer frictions less than 1 mm are likely contained in the interstitial muddy water, which behaves as a liquid. In any case, a fraction of constituent less than 0.1 mm is far less than in viscous-type and muddy-type debris flows. The dynamic of stony-type debris flow is dominated by grain collision stresses which are responsible for the dispersion of grains throughout the entire water depth (mature flow) and segregation processes (e.g. the accumulation of larger particles on the debris front). The excess of pressure in the pore fluid is likely to play a minor role especially for low grain concentration (Stancanelli et al., 2015).

2) Turbulent-muddy-type debris flow.

   The turbulent-muddy-type usually occurs in volcano area, after the vigorous ejection of ash from an active volcano resulting in the thick of mountain cover that is easily eroded even by a slight rainfall. Such ash cover erosion causes a frequent occurrence of debris flows. This type of debris flow contains many large boulders and mainly comprised of fine ash.

3) Viscous-type debris flow

   In general, viscous-type debris flow is a flow where the dispersion of coarse particles in such dense slurry. The concentration of coarse particles in the slurry is more than 50% by volume. This type of debris flow is characterized by its intermittency, where ten to hundreds of surges (intermittent bore-like flow) come out repeatedly within the time interval of from a few tens of seconds to a few minutes. Each surge rolls on and roars as if it were a breaking wave at the seacoast. The surges are followed by laminar flow part and happen repeatedly which causes bed smoothing and change the width of the channel

and the longitude shapes of the side banks. This flow behavior is recognized by Takahashi (1990) after a long observation in Jiangjia gully in China.

## 2.3 Lahar as a kind of debris flow

Debris flow in the slope of volcano happens not only by the effects of melting water but also by the overflow of crater-lake or by the flood runoff of severe rainfall. This event is sometimes called "lahar", that is an Indonesian genetic form (Takahashi, 2014). Lahar is originally introduced by Scrivenor (1929), in a report of dynamic flows produced by ejection of crater lake water at Kelud volcano in East Java. He translated lahar as "mudstream". Later, Van Bemmelen (1949) expanded the definition as "a mudflow, containing debris and angular blocks of chiefly volcanic origin", but also added, "…volcanic breccias, transported by water".

According to Lavigne et al. (2003) lahar is a Javanese term defined as a rapidly flowing, high concentration, and poorly sorted sediment-laden mixture of rock debris and water (other than normal stream-flow and flood) from a volcano. A lahar is a continuum of flow type, which includes debris flow, hyper-concentrated streamflow, and mudflows. Another definition of the lahar is a class of volcanic mass flows containing a mixture of water and volcaniclastic debris that forms because of the presence of four controlling factors: water, easily entrained debris, steep slopes, and a triggering mechanism (Vallance, 2000).

Based on those definitions, it can be summarized that most scientists agree that lahar can involve a debris flow phase and precursor and warning stage of hyper-concentrated-streamflow phases. The flow behavior exhibits by lahars may be complex but the flow is in contrast with water floods in at least three ways: the flow behavior is unsteady and non-uniform, the capacity of sediment transport is exceptional, and the effects on the valley channel are severe. Hence, several studies have used the numerical model of debris flows to analyze the lahar behavior (Takahashi, 2014; Nagata et al., 2003, Syarifuddin et al., 2016; 2017).

Lahars can be produced in several ways. Primary lahars are syn-eruptive, that is deriving from the pyroclastic flow and surges churning and melting snow and ice, or generated by a crater lake expulsion during the eruptions. Most syn-eruptive lahars are generated in a drainage system, which is buried by a pyroclastic. This leads a series of landslides and debris avalanches that inducing a debris flow (Lavigne et al., 2007).

The majority of lahars are secondary and post-eruptive, which is triggered by rainfall on loose pyroclastic material. In addition, some secondary lahars are not related to the eruptions and less predictable. They occur through processes common to the volcanic terrains after heavy rainfall on a steep slope. Post-eruptive lahar can occur during several years after an eruption. At Mt. Merapi, lahars are commonly rain-triggered by rainfall having an average intensity of about 40 mm in 2-hours, during the rainy season from November to April (Lavigne et al., 2000b).

Lavigne et al. (2000b) conclude that most lahars at Mt. Merapi are invariably initiated by heavy rainfall. During the rainy season after 1994 Mt. Merapi eruptions, more than 50 lahars happens in the rivers at Mt. Merapi. The frequency of post-eruptive lahars (cold lahars) depends on the rainfall characteristics and the total volume of grain size distribution of fresh volcanic deposits.

At Mt. Merapi, rain-induced lahars occur periodically for about 4 years following small to medium-scale eruptions. On average, moderate-sized pyroclastic occurs approximately every 9-16 years and small-scale pyroclastic flows occur every 2-3 years (Shimokawa et al., 1995). Because heavy rainfalls occur every year, rain-triggered lahars are expected to occur almost every year or two in some sectors of Merapi. Lahar occurrence during the 1995-1996 rainy season happens at Mt. Merapi is given in **Figure 2.2**.

At Mt. Semeru in East Java of Indonesia, where the pyroclastic flows are known to happen every 1 to 7 years, lahars take places in form of debris flows and hyper-concentrated flows. During an observation conducted in October 1991 to January 2001, 21 debris flows and 5 hyper-concentrated flows happened in Curah Lengkong Channel, on the southeast flank of Mt. Semeru. Almost all debris flows were triggered by stationary rainfall confined to the upper slopes of Mt. Semeru, whereas hyper-concentrated flows and stream flows were mainly generated by migratory of regional rains driven upwards on the eastern slope. In general, lahars could be triggered by intense rainfall intensity, or low intensity but long duration of rainfall.

Lahars are water saturated, so both liquid and solid interactions determine their unique behavior and distinguish them from other related phenomena common to volcanoes such as debris avalanches and floods. Similar to the viscous-type of debris flows, lahar moves as a surge or a series of surges, driven by gravity, by porosity fluctuation, and by pore fluid

pressures. This kind of flows is in accordance with the Coulomb grain flow model (Iverson 1997). Lavigne et al. (2000) also monitors the presence of at least a surge or two main surges followed by lahar fronts, within few minutes of lahar occurrence in 1995 at Kaliurang, on the southern slope of Mt. Merapi. Those surges show the similarity between lahar behavior and viscous-type of debris flow.
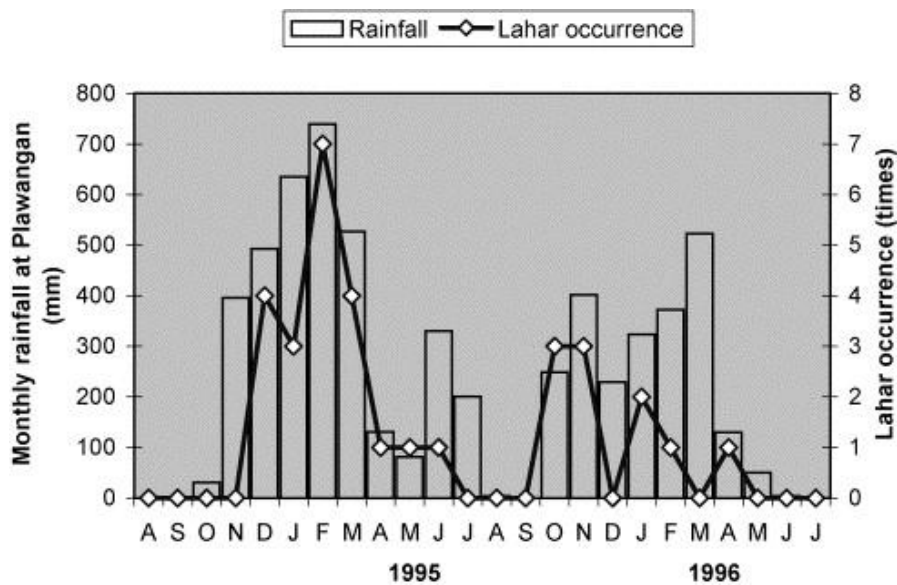


**Figure 2.2** Seasonal rainfall variability and lahar occurrence in 1995-1996 (de Belizal et al., 2013)
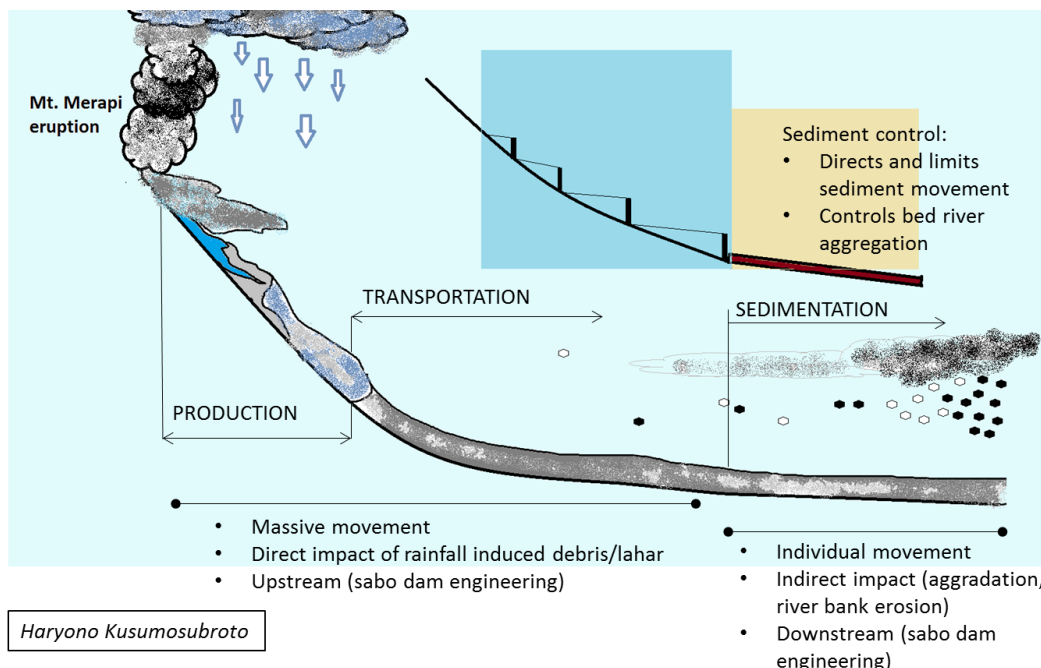


**Figure 2.3** The mechanism of lahar at Mt. Merapi. Image is redrawn and translated from Ministry of Public Work Department of Indonesia

## 2.4 Lahar flow mechanism

The mechanism of lahar occurrence is presented in **Figure 2.3**. The process of lahar flows includes three stages: production, transportation, and sedimentation.

### 2.4.1 Lahar production

The production stage happens in the upstream area after the eruption. Intense rainfall is responsible for triggering lahar initiation. Some studies defined the elevation of lahar initiation is higher than 1200 m amsl, while the other said that at elevation 400 m amsl to 600 m amsl this disaster is still dangerous with flow velocity could be higher than 3 m/s (Legowo, 1980; Lavigne et al., 2000b).

The production and characteristic depend on the volcanic deposits availability. The grain of lahar deposits at Mt. Merapi is dominated by sandy gravel and gravelly sand, which is relatively coarser than other lahar deposits from Mt. Kelud or Mt. Pinatubo. The source material at Mt. Merapi is mainly coarse debris from the block-and-ash flows, hence the remobilization of pyroclastic material in the upper flanks of Mt. Merapi is more difficult than on many other volcanoes.

At Mt. Merapi, most of the debris flows are generated by sheet, rill, and gully erosion in pyroclastic source areas. However, some rare and localized landslide happen on the prior past eruption deposit can also become an additional source of lahar, though the percentage is usually less than 10 % from total lahar volume (Lavigne and Thouret, 2002).

Substantial variations of rainfall intensity over time and space, which is typical of the tropical monsoon climate influences the sediment load variations of the lahars. The rainfall intensity for triggering lahar was said at least 40 mm in 2 hours, while other studies said it is 70 mm/h (Legono, 1981; Wardoyo, 2013). After 2010 eruption, recent studies give different values of this critical rainfall intensity. Kusumawardhani et al. (2017) mentioned the maximum rainfall intensity in Putih River for triggering lahar was at 40 mm/h, while in Gendol River, some debris flows happened at lower rainfall intensity less than 4 mm/h but had more than 100 mm rainfall accumulation (Fitriyadi, 2013). Previous lahars event also showed that lahar could even happen in 5 minutes before/after the peak of rainfall (Lavigne and Thouret, 2003).

2.4.2 Lahar transportation

Generally, lahars at Mt. Merapi have low capacity transport due to the numerous break-in-slope in the river channels. This break-in-slope is influenced by two factors, which are the effect of differential erosion between a lava flow and pyroclastic deposit (upstream area), and the presence of sabo dams (downstream area). This break-in-slope has increase downstream transformation of a lahar from a debris flow to a hyper-concentrated flow and a stream flow (Lavigne and Thouret, 2003).

The sabo dam installation is one of the countermeasures of lahar at Mt. Merapi. The sabo dam presence causes changes in the natural bed surface of the rivers, which affects the transportation process of lahar. There are several types of sabo dams constructed at Mt. Merapi: open-type sabo dam, closed-type sabo dam, and culvert-type sabo dam. The Ministry of public works of Indonesia has built more than 160 sabo dams in the rivers of Mt. Merapi (Ministry of public works of Indonesia in Sumaryono and Hildasari, 2010). An example of a sabo dam at Gendol River is presented in **Figure 2.4**.



**Figure 2.4** Sabo dam Ge-C7 Morangan in Gendol River seen from the northern side (left) and the southern side (right)

2.4.3 Lahar sedimentation

The lahar sedimentation usually comes in stratified deposits, which does not support the hypothesis of the freezing *en masse* deposition process. In the *en masse* deposition process, the flows come to an abrupt halt over its entire depth. In the lahar deposition process, these stratified deposits are caused by the incremental deposition mechanism due to the occurrence of frequent transient, unsteady flows, which transform rapidly from one type to another.

The analyses of the lahar deposits in the Boyong River at Mt. Merapi found that the sediment encompasses clast-supported and matrix-supported debris-flow deposits, hyper-concentrated flow deposits, and streamflow deposits. The stratigraphic succession of massive and stratified beds observed immediately after any given lahar event in the Boyong River indicates that the sediment concentration varies widely over time and space during a single lahar event. Sedimentation rate varies from 3 to 4.5 cm/min during relatively long-lived surges to as much as 20 cm/min during the short-lived surge. The characteristic of this deposition shows that lahar is a kind of transient sediment-water flows with unsteady flow properties.

Analysis of lahar occurrence in 1994-1995 at Boyong and Bedog Rivers, founds that lahar flow stops and deposits at about 820 m amsl with a volume of sediment ranges from $46 \times 10^3$ $m^3$ to $266 \times 10^3 m^3$. The lahars travel averagely at 6.5 km distance from the crater (Lavigne and Thouret, 2002).

## 2.5 Lahars at Mt. Merapi

Mt. Merapi (7.40 S; 110.44 E), is an active stratovolcano located on the border of Central Java and Yogyakarta Provinces, Indonesia. The mountain highest elevation reaches 2957 m amsl, with 13 main rivers drain this volcano (**Figure 2.5**). The word Merapi is actually derived from an Indonesian and Javanese word, which literally means the fire mountain. This mountain is one of the most active volcanoes in Indonesia and has erupted regularly since 1548. Mt. Merapi lies approximately 28 km north of Yogyakarta city, one of the densest populated cities in Indonesia with 2.4 million inhabitants. Thousands of people lived on the flanks of the volcano up to 1700 m amsl.

The destructive *Peléean* type eruption of Mt. Merapi happens every 1000 years. This type of eruption is identified by lava dome growth and collapsed, causing flows of ash and hot blocks, or known as the pyroclastic flows. Almost half of Mt. Merapi's nearly 1980 reported historical eruptions are known to have been accompanied by deadly pyroclastic flow—more than any other volcano (Simkin and Siebert, 1994).

The dome growth and collapsed are the early stage of eruption process, resulting in the volcanic deposits are characterized by more chaotic tephra deposits including poorly bedded and sorted pyroclastic flow and avalanche beds. Tephra or the volcanic material is composited

from fresh magma and lithic clasts with poorly vesicular and blocky structure. The size of blocks and ash grain are usually larger, with mean diameter can be as large as 32 mm (Heiken and Wohlezt, 1987). These pyroclastic flows associate with well-sorted fine layers deposition (ash-cloud surge), which generally thicken downslope and fill the drainage areas.

Some eruptions happened before 1800 are in 1768, 1786, 1791 and 1797. Those explosions were classified as volcanic explosivity index (VEI)-1 to VEI-2, certainly accompanied by new crater deformation and lava dome growth. Volcanic explosivity index (VEI) is an order of magnitude scale ranging from 0 (smaller) to 8 (greater) that often correlates to eruptive types.
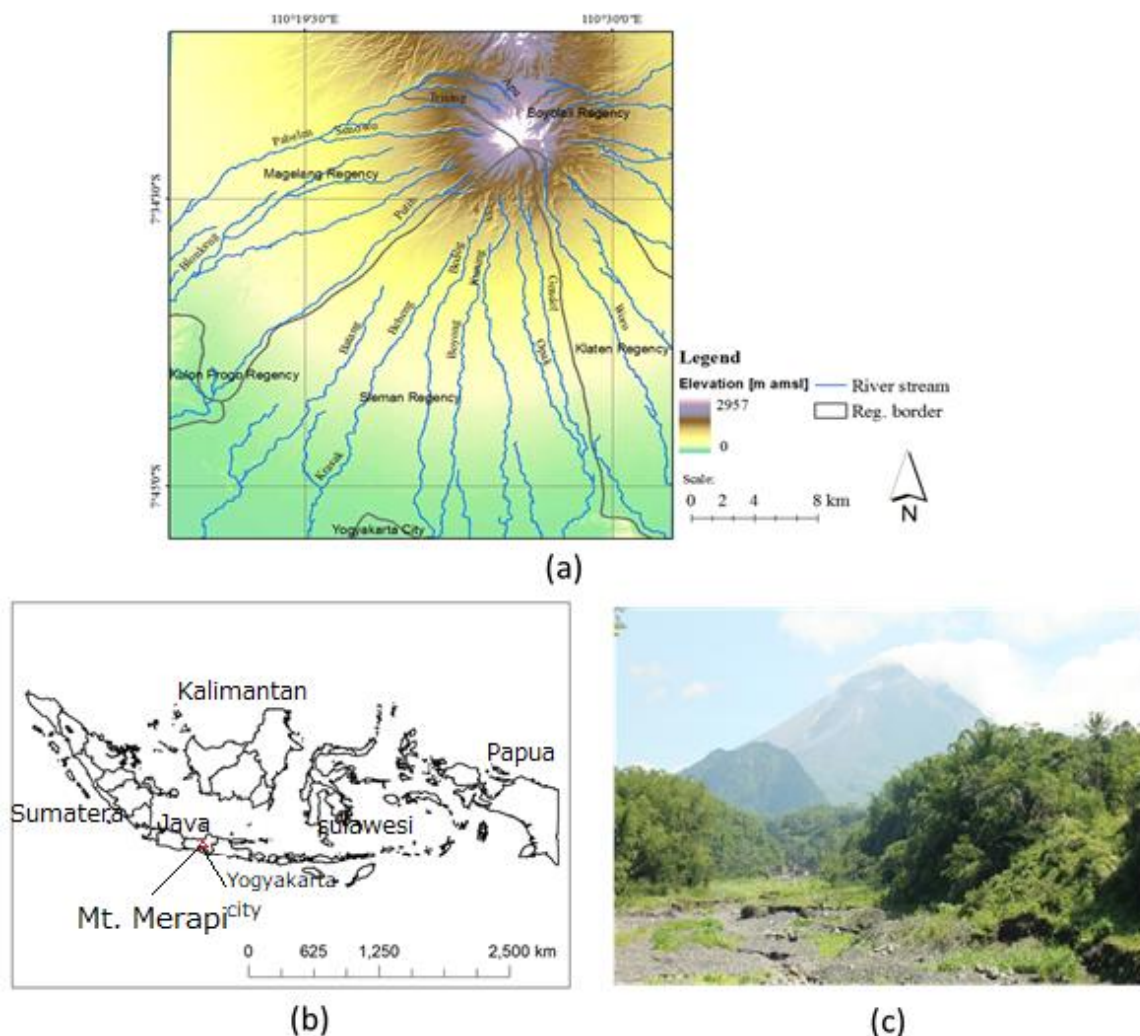


**Figure 2.5** Mt. Merapi and its main rivers (a), Mt. Merapi location in Indonesia (b) and the view of Mt. Merapi seen from Boyong River (c).

Increasing volcanic activity happened in 1800's, with some small eruptions and lava dome growth happened within every two years. The VEI-3 eruptions happened at least four times in 1823, 1833, 1846, and 1849. The largest VEI-4 happened in 1872, where the volcanoes ejected its material for about 120 hours, and the volcanic ash was observed as well in Madura and Bawean Island (approximately, 350 km from the Sleman Regency). Intense volcanic activities happened during 1900's, where almost every year to every four-year the VEI-2 eruptions was reported.

The latest eruption in 2000's happened in 2010. The series of eruptions belonged to the centennial eruption of Mt. Merapi and affected all directions around Mt. Merapi. Pyroclastic flow reached 4 km to the North, 11.5 km to the West, 7 km to the East and about 15 km to the South. Explosive bombs reached 4 km from the summit in all directions, with large emissions of ash and gas into the atmosphere. Ash dispersed by the wind affected mostly the western part of the volcano and disturbed the air traffic up to Jakarta. The airport of Yogyakarta was closed for more than 15 days (Surono et al., 2011).

As the rainy season started after the series of eruptions, the large amount of ashes deposit was directly being transformed into mudflows (lahars), flooding valleys close to the Mt. Merapi and destroying many facilities (**Figure 2.6**). Though this eruption and the following lahar events had swept away most of the monitoring instruments, however the Center of Volcanology and Geological Hazard Mitigation (CVGHM) had managed the post-eruptive impacts very well.

The management includes collaboration with the USGS to set-up a system of more than 20 geophones along the valleys that transmits real-time data to the CVGHM. With such a real-time system set-up for the first time at Merapi volcano, the CVGHM will be able to alert security teams as soon as a lahar starts in any valley, by sending messages to the right place at the right time (Jousset et al., 2013). Even though this is a very useful technique, but few efforts in terms of establishing real-time remote monitoring of rainfall at Mt. Merapi are done, in spite of this factor has been understood as the main triggering agent of lahar.

The average annual rainfall observed in 1990 by five stations on Mt. Merapi was about 3270 mm. On Mt. Merapi, the dry season starts from May to October and the rainy season starts from November to April. The total duration of rainfall at Mt. Merapi is 954 hours. Comparing

to Mt. Fuji, greater rainfall intensity at Mt. Merapi happens more frequent (Shuin et al., 1996). The average rainfall intensity in 2015 is given in **Figure 2.7.**

Diurnal and monthly rainfall variation at Mt. Merapi in 1990, that was observed by Shuin et al., (1996) is given in **Figure 2.8**. There was little precipitation in the morning on Mt. Merapi and generally, rainfall happened in the afternoon to night. The highest total accumulation was more than 900 mm at 16:00-18:00. The rainfall at Mt. Merapi had higher intensity and short duration compares to the rainfall at Mt. Fuji. This study has indicated that the type of rainfall at Mt. Merapi is the convectional rain, where the warm air from the heated ground and water accumulates, transforms, and condenses during the daytime resulting in the formation of high intensity and short duration precipitation.
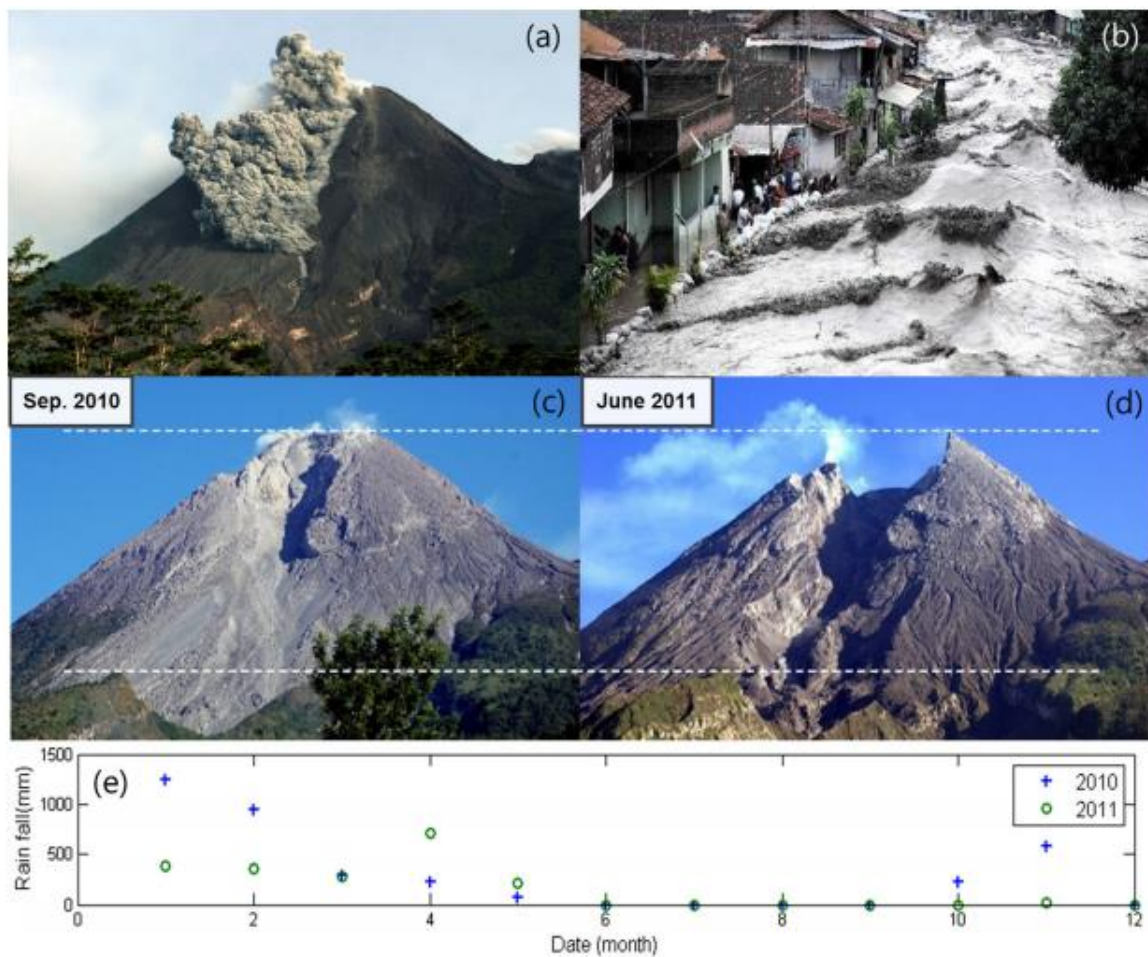


**Figure 2.6** Photographs of Merapi eruptions. (a) Pyroclastic flow that traveled Gendol River. (b) Lahars flow down the Putih River and impact inhabitants living next to the riverbanks. (c) Picture was taken at Gendol before Merapi's eruption in 2010. (d) Picture was taken after Merapi's eruption in 2010 (images from MIA-VITA Project (2009–2012), CVGHM). (e) Rainfall data for Gandol in Sleman for 2010–2011 according to Candra and Sunarto 2014 (Lee et al., 2015).
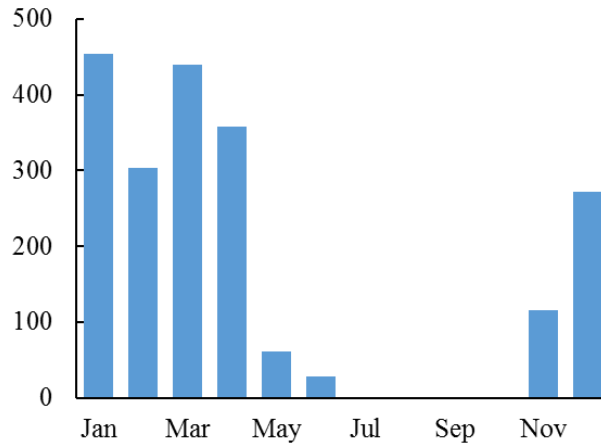
**Figure 2.7** Average rainfall intensity at Mt. Merapi derived by polygon Thiessen method. Data were collected from 9 rain gauge stations at Mt. Merapi (Lashari et al., 2014).
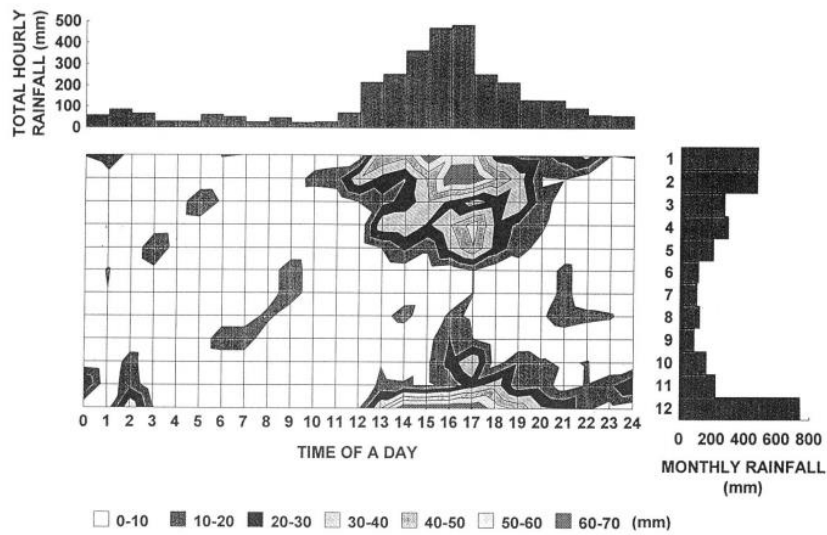


**Figure 2.8** Diurnal and seasonal variation of rainfall at Mt. Merapi (Shuin et al., 1996).

# CHAPTER III

# DEBRIS FLOW MODEL
# BY A SINGLE-PHASE CONTINUUM APPROACH

## 3.1 Introduction

Essential model for flow mechanics should consider constituents as the mixture of continues fluid (water and slurry) and densely assembled discrete particle. It should explain both the macro behaviors such as the mean velocity of the bulk body and flooding limit on an inundation area and the micro individual's particle simultaneously. Currently, the continuum mixture theory that divides the constituents into continuum solid phase and continuum fluid phase and the interaction between them is the most recommended model of debris flow (Takahashi, 2014).

Debris flow and/or lahar simulations have been performed using empirical and numerical models in the past. However, numerical models usually require strong computational expertise and involve a number of variables that make them impractical for field use. Currently some simplified empirical and numerical models that can be operated by users with limited expertise in sediment transport have been developed to fill the knowledge gap between engineers and stakeholders. Some of the well-known lahar simulators are LAHARZ developed by the US Geographical Survey (USGS) and TITAN2D developed by the Geophysical Mass Flow Group at the State University of New York (SUNY).

LAHARZ is one of the most commonly used geographical information system (GIS) based lahar simulation programs. Study of lahar by LAHARZ focused on evaluating the sensitivity toward different quality of digital elevation models (DEMs). Applying LAHARZ to different DEMs has occasionally resulted in unrealistic lateral inundation areas, called ragged edges (Muñoz-Salinas et al, 2009). It was generally assumed that finer resolutions could only produce better results when lahar modeling was done over short distances of 1-2 km (Huggel et al., 2007).

At the Mt. Merapi volcanic area, the application of LAHARZ have resulted in lahar volume predictions of $20 \times 10^6 \, \text{m}^3$ along 10 streams, which was found to be in 55.63% agreement with

real conditions, based on US National Oceanic and Atmospheric Administration (NOAA) LANDSAT Thematic Mapper (TM) satellite imagery (Lee et al., 2015).

However, it neglected the effect of timely rainfall variability in this area, since LAHARZ is a one-dimensional (1D) semi-empirical model based on historical lahar data, which assumed lahar as a flow that moves downstream as an evolving, translating waveform of constant bulk density, mass, and volume (Iverson et al., 1998). While TITAN2D framework originally was designed for application to "dry" granular masses and not wet debris flows (Procter et al., 2010).

In this chapter, the dilatant fluid model combined with Newtonian fluid model adopted by HyperKANAKO model is a suitable model for lahar simulation in Gendol catchment at Mt. Merapi. HyperKANAKO model allows the inclusion of rainfall variability as one of the factors for computing the accumulation of debris flow volumes.

This model is based on Takahashi equation for debris flow (Takahashi, 2014), which follows the dilatant fluid model. In general, it considers the mixture of fluid and grains in the viscous flow maintains the flow movement due to a threshold concentration. Although the constitutive response of this regime is an essentially Newtonian type, however, this kind of model is understood as an equivalent model to the two-phase mixture model in which the dynamic fluid effects are almost negligible (Takahashi, 2014; Hutter et al., 1994).

## 3.2 Single-Phase Models of Debris Flow

In the single-phase continuum models for debris flow, the mixture of particles and fluid is considered as a kind of continuous fluid which behaves as debris flow in various situations. The characteristics of the apparent fluid are determined by the relationship between the operating shear stress and the rate of strain, which is called the constitutive law of the consistency. Three of the most widely used constitutive equations used for single-phase continuum models of debris flows are

1) Newtonian fluid
2) Bingham fluid
3) Dilatant fluid (**Figure 3.1**).

The Newtonian fluid is represented by the laminar flow of plain water in which the shear stress, $\tau$ is linearly proportional to the rate of strain ($du/dz$). Bingham fluid does not deform if the

operating shear stress is smaller than a threshold, but, if the operating stress were larger than the threshold it would behave as a Newtonian fluid. The dilatant fluid decreases the flow mobility with increasing shear rate.
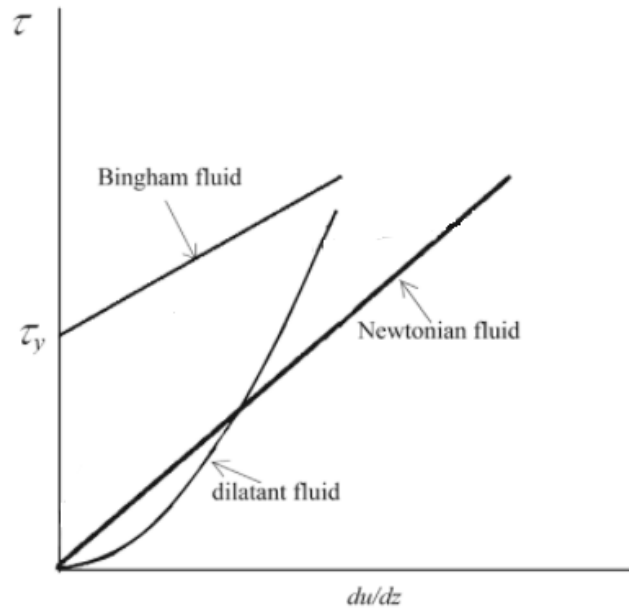


**Figure 3.1** Consistency curves for some kinds of fluid (Image is modified from Takahashi, 2014)

1) Newtonian fluid

Debris flow obviously behaves differently than a plain water flow, which makes it more appropriate to be considered as a non-Newtonian fluid. The Newtonian fluid represents the laminar flow of plain water where shear stress, $\tau$ is linearly proportional to the rate of strain ($du/dz$). However, simplification is required in the numerical models making some previous studies were able to apply this model for debris flow estimation.

An application of the Newtonian fluid model has been applied to simulate a debris flow happened in Jiangjia gully (Takahashi, 1999). This debris flow was evidently laminar but contained a high density of coarse particles. Due to its high viscosity, the turbulence was minimal so that particles could not be suspended by the fluid turbulence. Takahashi (1999) considered that the force acting to disperse particle contained in the flow to keep the mobility was the perpendicular force of particles embedded in the adjacent shearing surfaces. The cross-sectional mean velocity, $U$ was calculated following

$$\frac{U}{u_*} = \frac{1}{3}\frac{\rho u_*}{\mu_a}(1 + \varepsilon\bar{C})h \qquad (3.1)$$

where $u_*$ is friction velocity of shear stress $(=gh\sin^{1/2}\theta)$, $\mu_a$ is the apparent viscosity of the mixture, $\varepsilon = (\sigma - \rho)/\rho$, $\bar{C}$ is the average volumetric solid concentration, $h$ is water depth, and $\rho$ is the density of water.

Takahashi conducted an experiment of two kinds flume in which a steel of movable slope flume 10 m in length, 9 cm in width, and 40 cm in depth was used. The bed was roughened by pasting 3 mm in diameter of gravel to the bed. 13,000 cm$^3$ of the debris flow material was stored in the hoper set at 3.5 m upstream of the outlet of the flume and a high-speed video was set to record the flow at 2 m downstream of the hopper outlet beside the flume. The well-mixed characteristic of the debris flow in the Jingjia gully was simulated by mixing silica sand and kaolin, and a constant solid concentration was set between 0.56 and 0.57. The result showed the agreement of the velocity trend between the experimental and the calculation (**Figure 3.2**).
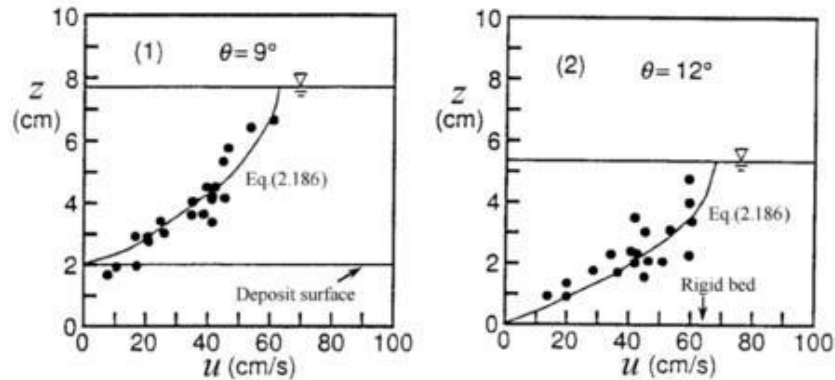


**Figure 3.2** The calculation (curve) and experimental (circles) velocity distribution in the first and second surges by Newtonian rheology

2) Bingham fluid

The Bingham fluid model assumes fluid does not deform if the operating shear stress is smaller than a shear stress threshold, known as $\tau_y$, but when it reaches the threshold, it acts as a Newtonian fluid. This consecutive model has been widely applied to many actual debris flows.

The application of the Bingham fluid model requires yield stress, $\tau_y$ and Bingham viscosity coefficient, $\eta$ obtained by rheometer test of samples, which is collected in the

field. The shearing stress operating on the plane at height, $z$ in a planar flow of depth $h$, and θ in the channel slope is

$$\tau_y + \eta \left(\frac{du}{dz}\right) = \rho g(h - z)\sin\theta \tag{3.2}$$

For Bingham fluid, since it follows $\tau = \tau_y + \eta(du/dz)$, then under the boundary condition, the result is

$$\frac{u}{u_*} = \frac{\rho u_* h}{\eta}\left\{\left(1 - \frac{z\prime}{h}\right)Z - \frac{1}{2}Z^2\right\} \tag{3.3}$$

Bingham fluid model had been applied to study the natural debris flow originating from overconsolidated clay materials in Norwegian Sea. Although it could reasonably explain the small-scale debris flow happened but it could not express the presence of intact-block occurs in the region (de Blasio et al., 2004).

Takahashi (2009) argued that the Bingham fluid application for debris flow is not suitable due to the surge behavior of debris flow. This argument was supported by trying to model the Jiangjia gully debris flow event by Bingham fluid model. the Bingham fluid model gave unreasonable of overestimated flow velocity. Whipple (1997) stated that the Bingham rheology application is limited to mud rich debris flows.

3) Dilatant fluid

Bagnold (1954) who was the first to discover the significance of inter-particle collision as the cause of grain dispersion, majorly contributed the work in the dilatant fluid model. He found that when the rotating velocity was given a small pressure, a shear stress change linearly with the change in shearing rate ($du/dz$). Otherwise, pressure and shear stress varied proportionally to the square of shearing rate ($du/dz$).

Pressure and shear stress in the inertial region is produced by the interparticle collision on the assumption of a particle dispersion system, where the particles embedded in each layer move in equal spacing keeping the velocity of the layer. Finally, the determined formula based on the experimental are

$$p_c = a_i \sigma \lambda^2 d_p{}^2 \left(\frac{du}{dz}\right)^2 \cos\alpha_i \tag{3.4}$$

$$\tau_c = p_c \tan\alpha_i \tag{3.5}$$

Here, $p_c$ is the pressure of flow, $\sigma$ is the density of the mixture, $a_i$ is the experimental coefficients (0.042), $\alpha_i$ is the collision angle to $z$-direction (average values is 17.8°), $d_p$ is the mean diameter of particles, and $\tau_c$ is the bed surface shear stress.

According to Takahashi (2014), based on field data comparison, the dilatant fluid model is an appropriate model for stony debris flows in which the effect of particle collisions dominates. Takahashi applies the Bagnold equation for grain inertia and macro-viscous regimes in a steady open channel flow of grain-water mixture under simple gravity driven shear stress. The grain is heavier than water by assuming that uniform distribution of grains throughout the depth and described the stress balance equation for $x$ and $z$-direction. Because the grain is heavier, they tend to be deposited. Some mechanisms to disperse the grain are required to keep the flow going.

These mechanisms are the rapid shearing and the threshold concentration. The shear stress equals to the square of velocity rate, which is known as the dilatant fluid model, while the concentration is calculated according to

$$C = \frac{\rho \tan\theta}{(\sigma - \rho)(\tan\alpha_i - \tan\theta)} \tag{3.6}$$

where in critical concentration, $C_*$, $\tan\alpha_i = \tan\phi$ and the channel slopes satisfies

$$\tan\theta \geq \frac{(\sigma - \rho)C_*}{(\sigma - \rho)C_* + \rho}\tan\phi \tag{3.7}$$

where $\theta$ is the slope gradien, $\phi$ is the internal friction angle of the sediment, and $\sigma$ is interstitial fluid density.

## 3.3 Lahar Simulation by HyperKANAKO Model

3.3.1 What is HyperKANAKO model?

The HyperKANAKO model was developed by Nakatani et al. in 2012 as an improved version of former KANAKO 1D and 2D models. Both were intended to be simple and effective systems for debris flow simulation based on hydrologic and hydraulic processes. The systems provide information on discharge, water depth, sediment volume, and sedimentation thickness hence permits users to gain an instinctive understanding of the data (Nakatani et al., 2011, 2012).

HyperKANAKO improves data preparation flexibility in terms of the mesh number and mesh size of 2D topographic data by using laser profiler (LP) data or another digital elevation model (DEM). It is able to perform a fast wide-ranging analysis. Results are provided both numerically and spatially, which facilitates further analysis (Nakatani et al., 2012).

HyperKANAKO initially considers debris flow in 1D and then transforms into a 2D flow when it reaches a valley or plain. It uses the same equations as 1D and 2D KANAKO, which are based on the Takahashi model for debris flow (Takahashi, 2014). The continuity equation and the momentum equation for the total debris flow volume are given in equations (3.8)-(3.10):

$$\frac{\partial C_k h}{\partial t} + \frac{\partial C_k uh}{\partial x} + \frac{\partial C_k vh}{\partial y} = i_k C_k \tag{3.8}$$

$$\frac{\partial u}{\partial t} + u\frac{\partial u}{\partial x} + v\frac{\partial u}{\partial y} = g\,\sin\theta_{wx} - \frac{\tau_x}{\rho_m h} \tag{3.9}$$

$$\frac{\partial v}{\partial t} + u\frac{\partial v}{\partial x} + v\frac{\partial v}{\partial y} = g\,\sin\theta_{wy} - \frac{\tau_y}{\rho_m h} \tag{3.10}$$

The change in bed surface elevation is estimated by

$$\frac{\partial z}{\partial t} + i = 0, \tag{3.11}$$

where $h$ is water depth, $u$ is $x$-axis direction flow velocity, $v$ is $y$-axis direction flow velocity, $i$ is erosion/deposition velocity, $i_k$ is the $k$-th sediment erosion/deposition velocity, $g$ is gravitational acceleration, $\rho_m$ is interstitial fluid density, $\theta_{wx}$ and $\theta_{wy}$ are the flow surface gradients in the $x$-axis and $y$-axis directions, and $\tau_x$ and $\tau_y$ are the riverbed shearing stresses in the $x$-axis and $y$-axis directions, respectively.

The erosion and deposition velocity, $i$, are the source terms related to the sediment concentration, which were described by Takahashi et al. (1992) as follows.
Erosion velocity: if $C < C\infty$,

$$i = \delta_e \frac{C_\infty - C}{C_* - C_\infty} \frac{q}{d_m} \tag{3.12}$$

Deposition velocity: if $C \geq C\infty$,

$$i = \delta' \frac{C_\infty - C}{C_*} \frac{M}{d_m}, \tag{3.13}$$

where $\delta$ is the erosion coefficient, $\delta'$ is the deposition coefficient, $d_m$ is the mean diameter of sediment (equals 0.014 m, based on Ikhsan et al., 2010), $C_*$ is the maximum sediment concentration in the flow, and $C_\infty$ is the equilibrium sediment concentration, described by Nakagawa et al. (2003) as follows.

In the case of stony or dynamic debris flow, where $\tan\theta_w > 0.138$, the equilibrium concentration, $C_\infty$, obeys the equation (3.6) to be

$$C_\infty = \frac{\rho_m \tan\theta_w}{(\sigma - \rho_m)(\tan\phi - \tan\theta_w)} \tag{3.14}$$

In the case of immature debris flow, where $0.03 < \tan\theta_w \leq 0.138$,

$$C_\infty = 6.7\left\{\frac{\rho_m \tan\theta_w}{(\sigma - \rho_m)(\tan\phi - tan\theta_w)}\right\}^2 \tag{3.15}$$

If $\tan\theta_w \leq 0.03$, turbulent water flow with bed load transport occurs, so

$$C_\infty = \frac{(1 + 5\tan\theta_w)\tan\theta_w}{\frac{\sigma}{\rho_m} - 1}\left(1 - \alpha_0{}^2\frac{\tau_{*c}}{\tau_*}\right)\left(1 - \alpha_0{}^2\sqrt{\frac{\tau_{*c}}{\tau_*}}\right) \tag{3.16}$$

where

$$\alpha_0{}^2 = \frac{2\{0.45 - \left(\frac{\sigma}{\rho_T}\right)\tan\theta_w/(\frac{\sigma}{\rho_T} - 1)}{1 - \left(\frac{\sigma}{\rho_T}\right)\tan\theta_w/(\frac{\sigma}{\rho_T} - 1)} \tag{3.17}$$

$$\tau_{*c} = 0.04 \times 10^{1.72\tan\theta_w} \tag{3.18}$$

$$\tau_* = \frac{h\tan\theta_w}{(\frac{\sigma}{\rho_T} - 1)d_m} \tag{3.19}$$

where $\phi$ is the internal friction angle of the sediment, $\tau_{*c}$ is the non-dimensional critical shear stress, and $\tau_*$ is the non-dimensional shear stress. If $\tau_* \leq \tau_{*c}$, then $C_\infty = 0$.

The bottom shear stress equations are as follows.

(a) In the case of stony or dynamic debris flow, $C \geq 0.4C_*$, and

$$\tau = \frac{\rho_T}{8}\left(\frac{d_m}{h}\right)^2\frac{u|u|}{\left\{C + \frac{(1-C)\rho}{\sigma}\right\}\left\{(\frac{C_*}{C})^{1/3} - 1\right\}^2} \tag{3.20}$$

(b) In the case of immature debris flow, $0.01 \leq C \leq 0.4C_*$, and

$$\tau = \frac{\rho_T}{0.49}\left(\frac{d_m}{h}\right)^2 u|u| \tag{3.21}$$

(c) In the case of bedload, $C \leq 0.01$, and

$$\tau = \frac{\rho g n^2 u|u|}{h^{1/3}} \tag{3.22}$$

where $n$ is the Manning roughness coefficient.

In this chapter, sabo dam's effect is neglected mainly due to their poor condition as the impact of 2006 and 2010 eruptions and frequent lahars following the eruptions (Wardoyo et al., 2013) so that reducing their effectiveness.

3.3.2 Study area

The target of this study was Gendol-Opak catchment which covers 67 km$^2$ area and 21.73 km length. It lies on the southern flank of the Mt. Merapi volcanic area. The Opak and Gendol Rivers flow parallel and side by side before finally meet in the Rogobangsan tributaries at an elevation of approximately 174 m amsl (**Figure 3.3**). The Gendol River flows along vital infrastructure and historical areas of the Yogyakarta, Surakarta, and Wonosari regions.

The study area has two seasons: the rainy season, that starts in November and a dry season, which starts in the middle of April. Yearly average rainfall ranges from approximately 2200 to 2800 mm. Before the 2010 eruption, the average riverbed slope of the Gendol River was about 0.12° and increased just after the eruption. The change in the riverbed slope led to a change in the sediment transport mechanisms, where high-concentrated flow extends up to 12 km from the summit of Mt. Merapi (Wardoyo et al., 2013).

The centennial eruption of Mt. Merapi in 2010 deposited 10 times the volume of the pyroclastic materials resulting from the 1994 and 2006 eruptions, and most of these materials were deposited in Gendol River. According to the National Board for Disaster Mitigation, the volume was caused by the direction of 9 of 10 multi-phase pyroclastic flows leading into the Gendol catchment area (Wardoyo et al., 2013).
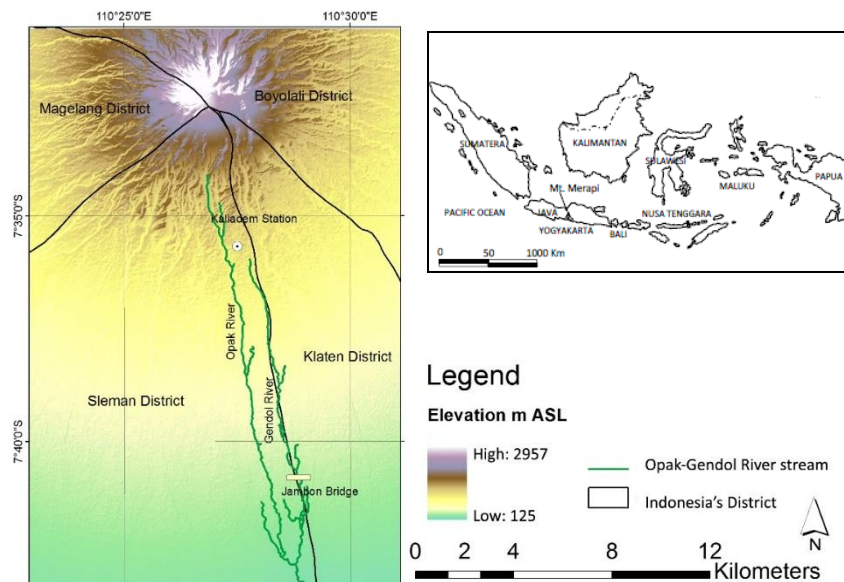


**Figure 3.3** Opak-Gendol River stream (ALOS DSM 5 m resolution). Insert, the location of Mt. Merapi volcanic area in Indonesia (Legono et al., 2015).

These flows covered an area of ~27 km$^2$ in the Gendol-Opak catchment, which amounts to approximately 34 million-m$^3$ deposit volcanic material. The eruption also destroyed numerous facilities such as sabo dams and observatories sites. During the 2010 to 2013 period, frequent lahar events imposed significant devastation on the area, including loss of human life (Lee et al., 2015).

3.3.3 Data and methodology

Data used in this study consist of spatial data of the Gendol River from three different Digital Elevation Models (DEMs) resolution levels, which are the US National Aeronautics and Space Administration (NASA) Shuttle Radar Topographical Mission (STRM) 90 m DEM (M$_1$), the US Jet Propulsion Laboratory (JPL) Advanced Spaceborne Thermal Emission and Reflection Radiometer (ASTER) 30 m DEM (M$_2$), and the Japan Aerospace eXploration Agency (JAXA) Advanced Land Observation Satellite (ALOS) 5 m DEM (M$_3$). Rainfall data used were recorded on 1 February 2013 (R$_1$) and 15 February 2013 (R$_2$) from the Kaliadem station, which is supported by the Hydraulic Laboratory of Gadjah Mada University. Based on the DEM analysis, there is a significant difference in the slope angle at elevations higher than 1200 m amsl, where the average angle is 20$^o$ and below 1200 m amsl, where the average is 3.43$^o$. Considering this condition and previous study that stated lahar flow occurrences at Mt. Merapi volcanic area rivers usually reach 400-650 m amsl (Lavigne et al., 2007), a 1D flow is modeled at an elevation of 2300-1200 m amsl and 2D lahar flow is projected to occur at the height of 1200 until 580 m amsl.

This study was divided into two steps: data preparation and running HyperKANAKO model.

1) Data Preparation

Rainfall data were first analyzed to set up the upstream supplied hydrograph using the Nakayasu synthetic hydrograph method (Equation (3.23)), while timely sediment concentration changes were interpolated based on discharge data according to HyperKANAKO simulation handbook.

$$Q_p = \frac{cAR}{3.6(0.3T_p + T_{0.3})} \qquad (3.23)$$

Here, $Q_p$ is peak discharge (m$^3$/s), $R$ is unit rainfall intensity (mm/h), $T_p$ is time required from start raining until the flood peak (hour) (h) defined in equation (3.24), and $T_{0,3}$ is time

required to discharge reduction up to 30%, $A$ is watershed area (km$^2$), and $c$ is river coefficient (0.75).

$$T_p = t_g + 0.8t_r \tag{3.24}$$

Where $t_g$ is the function of the time-concentration and duration of effective rainfall ($t_r$). Rising limb curve ($Q_d$) is the function of peak discharge $Q_p$, time ($t$), $T_p$, and $T_{0.3}$. The equation is,

$$\text{if } Q_d > 0.3Q_p, \text{ then } Q_d = Q_p 0.3^{\frac{t-T_p}{T_{0.3}}} \tag{3.25}$$

$$\text{if } 0.3Q_p > Q_d > 0.3^2 Q_p, \text{ then } Q_d = Q_p 0.3^{\frac{t-T_p+0.5T_{0.3}}{1.5T_{0.3}}} \tag{3.26}$$

$$\text{if } Q_d > 0.3^2 Q_p, \text{ then } Q_d = Q_p 0.3^{\frac{t-T_p+1.5T_{0.3}}{2T_{0.3}}} \tag{3.27}$$

The short-term upstream supplied hydrographs of Gendol River based on Nakayasu method are given in **Figure 3.4**.
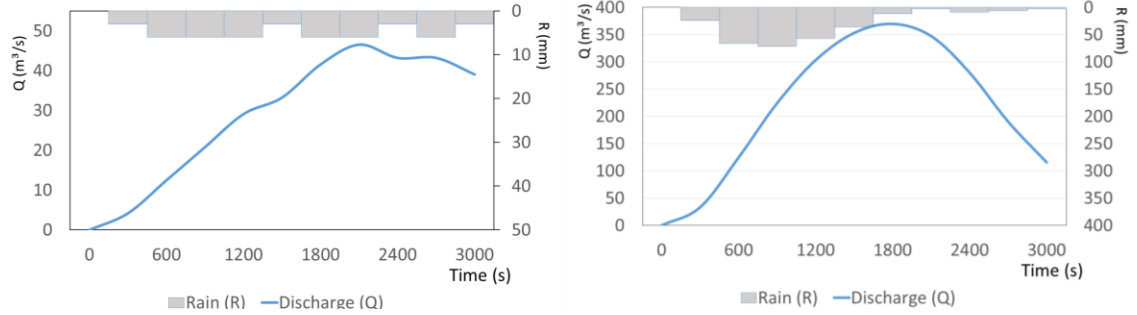


**Figure 3.4**  Hydrographs of rainfall; left is on 1 February 2013 (R$_1$) on the left and on 15 February 2013 (R$_2$)

All spatial data were converted to 5 m grid resolution using the nearest neighbor method. Mesh data were created based on $Z$ (height) value at each grid ($x,y$) using the mesh creation tools included in the HyperKANAKO package.

(2) Lahar Simulation by HyperKANAKO

Lahar simulation begins with the selection of 1D flow at a certain height amsl. The model will then automatically determine the direction of flow. The 2D plane was adjusted to have an area of $2 \times 7$ km$^2$. The final step is to adjust the hydrograph and a number of parameters required by model presented in **Table 3.1**. Lahar simulations were performed on each of every spatial data (M$_1$-M$_3$) by applying both rainfall data (R1 and R2). Models were run for 3000 s based on previous research that found the peak discharge of rain-

triggered debris flow in Gendol River happens at t = 1800 s and mostly decrease after 2400 s (de Belizal et al., 2013).

**Table 3.1** Simulation initial parameters

| Parameters | Value | Unit |
|---|---|---|
| Simulation time | 3000 | s |
| 2D mesh size interval | 10 | m |
| 2D mesh number (XY) | 200x700 | m |
| Minimum depth of 2D calculation | 0.01 | m |
| 1D Slope angle | 20 | ° |
| 1D river width | 20 | m |
| Movable bed layer | 3 | m |
| Number if 1D mesh observation points | 665 | |
| 1D Roughness value | 0.03 | |
| 1D mesh size interval | 5 | m |

3.3.4. Result and discussion.

(1) 1D Simulation results.

The simulation results for peak discharge of 1D flow are presented in **Table 3.2**. Since coarser resolution DEMs do not provide fine topography variability, lower frictional force was expected to show increased flow velocity. However, as can be seen in **Table 3.2**, the highest resolution ($M_3$) shows the highest discharge level, which indicates the limitation of 1D model to analyze lateral flow.

**Table 3.2** Peak discharge (Qp) and peak time (Tp) of 1D lahar in the Gendol River.

| Variables | $Q_P$[m³/s] | $T_P$[s] |
|---|---|---|
| $R_1M_1$ | 90 | 2300 |
| $R_1M_2$ | 120 | 2300 |
| $R_1M_3$ | 130 | 2300 |
| $R_2M_1$ | 1400 | 2400 |
| $R_2M_2$ | 1500 | 2400 |
| $R_2M_3$ | 2000 | 2400 |

Two-way analysis of variance (2-factor ANOVA) without replication, determined that even if finer DEM increased the discharge, the amounts were not statistically significant. For $R_1$, only a slight difference was noted between $M_2$ and $M_3$, while a larger difference was noted for $R_2$. The same results also applied for peak time, where higher rainfall accumulation results in peak time delays.

Therefore, we can conclude that 1D flows depend on rainfall data alone, and are not sensitive to DEM resolution levels. Despite of 1D model limitation, they could show the effect of slope difference along the 1D trajectory, which indicates gravitation is important to generate lahar flow. This finding is in agreement with the fact that, in principal, debris flow is gravity driven (Iverson, 1997).

(2) 2D Simulation Results.

The 2D analysis shows different flow spatial distribution amongst DEMs data, as shown in **Figure 3.5** were the coarser the resolution, the more accumulated flow is concentrated in areas higher than 1000 m amsl. While at the finest resolution ($M_3$), water depth at some area lower than 700 m amsl still distributed well with values higher than 5 m. This result shows that coarser resolution simulation gave lahar flow to inundate upstream area without flowing to downstream area (**Appendix 3**).

These findings are consistent with the behavior of lahar flow range that remains dangerous at elevations of 450-600 m amsl (Lavigne et al., 2000; Wardoyo et al., 2013) and are in agreement with the lahar disaster risk map of Mt. Merapi volcanic area. Similar results by Widowati (2016) using three kind of Light Detection and Ranging (LiDAR) DEMs of 5 m, 10 m and 20 m resolutions applied to SIMLAR found that lower resolution produces wider sediment extent out of the actual lahar flow path in Putih River of Mt. Merapi, which did not exist during the field event. SIMLAR is a 2D mathematical model based on hydrologic and hydraulic process developed by the Ministry of Public Works of Indonesia and Gadjah Mada University.

The simulation result obtained using $M_3$ clearly shows HyperKANAKO's ability to simulate the actual lahar conditions that occurred on the Gendol River as reported on 15 February 2013, where lahar flow destroyed Jambon Bridge (Sleman Regency, **Figure 3.3**), which is located in an area lower than 300 m amsl.
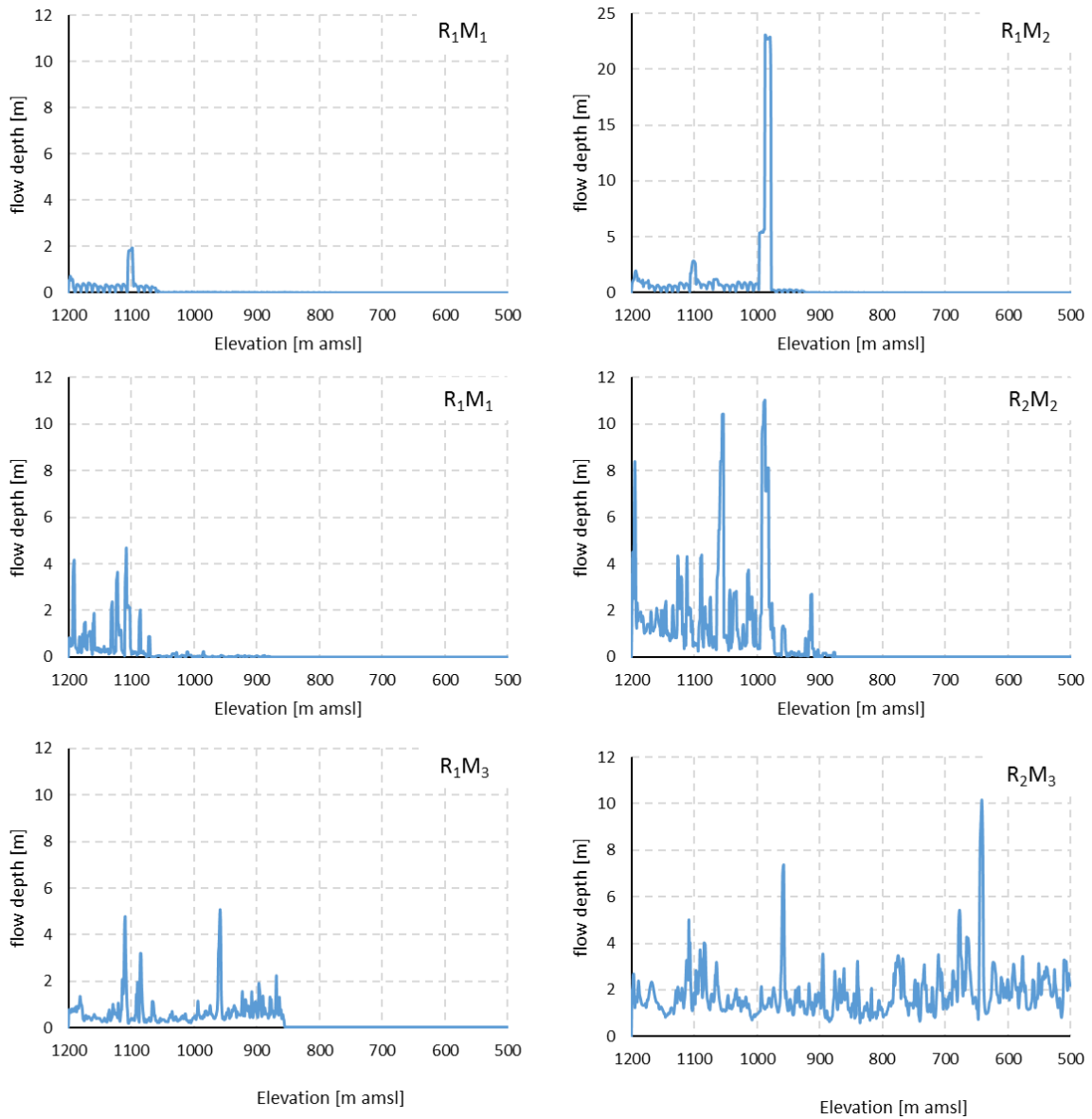
**Figure 3.5** The 2D HyperKANAKO simulation results for water depth (m) in the Gendol River
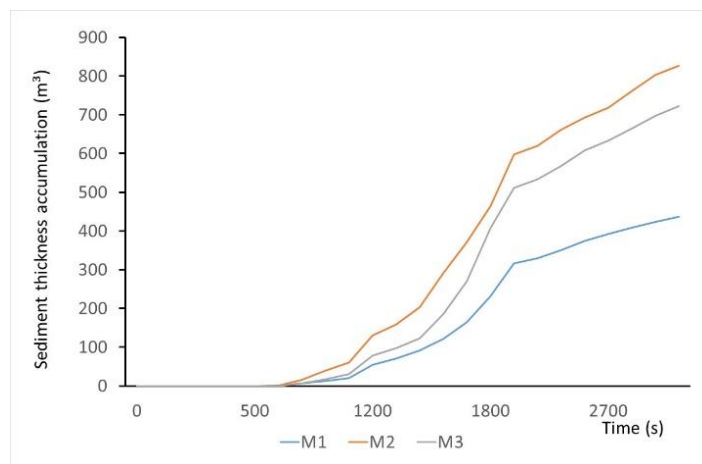


**Figure 3.6** Sediment thickness accumulation of $R_2$ in 2D plane

Considering the discharge values from 1D flow as the source of the 2D flow, therefore, higher areas have wider inundated area because the travel distance is shorter and accumulates only at this particular elevation. It also shows that coarser resolutions were unable to identify lateral flow areas, and had difficulty identifying channel stream. Paul et al. (2017) mentions that the resolution of DEM plays important role in identifying river stream network. The finest resolution provided by $M_3$ at the end of the timed simulations for both rainfall datasets used gave the furthest flowing mass length with water depth mostly higher than 0.5 m and even higher than 5 m ($R_2$) even in the lower elevation.

(3) Coarse Sediment Accumulation

HyperKANAKO model parameterized solid mixed-size grain particle, which varies from 0.1-1 m (Nakatani et al., 2011). The timely sediment accumulation values that resulted from lahar during the $R_2$ simulation are presented in **Figure 3.6**.

The coarsest resolution of $M_1$ gives lowest sediment accumulation when compared to $M_2$ and $M_1$. Different spatial distribution could be obtained within the limits of the coarser DEM. However, in general, sediment accumulation should show the same values since the simulation covered the same area (Schneider et al., 2008).

The highest sediment accumulation presented by $M_2$ strengthened the tendency of the ASTER DEM to overestimate lahar simulation, which has been observed in previous studies (Huggel et al., 2007). It is assumed caused by ASTER based models show stronger lateral flow distribution and easily deviated from its true drainage pathways. This is likely due to interpolated areas of missing data errors in the drainage channel in ASTER image processing.

SRTM which previously has been considered to be more reliable than ASTER (Huggel et al., 2007) gave lower results, because the DEM was taken in 2000, thus it is unable to represent the topography deformation caused by 2006 and 2010 eruption which have changed bed slope and increase lahar flow distance (Wardoyo et al., 2013). Therefore, timely topography analysis in an active volcanic area is important for getting better results.

However, the ability of HyperKANAKO simulation to recognize channel stream and extent lahar flow distance when it is applied to the finest resolution has led to the importance of using high-resolution spatial data in lahar simulation. This is certainly

contradicting previous assumption that finer resolutions could only provide improved results for shorter length flow (Huggel et al., 2007).

In relation to supporting this sensitivity results, field observation is highly recommended for validation. The importance of rainfall in initializing lahar mobilization at Mt. Merapi volcanic area should also be explored further since HyperKANAKO has an empirical approach for upstream hydrograph. Applying the kinematic wave approximation from a distributed rainfall-discharge model or a semi-distributed model might be the recommendation in the future work.

## 3.4 Summary

Three of the widely used constitutive equations used for single-phase continuum models of debris flows are Newtonian fluid, Bingham fluid, and dilatant fluid. Dilatant fluid model is the best approach for debris flow simulation, and considered equals with two-phase model. However, Newtonian fluid model could also be used for viscous turbulent debris flow calculation.

The application of dilatant fluid model for lahar flows simulation in the Gendol River of the Mt. Merapi in Indonesia provided the best performance level when the finest resolution of ALOS data were used, since finer DEM resolution made it possible to project finer topography variations that influence the lateral flow and able to identify stream channel. ASTER and SRTM were not feasible for lahar simulation due to the gross error and outdated information. On the other hand, it was confirmed that rainfall variability tends to play more important role in 1D flows.

# CHAPTER IV

# INTEGRATING X-MP RADAR DATA FOR
# LAHAR SIMULATION

## 4.1 Introduction

After the 2010 eruption, more than 50 volcanic debris flow (lahar) events occurred during the rainy season of 2010–2011 at Mt. Merapi, Indonesia (de Belizal et al., 2013). The lahars occurred following severe rainfall intensity in the upstream area, where remaining volcanic material was deposited. Estimation of rainfall-induced lahars at Mt. Merapi is difficult and uncertain because the upstream area is dangerous and inaccessible.

On 17 February 2016, a lahar occurred in the upstream region of the Gendol River on the southeastern flank of Mt. Merapi after a maximum rainfall intensity of 69 mm/h was monitored on the peak of Mt. Merapi by X-band multi-parameter (X-MP) radar. However, those rainfall was not monitored by the only rain gauge located near the upstream area. This problem raised concern on the importance of remote monitoring of rainfall in volcanic area and also the uncertainty given by rain gauge measurement.

In this chapter, rainfall intensity estimates from X-MP radar were applied to generate boundary discharge of HyperKANAKO. The numerical simulation was able to estimate volcanic debris flow occurrence and magnitude at the catchment scale. The reliability of radar-rainfall data and the effects of the sabo dam on reducing the impacts of lahar disaster were also examined. This chapter demonstrated the effectiveness of remote monitoring of rainfall combined with numerical debris flow modelling for applied practical use in disaster management.

## 4.2 Lahar Monitoring System at Mt. Merapi

The early measurement of rainfall at Mt. Merapi was pioneering by Dutch and German scientists since 1934, and by the Volcanological Survey of Indonesia, which collected subsequent rain gauge data during 1960s. Because lahar events are one of the major disasters in the Mt. Merapi volcanic area, the government of Indonesia has developed an early warning

system (EWS) for lahar disaster preparedness prior to 1970 (Hardjosuwarno et al., 2013; Lavigne et al., 2000a).

The system consisted of wire sensors that crossed the perimeter of the river at the height of 1 m from the riverbed that could calculate the velocity of any lahar. Radio communication was used to send pertinent information to residents. During the continuation of the system, it was equipped with a movie camera for recording lahar events. A lahar warning was issued if the flow was large enough to break the wire(s). However, some large lahar events did not break the wire because of their diluted concentration (Lavigne et al., 2000a).

Rainfall monitoring was improved by the installation of some new rain gauges station since 1973. Three rain gauges were installed in Deles, Yogyakarta and Babadan. Those rain gauges installation was continued until 1984 and in total 32 rain gauges were installed to monitor rainfall condition at Mt. Merapi (Lavigne et al., 2000a).

In the same time, the Volcanic Sabo Technical Center (VSTC) in corporation with The Japan International Cooperation Agency (JICA) installs a radar rain gauge that provides visual information on the occurrence, movement and disappearance of "hyeatal regions". This system is able to monitor an area of 60 x 80 km with three observational modes (maximum, normal and enlarged image).

The best data are obtained by the enlarged mode, which defines the minimum observation area (20 km W–E x 15 km N–S). This range is divided into a 4000 mesh grid (250 m W–E x 300 m N–S): The intensity and areal distribution of rainfall can be viewed on a display screen, with the data stored on a floppy disc for future analysis. However, the radar could not consistently provide continuous rainfall data compared to the performance of the rain gauge (Shuin et al., 1996) and was reported to have functioned for only one week because of a data storage problem (Lavigne et al., 2000a).

In 2010, the centennial eruption of Mt. Merapi destroyed most of the lahar monitoring instruments. During the recovery, the government and Gadjah Mada University, later installed new rain gauge system to replace the prior rain gauges. The location of each rain gauges and an example of rain gauge installed in Gendol River is shown in **Figure 4.1**.
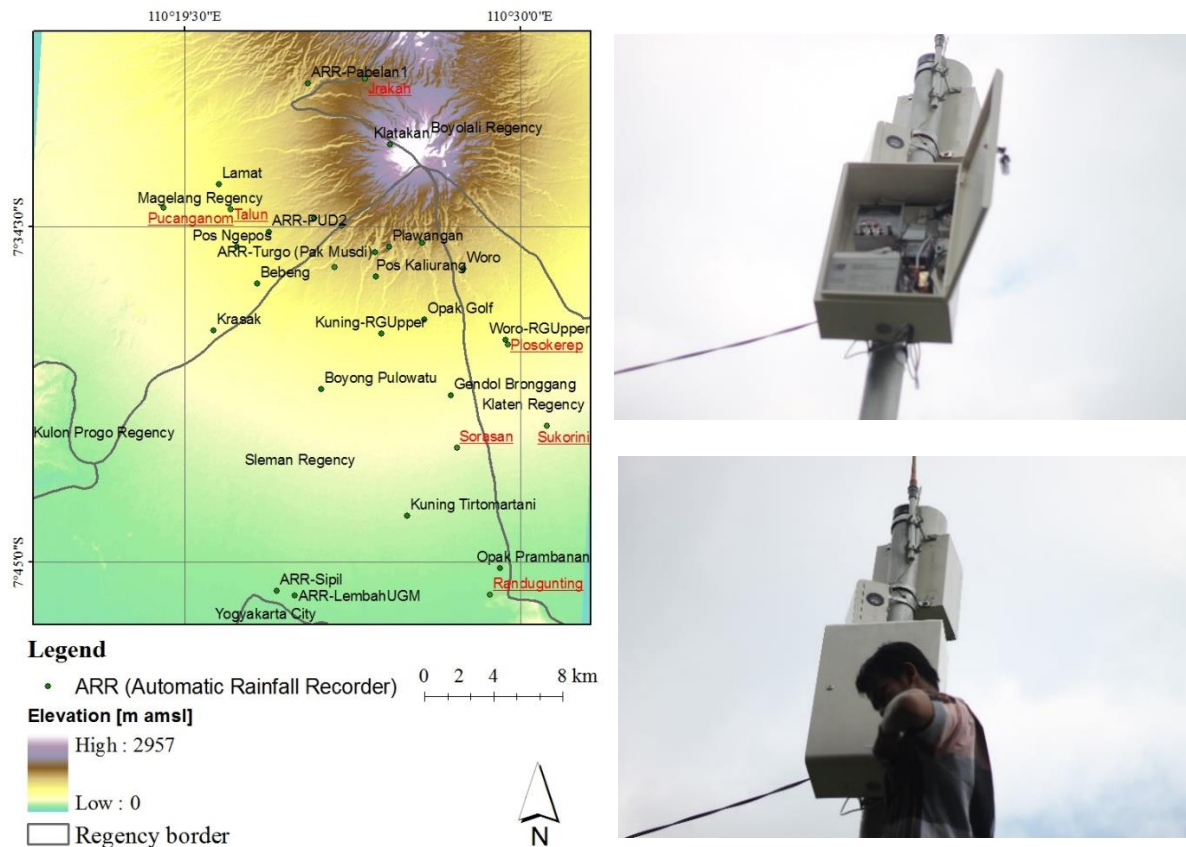
**Figure 4.1** Automatic Rainfall Recorder (rain gauge) distribution at Mt. Merapi (left), a rain gauge installed by Gadjah Mada University (right-top), a technician is collecting the rainfall data from data logger (right-bottom).

To analyze the reliability of rainfall measured by rain gauge, rainfall values in January to June 2016 from 7 rain gauge stations at Mt. Merapi were compared linearly by the least square method (**Figure 4.2**). Each rain gauge shows great variance with one and another. This means, while there was a rainfall recorded at a station, no rainfall happened in nearby stations. Another problem is the discontinuity observation by rain gauge data, which causes some severe rainfall events are not observed by the rain gauge.

In Gendol catchment, rainfall and lahar flow can be monitored by 10 ARRs and 2 Automatic water level recorders (AWLRs) (**Figure 4.3**). However, some of the rain gauges do not give continues data and sometimes unable to monitor heavy rainfall intensity due to some technical problems. An example of rainfall data availability until February 2016 is presented in **Table 4.1**. These problems encourage the need for a better rainfall observation tool such as by weather radar. Although the Quantitative precipitation estimation (QPE) from weather radar still have some uncertainties (Over et al., 2007; Habib et al., 2004), but this kind of study is important for a safe and precise remote based of real-time lahar monitoring in the future.

41
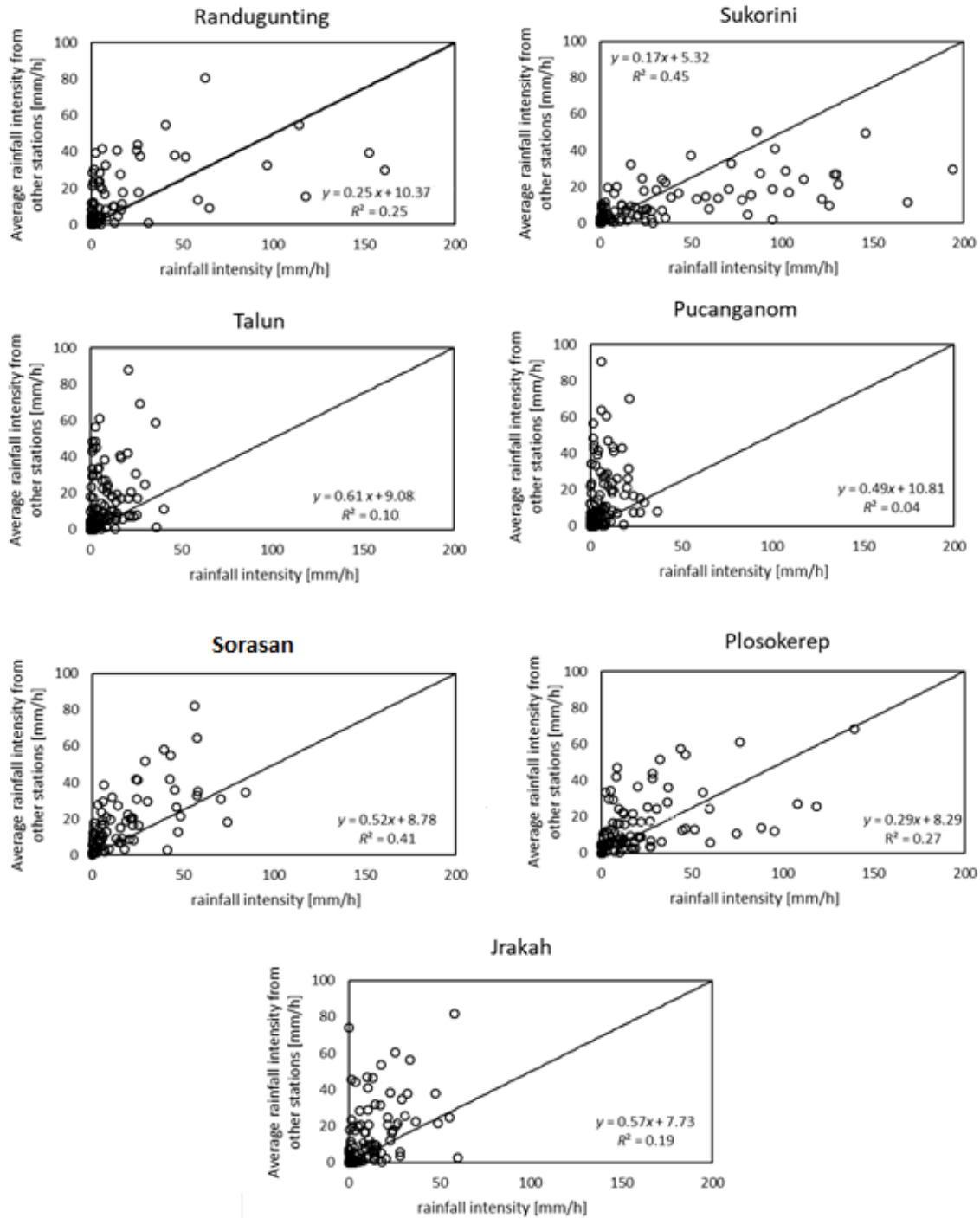
**Figure 4.2** Comparison of rainfall intensity between seven rain gauges station and average rainfall intensity from other nearby stations based on data from January-June 2016.
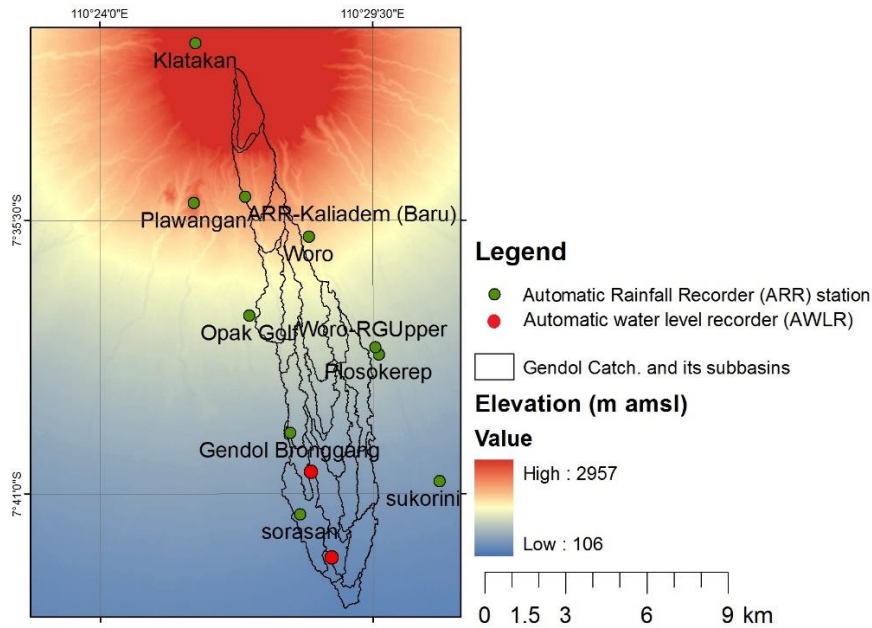
**Figure 4.3** Gendol catchment and distribution of ARRs and AWLR in and nearby the catchment

**Table 4.1** Data availability of ARRs in Gendol catchment for September 2015 to February 2016

| No | Station | Rainfall parameter | Time resolution (min) | Data availability* | | | | | |
|---|---|---|---|---|---|---|---|---|---|
| | | | | 09-15 | 10-15 | 11-15 | 12-15 | 01-16 | 02-16 |
| 1 | Gendol Bronggang | Intensity | 5 | 30/30 | 31/31 | 19/30 | 31/31 | 30/31 | Prepare |
| 2 | Woro | Intensity | 5 | 30/30 | 31/31 | 19/30 | 31/31 | 30/31 | Prepare |
| 3 | Opak Golf | Intensity | 5 | 30/30 | 31/31 | 19/30 | 31/31 | 30/31 | Prepare |
| 4 | Klatakan | Intensity | 5 | 30/30 | 31/31 | 19/30 | 31/31 | 30/31 | Prepare |
| 5 | Plawangan | Intensity | 5 | 30/30 | 31/31 | 19/30 | 31/31 | 30/31 | Prepare |
| 6 | Plosokerep | Amount | 60 | 30/30 | 31/31 | 30/30 | 31/31 | 31/31 | 29/29 |
| 7 | Sorasan | Amount | 60 | 30/30 | 31/31 | 30/30 | 31/32 | 31/31 | 29/29 |
| 8 | Sukorini | Amount | 60 | 30/30 | 31/31 | 30/30 | 31/31 | 31/31 | 29/29 |
| 9 | ARR-Kaliadem (Baru) | Intensity | 5 | 8/30 | 23/30 | 24/30 | 31/31 | 31/31 | 21/29 |
| 10 | Woro-RGUpper | Intensity | 5 | 8/30 | 23/31 | 25/30 | 31/31 | 18/31 | 0/29 |

Annotation: *The data availability shows the number of recorded rainfall days within a month; Prepare: no response as of yet to data request

**4.3 X-MP Radar for Rainfall Monitoring at Mt. Merapi**

4.3.1   Radar Hydrology

The significance of rainfall spatial structure in flood runoff studies has been confirmed by many studies (Chiang and Chang, 2009; Kim et al., 2006). Weather radar is a desirable instrument for observing rainfall over large spatial domains within fine time resolutions. It is now becoming one of the most desirable data to hydrologists with an application to distribute hydrologic modeling.

Compared with the sparse distribution of rain gauges, the high spatial and temporal resolutions of radar-observed rainfall fields are highly desirable for debris flows and landslide studies (David-Novak et al., 2004; Chiang and Chang, 2009). Radar-based estimation of debris-flow triggering rainfall may pose different challenges with respect to those characterizing more hydrological applications. These differences are largely related to the small size of debris flow catchments (sometimes even less than 1 km$^2$) (D'Agostino and Marchi, 2001).

Considering that debris flows scales are comparable to a single radar pixel, it is expected that radar beam pointing errors may have an important effect on estimating the actual triggering rainfall properties. This is important as debris flow triggering events are often characterized by high precipitation gradients (i.e. rainfall spatial variability) (Nikolopoulos et al., 2014). Recent studies have confirmed the importance of the rainfall spatial structure in flood runoff generation and also debris flow occurrence (Marra et al., 2014; Segond et al., 2007; Berne et al., 2004).

X-band radar observation, whereby 0.5 km resolution can be achieved, provides more detail rainfall information than conventional radars (**Table 4.2**) (Kato and Maki, 2009). Thus, it has a considerable potential for the applications in debris flow and lahar studies.

The radar-rainfall algorithm provides QPE by weather radar. Theory of drop size distribution (DSD) initially proposed by Marshall and Palmer (1948) introduced the algorithm for QPE from radar horizontal reflectivity, $Z_h$. In contrast to conventional radars, which measure horizontal reflectivity, polarimetric radar measures from both horizontal and vertical polarizations. Some advance studies revealed that more accurate rainfall amounts could be obtained from a polarimetric radar (Schafenberg et al., 2005; Maki et al., 2005).

**Table 4.2** Weather radars band

| Type | Wave length and frequency | characteristic |
|------|---------------------------|----------------|
| S-Band | 8-15 cm, 2-4 GHz | Not easily attenuated, long range observation |
| C-band | 4-8 cm, 4-8 GHz | Easily attenuated, short-range weather observation |
| X-band | 2.5-4 cm, 8-12 GHz | Highly attenuated, possible to detect smaller particle, very short-range observation |

The fundamental polarimetric parameters for estimating the rainfall intensity are radar reflectivity factor ($Z_{DR}$) and differential phase shift ($K_{DP}$). Differential phase shift ($K_{DP}$ [°km$^{-1}$]), which is defined as the difference between the horizontal and vertical pulses of the radar as they propagate through a medium such as rain or hail, is one of the features of X-MP radar. The radar reflectivity factor ($Z_h$ [dBz]) indicates the strength of backward scattering of radio waves to the radar after the signal strikes raindrops.

A composite method proposed by Park et al. (2005) derived from the observation of X-band polarimetric radar in Tsukuba, Japan, which represents the mid-latitude regime, is usually adapted for estimating the rainfall intensity values. The radar-rainfall algorithms using the composite algorithms are expressed as follows.

$$R(Z_H) = 7.07 \times 10^{-3} ZH_H^{0.819} \text{ for } Z_H \leq 30 \ dBZ \text{ or } K_{DP} \leq 0.3^o \text{km}^{-1} \tag{4.1}$$

$$R(K_{DP}) = 19.63 K_{DP}^{0.823} \qquad \text{otherwise} \tag{4.2}$$

$$R(Z_H) = 7.07 \times 10^{-3} ZH_H^{0.819} \text{ for } Z_H \leq 30 \ dBZ \tag{4.3}$$

$$R(Z_H) = 7.40 \times 10^{-2} ZH_H^{0.566} \text{ for } Z_H \leq 30 \ dBZ \tag{4.4}$$

Detail information about the QPE is already explain in Hapsari (2011) and not the main focus of this study, as the X-MP radar at Mt. Merapi gives rainfall intensity as one of the products. However, comparison with ground measurement is still needed to show the reliability of radar data, which is explain in sub-chapter 4.3.3

### 4.3.3 X-MP radar description

The Sabo Works Agency (Balai Sabo) installed the new generation of X-MP radar to replace the RRG. The radar measures Doppler velocity and transmits an electromagnetic signal at a

frequency of 9.345 GHz. It covers a radius range of 90 km, and its X-band radar specifications are a 3 cm wavelength and short-range distance (Hardjosuwarno et al., 2013). However, its utilization for lahar monitoring is very limited due to some uncertainty of the QPE algorithms (Mulyana et al., 2016)

In 2015, the Science and Technology Research Partnership Sustainable Development Program (SATREPS) project installed an X-MP radar that operates at 3.3 cm of wavelength. This radar is installed closer to the summit of Mt. Merapi (8.7 km) (**Figure 4.4**). The spatial resolution is 150 m mesh and the temporal resolution is 2-minute. It is designed to monitor not only the rainfall condition but also some of the volcanic material ejected from the volcano during an eruption. **Table 4.3** provides the specifications of this radar.

### 4.3.4   Reliability of X-MP radar

The 2-minute rainfall intensity, $R$, from X-MP radar was converted to hourly amount values [mm] before the values were compared to the rainfall amounts from 7 rain gauges (**Figure 4.3**) provided by the Sabo Works Agency. It was important to establish the X-MP radar performance within the entire radius range. Only stations managed by the Sabo Works Agency were taken into consideration as they provide more current and continuous data.



**Figure 4.4** X-MP radar installed at Mt. Merapi Meseum

**Table 4.3** X-MP radar installed in the MVA by the SATREPS project

| Parameter | Description |
|---|---|
| Transmitter | Solid state 200 W per channel (H,V) |
| Polarity | Dual polarimetric horizontal (H) and vertical (V) |
| Pulses | PRF 600–2,500 Hz, Width 0.1–5.0 µs |
| Antenna | 1,086 mm $\Phi$, 2.7° beam width |
| Antenna gain | 33.0 dBi |
| Operating frequency | 9.47 GHz |
| Wavelength | 3.3 cm |
| Scan mode | PPI, CAPPI, RHI |
| Resolution of distance | Maximum of 50 km |
| Maximum range fixed observation level | 30 km |
| Data output | Reflectivity intensity $- Z_h$ [dBz], <br><br> Differential reflectivity $- Z_{dr}$ [dB], <br><br> Doppler velocity $- V_D$ [m/s], <br><br> Doppler velocity spectrum width $- \sigma_{VD}$ [m/s], <br><br> Specific differential phase shift $- K_{DP}$ [°km$^{-1}$] <br><br> Correlation coefficient between two polarizations $- \rho_{HV}$, <br><br> Rainfall intensity $- R$ [mm/h], <br><br> Cross polarization difference phase $- \Phi_{DP}$ |

*Source*: Furuno, Compact X-band dual polarimetric doppler, WR-2100 information brochure

In this study, the $Z_h$ and $K_{DP}$ data were obtained from constant altitude plan position indicator (CAPPI) scanning at 1.2 km amsl. An example of rainfall monitoring by X-MP radar is given in **Figure 4.5**.

Previously, Over et al. (2007) recommended hourly comparison to determine the reliability of Doppler weather radar. They stated its importance for hydrological models and determination of radar's accuracy. The comparison was done for May and September 2016 because continuous X-MP radar data were unavailable for the period of June to August 2016 due to an electricity problem. Data were compared by using the least mean square analysis. A comparison of the rainfall amount estimates from X-MP radar and ARR is provided in **Figure 4.6.** The radar rainfall amount has a tendency to yield smaller values than ARR, which is similar to previous findings by Over et al. (2007).
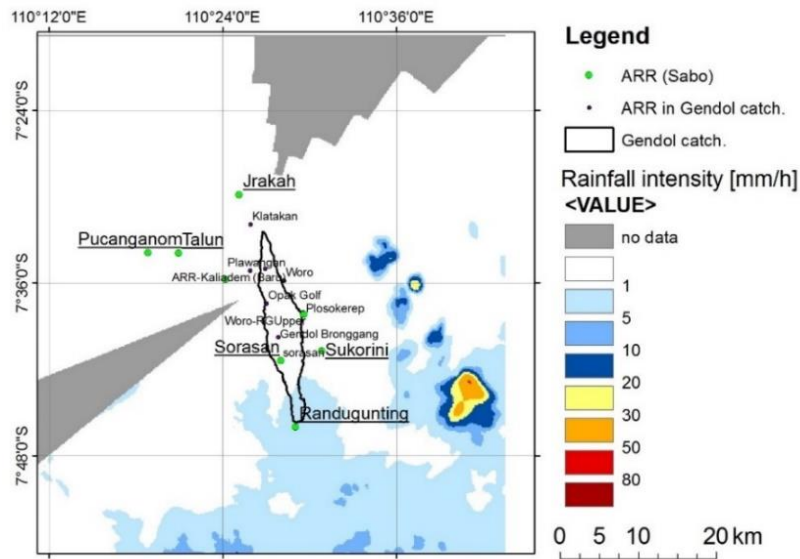
**Figure 4.5** Rainfall intensity, $R$ [mm/h], monitored by X-MP radar at 19:40, 30 May 2016, and rain gauge network under Sabo Work Agency management (green dots) and in Gendol catchment (dark dots).

Either one or a combination of the following three main reasons probably causes the underestimated values of rainfall amount from the radar. First, the algorithm for rainfall intensity, $R$, is derived from $Z_h$ and $K_{DP}$ from subtropical regions (Hapsari, 2011), where the rainfall characteristics are different from those of tropical rainfall. Second, attenuation of radar still occurs. The attenuation of radar is a common problem that is attributable to the radar's wavelength. Shorter wavelength radar (X-band) is attenuated to a greater extent than longer wavelength radar (C-band). This problem causes a rainfall echo behind stronger rainfall, which results in the reflection of a weaker electromagnetic wave resulting in bias of the rainfall measurement. Thus, rainfall intensity could be underestimated.
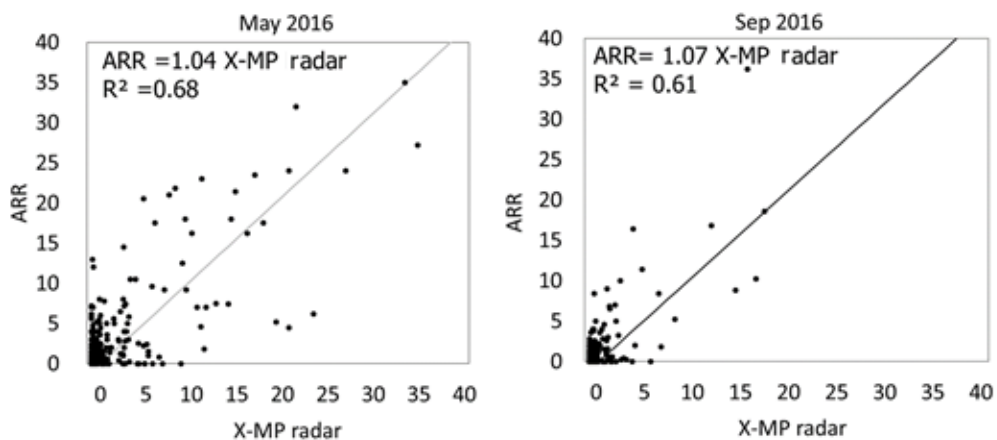


**Figure 4.6** Scatter plot of rainfall amount [mm] by X-MP radar vs. ARR at eight different ARR stations managed by the Sabo Public Works Agency (**Figure 4.3**).
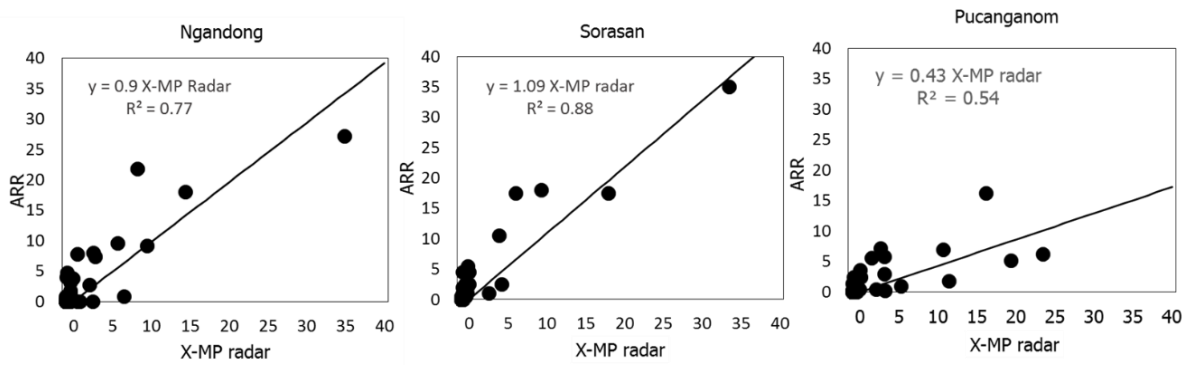
**Figure 4.7** Rainfall amount [mm] estimates of X-MP radar versus ARR measurement for May 2016 at three stations: Ngandong station (3.4 km from the X-MP radar), Sorasan station (9.5 km from the X-MP radar), and Pucanganom station (13.5 km from the X-MP radar).
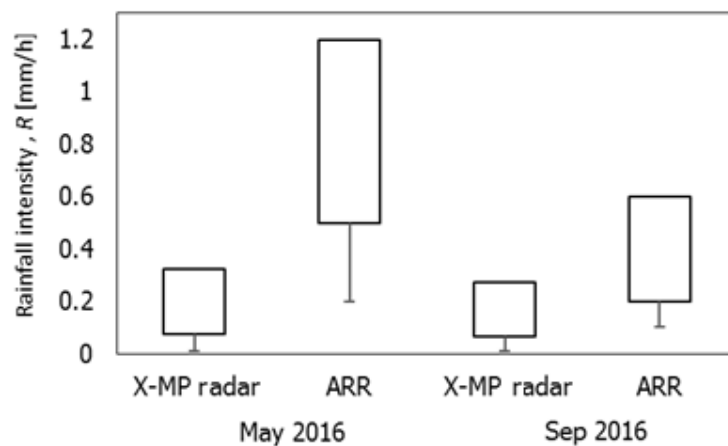


**Figure 4.8** Minimum rainfall amount [mm] distributions up to the median values of X-MP radar and ARR. The block diagrams represent the data distribution from the first quartile (bottom) to the median (top), and the error tails show the data distribution from the minimum value to the first quartile.

A separate comparison of rainfall amount at a station closer to the radar gave better results than those of more distant stations (**Figure 4.7**). The figure shows that Sorasan station, located 9.5 km from the X-MP radar, provided a strong relationship, whereas Pucanganom station, located a more distant 13.5 km from the radar, provided the weakest relationship. A deeper analysis of the attenuation problem should be done because the closest station, Ngandong station, provided a closer relationship at 0.96 but a lower $R^2$.

The last potential reason for the underestimation is a "representativeness" error, which is an error caused by the use of a rain gauge to represent a larger radar pixel. The radar rainfall values were consistently smaller than the ARR values, as shown by the median values of X-

MP radar in May and September 2016 being 0.6 and 0.3 lower than the ARR median values, respectively (**Figure 4.8**). This problem is explained by the fact that an ARR represents a point measurement (0.035 $m^2$), whereas radar values represent a 150 m mesh, equal to area of 22,500 $m^2$. Habib et al. (2004) stated that this error depends on the spatial correlation of the rainfall at the sub-pixel scale, such that the correlation of rainfall decreases with the temporal averaging interval as the spatial resolution increases.

The X-MP radar could monitor rainfall depth less than 0.2 mm comparing to the rain gauge measurement. In May, the mean of rainfall depth from the rain gauge data was 1.2 mm, while X-MP radar is 0.4 mm. In September, the mean of rainfall depth from rain gauge was 0.6 mm, and the X-MP radar is 0.3 mm. The consequences are, even so **Figure 4.6** shows the rainfall depth from X-MP radar is almost equal to the rainfall depth measured by the rain gauge, but the rainfall depth values of X-MP radar are two to three times smaller than rainfall depth measured by rain gauge for the rainfall depth values below the mean rainfall depth.

Despite the need to improve the accuracy of X-MP radar, the relationships of the current results are better than those of previous studies using longer C-band and S-band wavelengths, which showed $R^2$ values of 0.51 and 0.48, respectively (Over et al., 2007; Nakaya and Toyoda, 2011).

## 4.4 Materials and Method

4.4.1 Materials

This study combined a semi-distributed model of rainfall-runoff with a numerical model of debris flow to estimate lahar occurrence based on a real lahar event that occurred on 17 February 2016. The materials used in this study are given in **Table 4.4**.

4.4.2 Boundary data generation

Terrain data were pre-processed before applying them into the Geospatial Hydrologic Modeling Extension (HEC-GeoHMS), an extension in GIS developed by the U.S. Army Corps of Engineers. The pre-processing included reconditioning, fill sink, flow direction, flow accumulation, stream definition, stream segmentation, catchment grid delineation, catchment polygon processing, drainage line processing, adjoint catchment processing, drainage point processing, and slope analysis. Stream definition was set to be 1 $km^2$.

HEC-GeoHMS was used to provide input to the Hydrologic Engineering Center's Hydrologic Modeling System (HEC-HMS) by selecting the upstream area of Gendol catchment (**Figure 4.9**). The process relied on a terrain pre-processing dataset to specify the outlet and for running the flow analysis. All procedures were done following the standards of HEC-GeoHMS and HEC-HMS processes.

**Table 4.4** Dataset sources and short descriptions

| Data type | Description | Data source | Used for |
|---|---|---|---|
| Digital surface model | Resolution: 5 m<br>Format: Arc Grid<br>Projection: UTM 49S | ALOS JAXA | Rainfall–runoff model and debris flow model by HyperKANAKO |
| Rainfall intensity [mm/h] of X-MP radar | Resolution: 150 m/2 min<br>Format: ASCII<br>Projection: GWS 84 | X-MP radar cloud system | Rainfall–runoff model and X-MP radar reliability |
| Rainfall amount from rain gauge data [mm] | Time series data with 1-hour resolution<br>Format: csv | Sabo Works Agency | X-MP radar reliability |
| Soil type | Classification of soils<br>Format: database | FAO–HWSD (harmonized world soil database) viewer | Rainfall–runoff analysis |
| Land use/land cover (LULC), 2011 | Classification of coverage and land use<br>Format: kml | The Ministry of Forestry of Indonesia | Rainfall–runoff analysis |
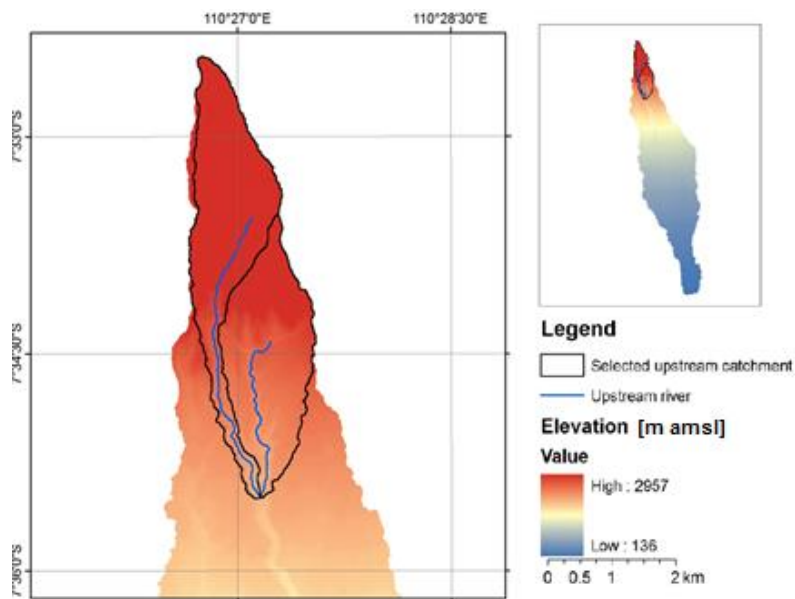


**Figure 4.9** The upstream area of the Gendol catchment that was selected for setting-up the boundary condition.

For each sub-basin, the radar-rainfall intensity, $R$ [mm/h], values were extracted and the rainfall information was assumed to be homogeneous in each sub-basin by selecting the maximum rainfall intensity, $R$, values from the Zonal Statistics toolbox.

The curve number ($CN$) was extracted based on the land use/land cover (**Figure 4.10**) and soil type information for each sub-basin. The curve number values for land use were chosen according to the curve number table by the USDA (1984). The weighted curve number ($CN$) values were calculated according to equation (1).

$$Weighted\ CN = \frac{\sum A_s CN_s}{\sum A_s} \tag{4.1}$$

in which, *weighted CN* is the composite $CN$ used for runoff volume computations, $s$ is the index of basins subdivision of uniform land use and soil type, $CN_s$ is the $CN$ for subdivision $s$, and $A_s$ is the basin area for each subdivision $s$.

The final step was converting the HEC-GeoHMS data into the HEC-HMS input format. A watershed schematic and coordinates (UTM49S) were added to the features before exporting the model. The model for the case of 17 February 2016 was run from 09:00–20:00 local time (UTC+7). Using the Soil Conservation Service (SCS) sub-basin loss method (equation (4.2) - (4.3)), $CN$ values were entered for each sub-basin and 25.0% was entered for imperviousness of surface. Hence, in this case, 75% of falling rain becomes direct runoff. The transform method calculates the actual surface runoff for each sub-basin. The lag time was set for the purpose at 30 minutes. The route method was Muskingum and the base flow was neglected because a field visit to the upstream region of Gendol catchment showed dry conditions (**Figure 4.11**).

$$P_e = \frac{(P - 0.2S)^2}{P + 0.8S} \tag{4.2}$$

$$S = \frac{25,400 - 254CN}{CN} \tag{4.3}$$

Where $P_e$ is accumulated precipitation excess at time $t$; $P$ is accumulated rainfall depth at time $t$; and $S$ is potential maximum retention.

### 4.4.3 HyperKANAKO model

HyperKANAKO is a debris flow model developed by Nakatani et al. (2012). The model is equipped with a geographical information system (GIS) for better output interpretation and is

able to calculate debris flow in 1-dimensional (1D) or 2-dimensional area (2D). The continuity and momentum equations for the phenomena of the *x*-axis direction (flow) and the *y*-axis direction (cross direction) are given as equations (3.8) to (3.9). The change in bed surface elevation was estimated by equation (3.11)
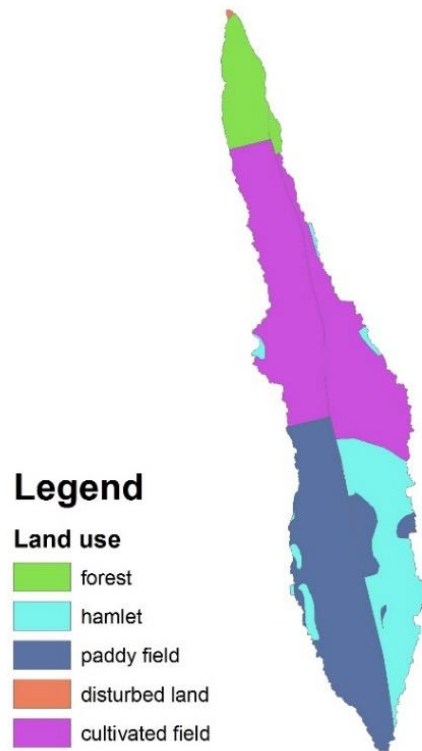


**Legend**

**Land use**
- forest
- hamlet
- paddy field
- disturbed land
- cultivated field

**Figure 4.10** Land use in Gendol catchment.



**Figure 4.11** The dry river in the upstream part of Gendol catchment (1000 m amsl).

The erosion and deposition velocity, *i*, are the source terms related to the sediment concentration, which were described by Takahashi et al. (1992) as given in equations (3.12) and (3.13) respectively.

Erosion and deposition happens during simulation depend on the equilibrium sediment concentration $C_\infty$, described by Nakagawa et al. (2003). This calculation is based on the sediment concentration threshold formulated by Takahashi (equation (3.6)). The bottom shear stress equations for stony-type or dynamic debris flow, immature debris flow and bedload, are calculated based on the slope according to equations (3.20) to (3.22).

The sabo dam scenario was calculated based on Takahashi et al. (2001), where the relationship between the dam height and riverbed height at the dam's upper site determines whether materials will pass over the sabo dam. When a dam's upstream side contains a pocket, material and water can be separated easily and deposited immediately. The slit sabo dam effect was simulated by narrowing the river width between scalar evaluation points upstream and downstream from the vector evaluation point where the slit-type sabo dam was set.

The sabo dam was set at the calculation point of the flow discharge per unit width, *q(i)*, (Figure 6). The elevation of the dam crown, *zl*, was set equal to the sum of the mean bed elevation {*z(i-1)+z(i)*}/2 and the dam height. The flow surface gradient, $\theta_w$, and the effective water depth, *h'* at the dam point which is used to calculate the outflow flux is expressed based on variables in **Figure 4.12** as follows.

$$\theta_e' = \tan^{-1}\left\{\frac{[z(i) + h(i) - zl]}{(\frac{\Delta x}{2})}\right\} \tag{4.4}$$

$$h' = \begin{cases} h(i) + z(i) - zl & h(i) + z(i) - zl > 0 \\ 0 & h(i) + z(i) - zl \leq 0 \\ h(i) & z(i) > zl \end{cases} \tag{4.5}$$

The notations used in the equations are shown in **Figure 4.12**. The gradient, $\theta_e$, is needed to calculate the equilibrium sediment concentration, $C_\infty$, and is evaluated as

$$\theta_e' = \tan^{-1}\left\{\frac{[z(i) - zl]}{(\frac{\Delta x}{2})}\right\} \tag{4.6}$$

When the $\theta_e'$ is less than zero, the equilibrium concentration is set at 0.
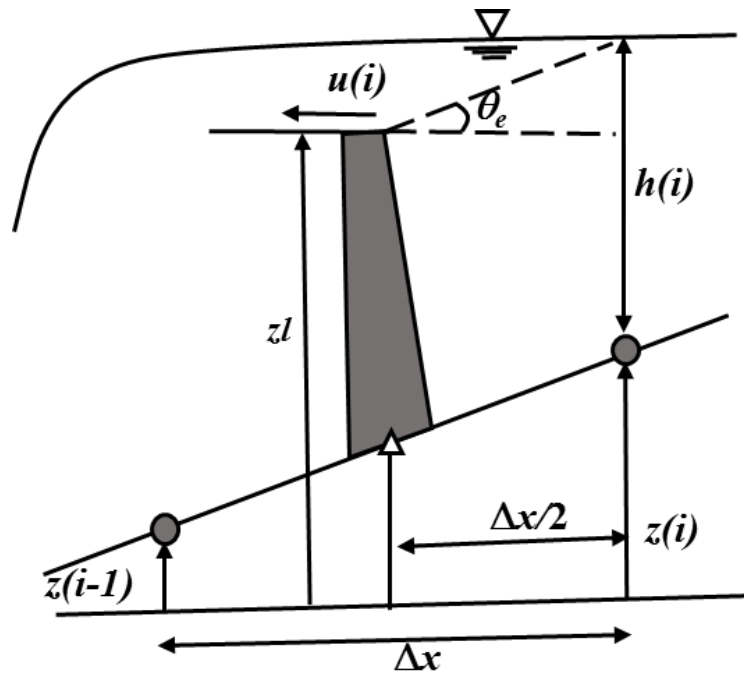
**Figure 4.12** Definition of the gradient used for calculating discharge over the dam.

A flowchart of the HyperKANAKO model simulation procedure is presented in **Figure 4.13**. The following steps are for the debris flow estimation by HyperKANAKO:

1) Preparation

The preparation included creating binary mesh data using the HyperKANAKO tools, calculating the flow input discharge, described in section 4.4.2, and setting up the 1D and 2D areas of debris flow calculation. The binary data were set up by using the conversion program tool provided by the HyperKANAKO program. This tool was used to convert grid points data that consisted of latitude and longitude information from UTM49S as Cartesian coordinates and elevation information for each grid into mesh binary data.

The target 1D stream was set by specifying its upper and lower end points in the GIS and then using the automatic lowest riverbed line drawing function of the HyperKANAKO system. **Figure 4.14** shows an example of setting up the 1D path and the 2D area in the HyperKANAKO model, and **Figure 4.15** shows the longitudinal profile of 1D path. The 1D and 2D upstream elevations were determined based on the HEC-HMS analysis. The 1D path should represent the lower area of the selected sub-basin (below the centroid), close to the elevation of 1200 m amsl, which is used as a requirement of lahar occurrence in the Mt. Merapi volcanic area (Legowo, 1981).
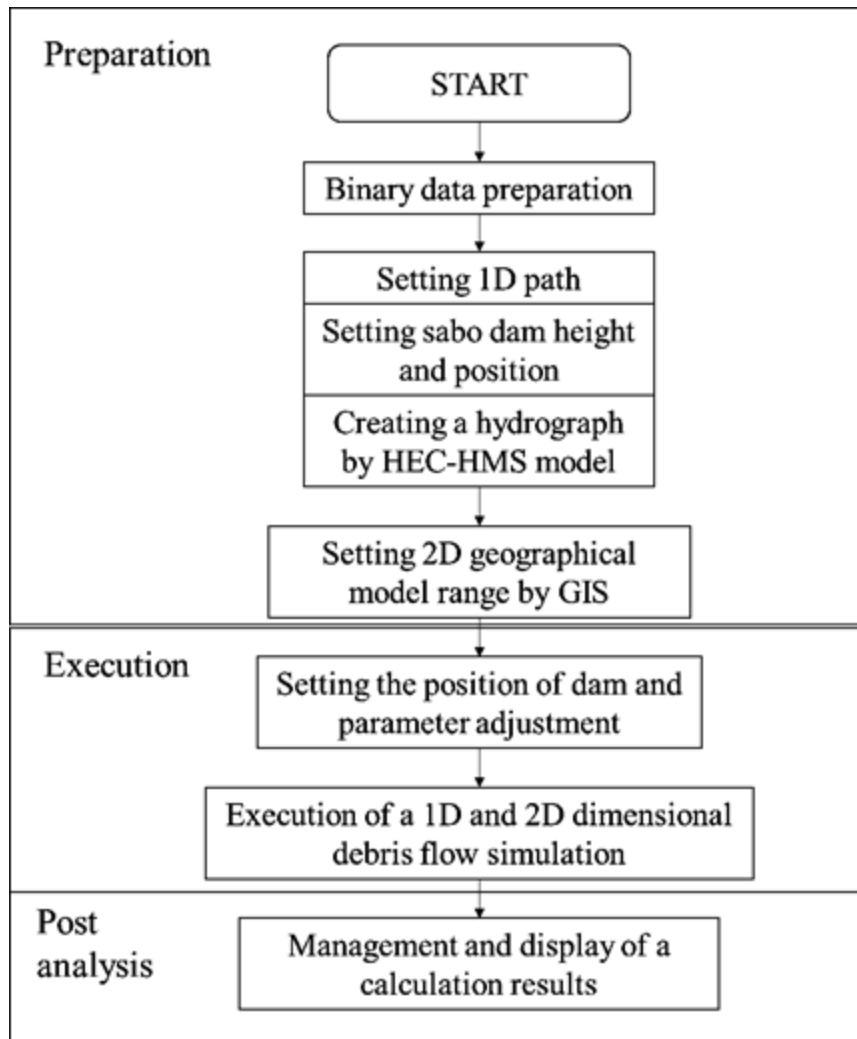
**Figure 4.13** Flow chart of lahar flow simulation by the HyperKANAKO model.
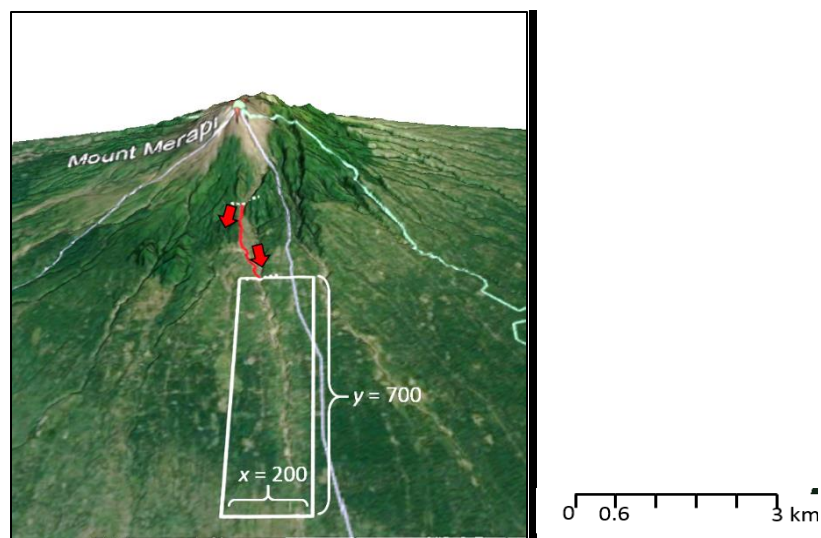


**Figure 4.14** Setting up a 1D path and a 2D area with the GIS tool in the HyperKANAKO model. The red line shows the 1D path, and the white square represents the 2D model
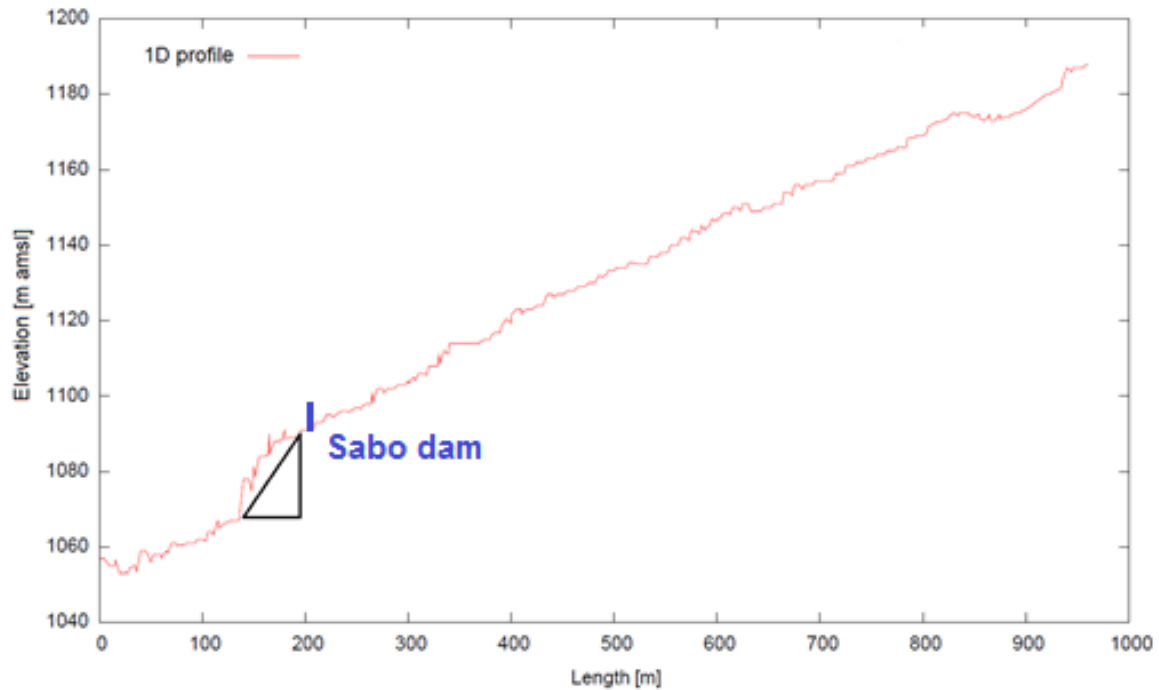
**Figure 4.15** Slope profile of the Gendol catchment from 1200–1068 m amsl and position of the sabo dam for the simulations.

2) Execution

The execution step covered parameter adjustment, sabo dam scenario selection, and running the simulation model. The parameters used in the simulations are listed in **Table 4.5**. The sabo dam could be set at only 1D flow, and three scenarios were applied: no sabo dam (S0), one closed-type sabo dam (S1), and one slit-type sabo dam (S2). The sabo dam for both the closed-type scenario (S1) and the slit-type (S2) scenario was set at an elevation of 1090– 1100 m amsl, which is similar to the elevation of the existing GE-D Kaliadem sabo dam. For the sabo dam scenario calculation, the sabo dams were assumed to be empty and in the most effective condition.

In this study, debris flow was considered to be driven by the erosion, as the historical eruption caused the river in the upstream filled by the volcanic ash. Assuming the erosion process triggering lahar occurrence is in agreement with the fact that the highest erosion rates in the world happens in the drainage basins of active volcanoes (Lavigne, 2004). A good example is in Irazu Volcano of Costa Rica, where the erosion problem is attributed to the accumulation of ash on the upper slopes of the volcano. Furthermore, this ash can form a thin, hard and comparatively smooth crust that is impervious, which makes the upper layer to be eroded easily (Waldron, 1967).

**Table 4.5** Parameters used in the 2D lahar model conducted by HyperKANAKO

| Parameter | Value | Unit |
|---|---|---|
| Simulation time | 8040 | s |
| Calculation time-step | 0.01 | s |
| Output time-step | 60 | s |
| 1D mesh-size interval | 10 | m |
| 1D slope angle | 6.86 | degree [°] |
| 1D river width | 20 | m |
| 1D movable bed layer | 5 | m |
| Manning coefficient | 0.03 | |
| Number of 1D meshes (observation points) | 193 | |
| 2D mesh-size interval | 10 | m |
| 2D mesh number | 200 × 700 | m$^2$ |
| Minimum depth of 2D calculation | 0.01 | m |
| 2D movable bed layer | 5 | m |
| Mean diameter particle* | 0.014 | m |
| 2D average slope | 3.38 | degree [°] |
| Sabo dam height (S1) | 8 | m |
| Slit width (S2) | 3 | m |

* Ikhsan et al. (2010)

Accelerated erosion on the slopes of the volcano was directly related to the increase in the rate of both overland and stream runoff accompanying precipitation. Overland runoff caused sheet, rill, and gully erosion, and stream runoff caused channel erosion. On the other hand, the hydrological and geomorphic character of lahar at Mt. Merapi exhibits strong erosive force relative to the fluid density, hydraulic depth, and to the shear stress that is six times greater than the stream flow on the channel (Lavigne and Thouret, 2003).

Although HyperKANAKO is intended to calculate the 2D area as deposition zone, the existence of erodible layer in the 2D area in this study is also considered. This assumption is to represent the wide channel of the river and the availability of volcanic ash deposition in the downstream, as for the case of 2010 eruption, the pyroclastic flow could reach 15 km

from the summit. The remaining volcanic materials from pyroclastic flow were known to change the riverbed profile and destroyed many villages along Gendol channel.

The manning roughness coefficient of the model in **Table 4.5** was higher than previous recommended values by de Haas and Van Workoem (2016), where 0.02 gave the best correlation between measured flow velocity of experimental debris flow compared to the outcomes of Manning's equation based model. In this simulation Manning coefficient of 0.03 is usually used to represent natural stream roughness (Chou, 1959). However, another study (de Haas and Van Woerkom, 2016) has suggested higher values of manning roughness coefficient to represent the larger bed roughness in natural streams caused by the presence of bed forms, step-pools and large boulders in the channel.

3) Post analysis

The results, which were numerical and image data, could be viewed directly using the GIS program that accompanies the HyperKANAKO model. A 3D display (aerial view) is also possible by some GIS processing programs. Post analysis of the numerical results was done for three parameters, water depth, sediment accumulation, and frontal velocity, to obtain information pertaining to the effect of the sabo dams as a lahar countermeasure.

## 4.5 Results and Discussion

### 4.5.1 Rainfall and lahar event on 17 February 2016

The average spatial rainfall distribution in the Gendol catchment for the rainfall event of 17 February 2016 is presented in **Figure 4.16.** The lahar flow in the upstream part of Gendol catchment swept away a truck and a car. An approximately 200 mm increment of water level was measured in the downstream area at the elevation of 144 m amsl (**Figure 4.17**). We consider this small increment to be the result of local rainfall in the sub-basin where the AWLR is installed and not the result of lahar flow. Hence, the lahar occurred only in the upstream portion of the catchment and its flow path did not reach the downstream area.

The average rainfall intensity measured by X-MP radar for 1 h in the upstream area was 36.58 mm/h, and the accumulated rainfall amount in 2 h was 42 mm. **Figure 4.16** shows that the upstream area experienced more intense rainfall than the downstream area. Lavigne et al. (2000b) stated that lahar risk at Mt. Merapi is still hazardous following 40 mm of rainfall in 2

h. The accumulated rainfall values of this event are larger than this threshold, so lahar flow was likely to happen.
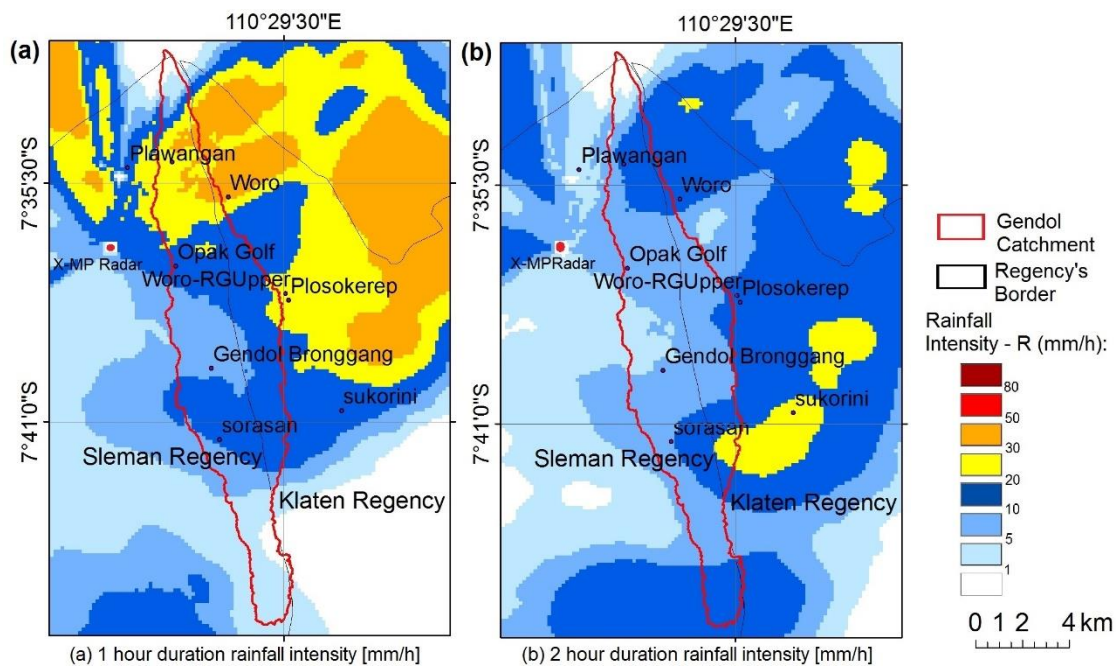


Figure 4.16 Average rainfall intensity on 17 February 2016 at Gendol catchment for a 1 h duration (a) and 2 h duration (b) measured from 15:30 to 16:30.
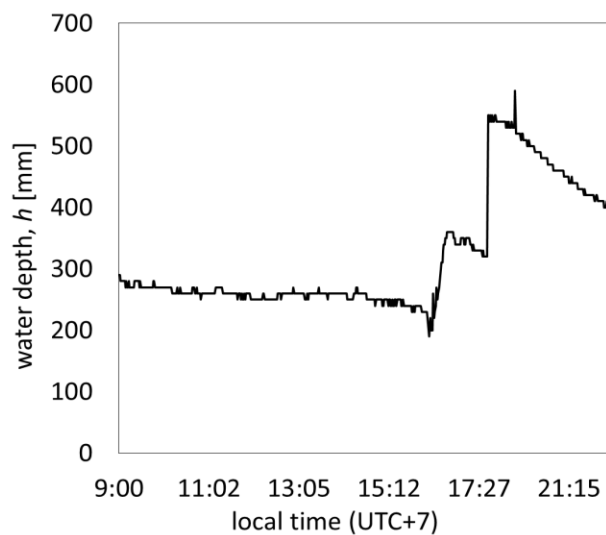


Figure 4.17 Water depth recorded on 17 February 2016

4.5.2 Boundary condition of the upstream portion of the Gendol River

The upstream region of the Gendol catchment consists of 2 sub-basins with a total area of 5.58 km$^2$ (Figure 4.18). Table 4.6 lists the characteristics of each sub-basin. Most of the area is forest, and the soil type is Regosol with a homogeneous profile and a sandy to loamy sand texture as the result of volcanic activities.

For simulation, we used sub-basin A, which has a steeper slope and a centroid higher than 1200 m amsl, that is known to be elevation of lahar initiation (Legowo, 1981). The average slope is also higher (6.86°) compare to sub-basin B (4.69°), and according to equation (3.15), this degree of slope is possible to generate the immature debris flow.

The HEC-HMS model simulated the rainfall–runoff process based on radar rainfall values. The rainfall variability within the sub-basins was based on the maximum rainfall intensity of the radar rainfall. The maximum rainfall intensity in each sub-basin was used not only because of the problem of smaller values of rainfall intensity of radar rainfall data compared to the gauged data but also to describe the worst case of the rainfall condition. The time-step of simulation was based on an X-MP radar 2-minute temporal resolution, which was required to cover the rapid changes in lahar occurrence and the lahar characteristics.

**Figure 4.19** presents the hydrograph of the upstream Gendol catchment from the HEC-HMS model. The maximum rainfall intensity, which occurred at 16:20, was 69 mm/h, whereas the maximum discharge, which occurred at17:10 local time, was 41 cm. The hydrograph was applied in the HyperKANAKO model for the simulation period starting at 15:30 for 8000 s. The 1D model was set at 1200 to 1060 m amsl, and the 2D area extended from 1060 to 800 m amsl.
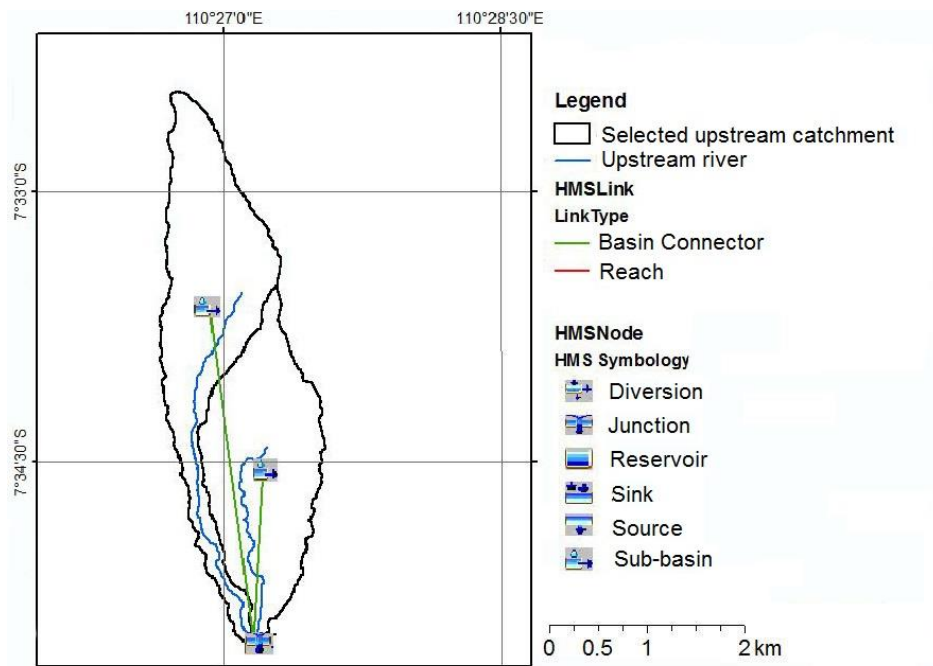


**Figure 4.18** Data preparation for calculating the boundary condition in the upstream portion of Gendol catchment by HEC-GeoHMS.
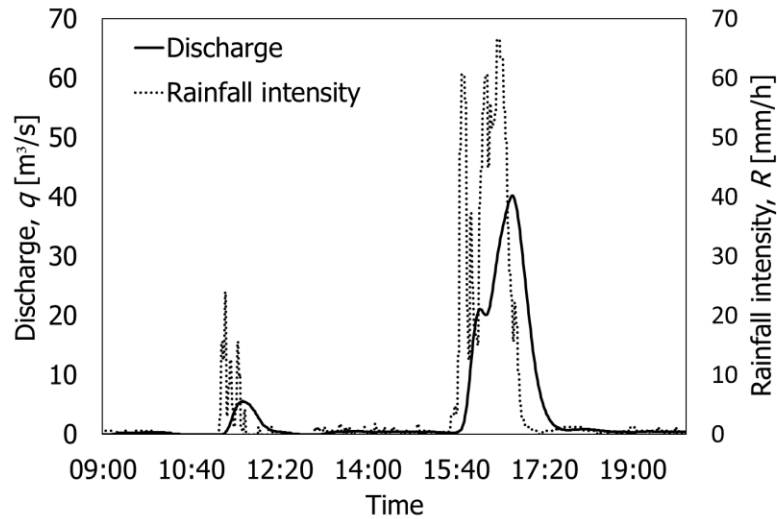
**Figure 4.19** Hydrograph of upstream Gendol catchment for the boundary condition of HyperKANAKO Model, calculated by Hec-HMS model

**Table 4.6** Sub-basin characteristics extracted from 5 m DSM ALOS

| Characteristic | Sub-basin A | Sub-basin B |
|---|---|---|
| Area [km²] | 2.92 | 2.65 |
| Max elevation [m amsl] | 2957 | 1600 |
| Minimum elevation | 941 | 941 |
| Average basin slope [º] | 20.71 | 11.76 |
| Average river slope [º] | 6.86 | 4.69 |
| River length [km] | 4.38 | 2.52 |
| Upstream river elevation | 1609 | 1204 |
| Downstream river elevation [m amsl] | 941 | 941 |
| Land use and land cover, LULC | Forest | Forest and cultivated area |
| Average sub-basin $CN$ | 34.85 | 56.13 |
| Sub-basin centroid [m amsl] | 1560 | 1214 |

### 4.5.3 The HyperKANAKO simulation results

1) Effect of sabo dam on frontal velocity

**Figure 4.20** shows the sabo dam effects on the maximum velocity of the 1D and 2D along the simulation path, while **Figure 4.21** shows the magnitude of frontal velocity at the end point of simulation which are 1070 m amsl and 820 m amsl respectively. In general, the lahar flow for all scenarios occurred as series of intermittent bore-like flows (surges) marked by a significant sudden increment of frontal flow velocity (Takahashi, 2014). The closed

type sabo dam scenario (S1) gave a 40 min delay of the surges but had the relatively same velocity as the other two scenarios at the end of simulation. The slit type sabo dam (S2) gave the highest velocity at 3.2 m/s and showed the occurrence of three surges in the 1D simulation within 31 min. All of the scenarios gave at least two surges in the 2D simulation. It is assumed that the highest velocity shown by the slit type sabo dam scenario (S2) was caused by the effect of narrowing the channel of the slit.

A lahar is a type of debris flow that is often described as a sequence of surges that progresses down and causes devastation along a river valley. Precise documentation of such surges and attribution of this phenomenon are rare but have been documented in many prototypes and in field monitoring and laboratory experiments (Zanuttigh and Lamberti, 2007).

Takahashi (1999) monitored debris flows in Jiangjia Ravine, China, and reported that tens to hundreds of surges emerged repeatedly at time intervals of a few tens of seconds to a few minutes. Between the surges, the flow stopped completely. Lavigne and Thouret (2002), who recorded lahar magnitude at Mt. Merapi by using seismic spectral amplitude measurement (SSAM) and an acoustic flow monitoring (AFM) instrument, also confirmed such surge behavior. Takahashi (2009) then argued that this showed that the Bingham fluid model and other viscoplastic fluid models are probably not applicable to debris flow behaviour analysis.

HyperKANAKO model was based on Takahashi model of a steady uniform open channel flow of grain-water mixture under simple gravity driven shear for Bagnold's grain inertia and macro-viscous regimes (Takahashi, 2014). The model considers the mixture of fluid and solid as a kind of continues fluid whose properties implicitly reflect the fluid particles interaction effect.

Solid particles were assumed to have uniform distribution throughout the depth. A mean diameter of solid particles was used and the grains are assumed to be heavier than water. Because of this characteristic, they tend to be deposited. Some mechanisms to disperse the grain are required to keep the flow going, and in the case of Takahashi model, they are the rapid shearing and the threshold concentration. The shear stress equals to the square of velocity rate which is known as dilatant fluid model (Takahashi, 2014), while the concentration is calculated according to equation (3.14).
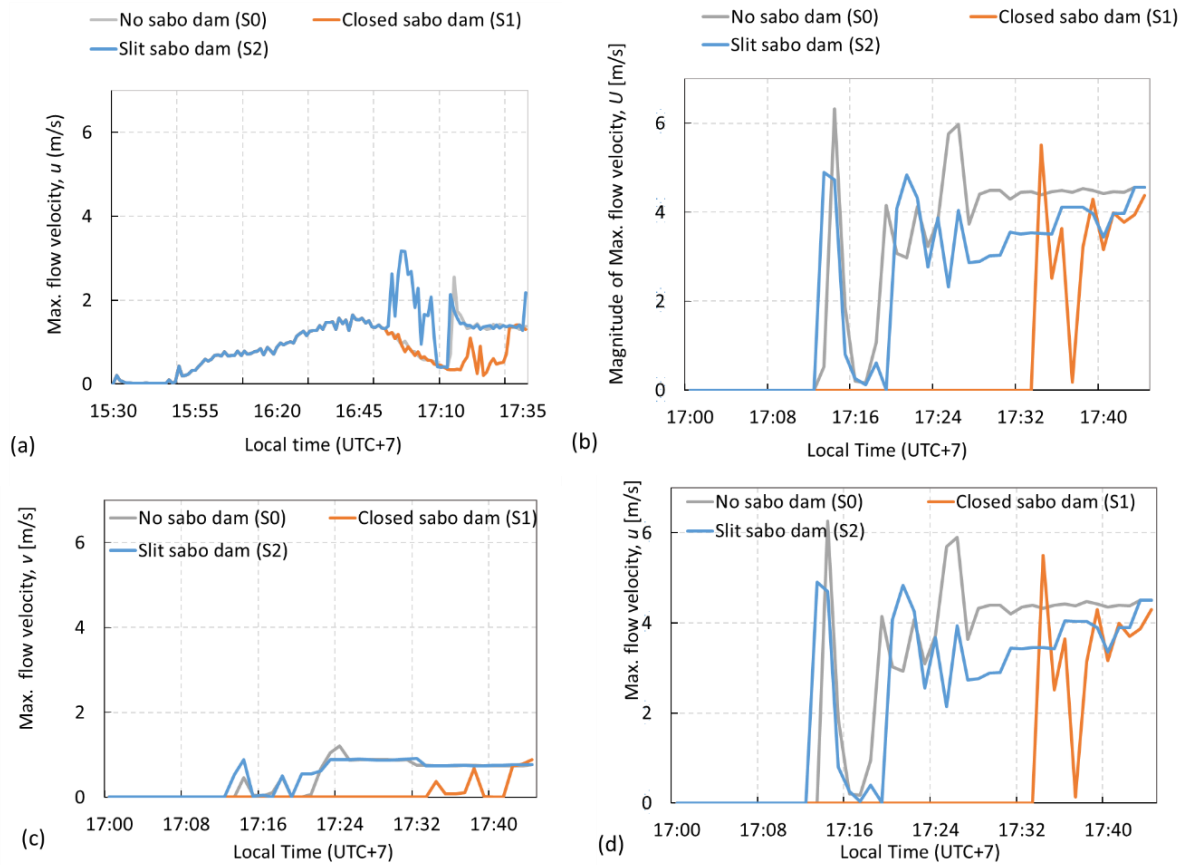
**Figure 4.20** Effect of the sabo dam scenarios on maximum flow velocity in the 1D simulation (a), magnitude of maximum flow velocity in the 2D simulation (b), maximum flow velocity parallel to the streamline (c), and parallel to the cross section of the river (d).



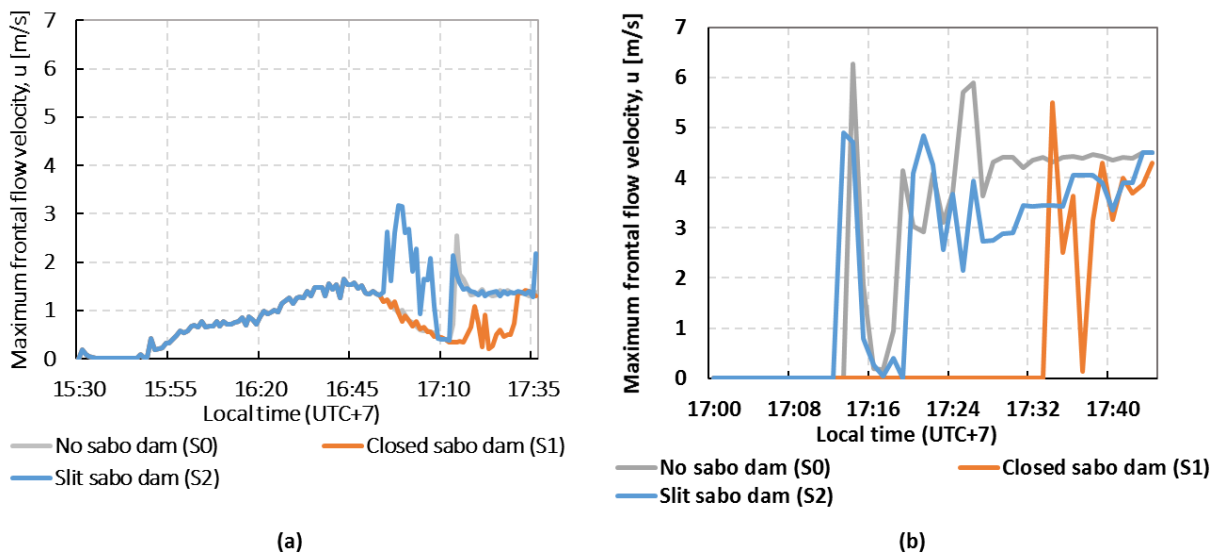**Figure 4.21** Effect of the sabo dam scenarios on maximum frontal velocity at the end of the simulation path for the 1D simulation at 1010 m amsl (a), and the 2D simulation at 810 m amsl (b).

Although the constitutive response of this regime is essentially Newtonian type, however, this kind of model is understood as an equivalent model to the two-phase mixture model in which the dynamic fluid effects are almost negligible (Takahashi, 2014; Hutter et al., 1994). Hence, it is able to demonstrate the surge occurrences similar to the two phase model which involved the sorting particles and the interaction amongst them once the threshold is satisfied.

Applying the other single-phase fluid such as Bingham fluid model has not resulted in surge-type behavior, as exemplified by the study of de Blasio et al. (2004) on debris flow simulation of overconsolidated clay materials. The simulation did not evolve in surges but showed a very strong dependence on the initial mass. A decrease of flow duration and velocity were marked in the flatter part of the path as the yield strength increased. A Bingham fluid model will only deform if the operating shear stress is larger than the threshold, where it will behave as if it were a Newtonian fluid (Takahashi, 2014). The Bingham rheology does not count the grain-grain and grain-fluid interaction that dictate the mechanics of flowing debris, hence the application is limited only to the mud-rich debris flows (Whipple, 1997).

The 1D simulation was calculated at an area with elevation ranging from 1200–1060 m amsl, while the 2D area started at an elevation of 1060 m amsl and extended to 800 m amsl. **Figure 4.20** and **Figure 4.21** indicate that frontal velocity in the 1D calculation was lower than in the 2D calculation. Based on **Figure 4.20**, the flow started to become a 2D flow after 17:10 for the scenarios of no sabo dam and slit-type sabo dam and after 17:25 for the scenario of closed-type sabo dam. At those times, the lahar flow became slower, and the values of the 1D simulation were used as the boundary of 2D simulation. The 1D simulation showed a maximum frontal velocity in the end point of simulation at 17:10 is very small at 0.01 m/s (**Figure 4.20 (a)**) which caused the same values to be used in the 2D calculation (**Figure 4.20 (b)**).

Greater magnitude velocity in 2D model are caused by the flow velocity parallels to the cross section of the river (**Figure 4.21**). The 2D model calculates both shear stress in 2 directions according to equations (3.20) to (3.22). In these equations, the slope plays important role on the sediment concentration and shear stress calculation. As the slope angle of cross-sectional river is much smaller than slope parallels to the river flow direction, the

flow velocity calculation in the *x*-direction (cross-section of the river) is mainly calculated by equation (3.22).

Equation (3.22) is in principle a Newtonian fluid equation that used Manning roughness coefficient. Because of the small Manning roughness coefficient (0.03), the shear stress becomes smaller resulting in greater flow velocity happened in the *x*-direction comparing to the flow velocity which parallels to the river flow (mainly in *y*-direction).

Although previous studies have successfully used the Manning equation in debris flow calculation but most of them suggested higher value of Manning roughness coefficient. Values of 0.05-0.10 are the most recommended coefficient for debris flow studies (de Haas and van Woerkom, 2016). Lavigne and Thouret (2003), measured the Manning roughness coefficient of rivers at Mt. Merapi for debris flow happened in 1995 were 0.122-0.641. Moreover, the river channel has various width, ranges from 10-60 m causing the effect of surface roughness can play important role due to the changing of cross sectional and hydraulic radius along the channel (Jarret, 1985). Hence, adjusting the Manning roughness coefficient for 2D model of debris flow is essential in the future studies.

At the end of the simulation, the velocity became relatively stable when the flow reached the downstream area for the case of slit-type and no sabo dam scenarios. The relatively stable flow velocity happened because the model uses the Newtonian fluid model in the deposition area which caused the flow to become less turbulent. However, in the calculation the erosion process in 2D area was allowed by involving 5 m thickness of erodible layer (**Table 4.5**).

The same result of sudden discharge increment followed by relatively constant to decreasing rate was presented by Kim et al. (2014), who also used the Takahashi equation for debris flow simulation. The closed sabo dam scenario on the other hand, showed a trend of increasing velocity at the end of simulation, which may indicate that this scenario does not reduce the velocity but only postpones the flow due to the empty sabo dam assumption used in the simulation.

The verification of this result was done qualitatively because an AWLR was not available in the upstream area (**Figure 4.16**). We compared the time of lahar occurrence with the information gathered from the weekly report of Mt. Merapi produced by CVHGM. The time

of the lahar occurrence was reported as 17:20–17:40, which is similar to the scenario of the closed-type sabo dam (S1). Although there is possibility that the model overestimated the flow velocity due to the small manning roughness coefficient used in the simulation, however by adjusting the roughness coefficient in the future, this simulation has shown the potency of remote monitoring for a lahar early warning system.

2) Effect of sabo dam on sedimentation

The sabo dam was set at the point in the 1D path at 1090–1100 m amsl, and its effect on trapping sediment is presented in **Figure 4.22**. At the elevation where the sabo dam was designated, the highest erosion rate occurred in the scenario without a sabo dam (S0) and in the scenario with a slit type sabo dam (S2), and the erosion was followed by high deposition at lower elevation. The closed type sabo dam gave a lower erosion value and yielded less sediment at the end of the 1D path compared to the slit–type dam.

The profile of the 1D slope shows a significant change in steepness at 1080–1090 m (**Figure 4.15**), resulting in a large amount of eroded material being transported to the downstream for all of the scenarios. As the closed type (S1) scenario had a smaller amount of sediment accumulation carried by the flow, the deposition at lower elevation was less than for the other two scenarios.
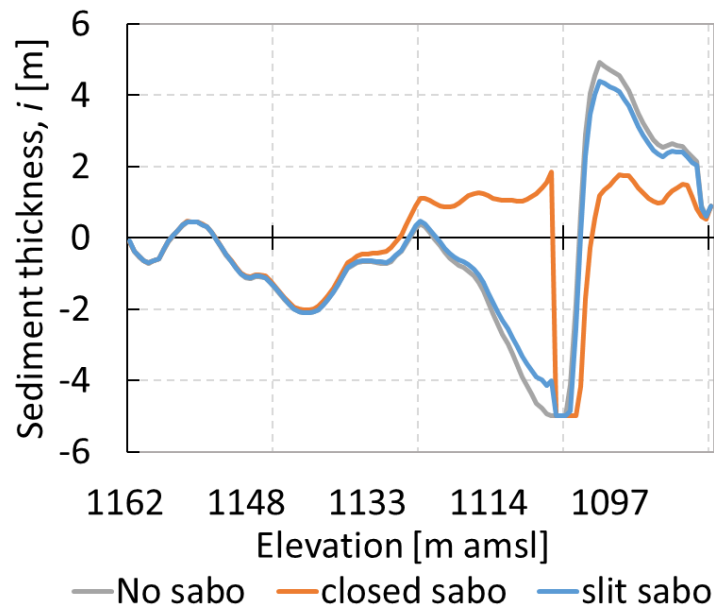


**Figure 4.22** Sediment thickness and depth of erosion in the 1D simulation.
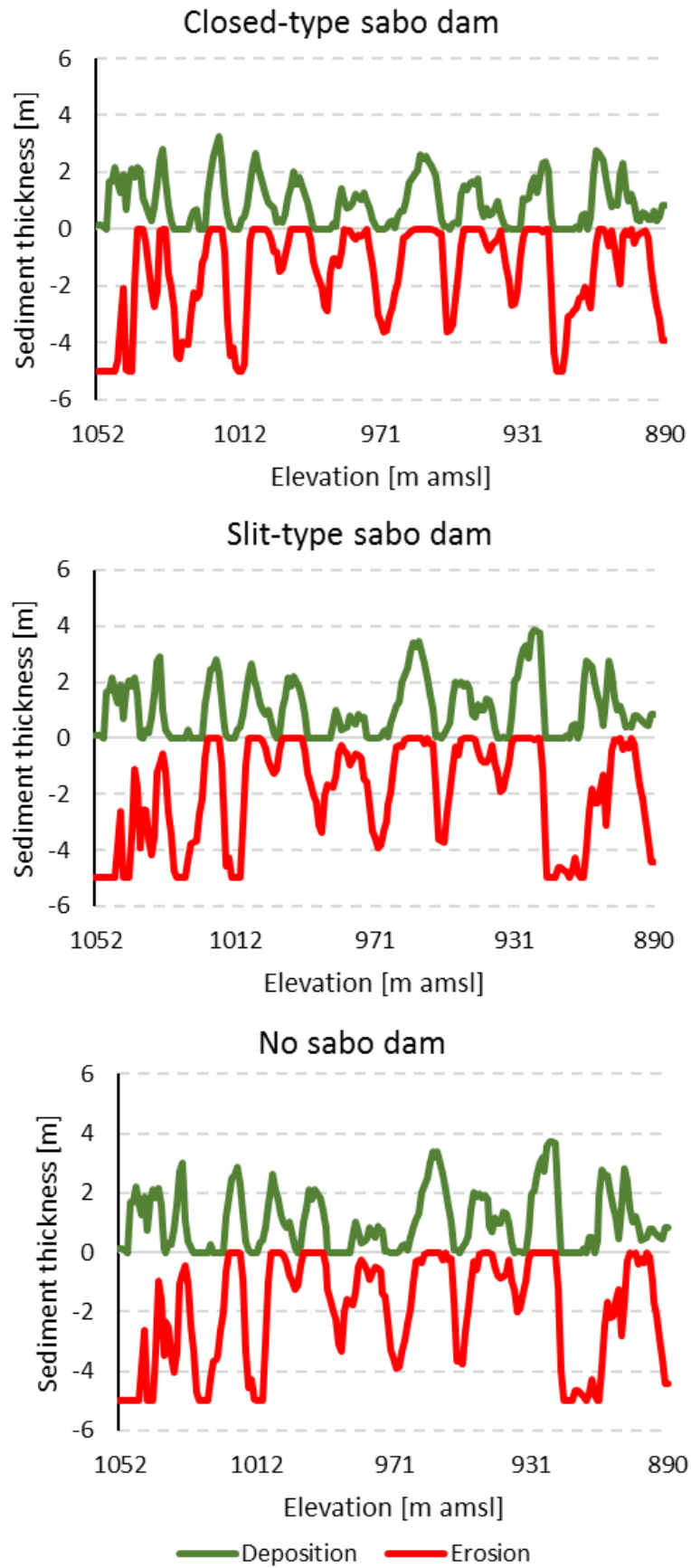
**Figure 4.23** Sediment thickness and depth of erosion in the 2D area.

The empty closed-type sabo dam was effective to trap the sediment and postponed the flow. However, after the sabo dam was filled with sediment, the velocity increased and caused higher erosion rate in 2D calculation. The feature of closed-type sabo dam to trap the sediment has sometimes caused environmental problem, where the sediment should be removed mechanically and caused overtopping for the following debris flow happened (Takahashi, 2014).

The higher sediment accumulation carried by the slit-type sabo dam in 1D calculation dam occurred because of the slit-type sabo dam has little effect on sediment discharge decrement (Sumaryono et al., 2009). In their study, closed-type sabo dams could reduce coarse sediment up to 7 times greater than slit-type sabo dams. However, the efficiency of closed sabo dam decreased after it was filled with sediment, which caused discharge increment and consequently higher erosion and deposition rate in the downstream.

All of the scenarios used in the 2D calculation showed a maximum sediment thickness of 3 m and an eroded layer carried by the flow of 5 m (**Figure 4.23**). The closed-type sabo dam resulted in lower sediment accumulation due to a smaller supply from the 1D simulation, and also higher flow velocity rate in the 2D calculation which caused higher erosion rate compared to the other scenarios. Both the slit-type sabo dam scenario and the no sabo dam scenario gave the same amount of sediment, which is similar to the tendency of water depth. This indicates that the flow behavior depends on the amount of sediment carried within the flow. Less sediment would increase the water depth in the 2D area as the flow becomes less viscous in agreement with the Newtonian fluid assumption.

Others studies conducted by using a 2D numerical model of debris flow also excluded the effect of dam break when addressing debris flow calculation (Hsu et al., 2010; Wu et al., 2013). The Hyper KANAKO using Takahashi model can consider the debris flow, immature debris flow, and bed load in 2D area. Debris flow occurrence or development due to the erosion can also be considered. The effect of sabo dam is not considered in 2D area because it considers the 2D calculation as a deposition process as the debris flow's velocity gradually stops, and it is also to calculate the inundation area affected by debris flow.

A sabo dam is usually constructed in a steeper area because of its main function is to change the river slope profile to reduce flow velocity. However, the rivers on Mt. Merapi and the lahar characteristics have different features, such that they have wide river width and the

sabo dams are constructed in areas that are relatively not very steep. An improvement of HyperKANAKO by using 2D numerical concrete sabo dam-break erosion by overtopping flow could be valuable because rivers below 1000 m amsl in the MVA are more suitable for 2D simulation due to the region's wide river width and flatter slope. Using the 2D dam-break numerical model was found to give good agreement with experimental results (Awal et al., 2008).

The current study addressed the remaining volcanic material that was deposited in the upstream area, where the steepness of the slope is high. This made the current calculation using the 1D numerical model as the initial process reasonable because the river width is not as wide as in the downstream area and the flow is more affected by gravitational force.

Eruption remains a threat for the people who live on Mt. Merapi. The 2010 eruption released volcanic ash that reached distances of more than 7 km from the vent. This area has wide river width, but the slope is still potential for debris flow occurrences (3.38°). This fact is supported by previous lahar reports on Mt. Merapi after the 2010 eruption (Lee et al., 2015).

3)  Water depth in the 2D area

The water depth distribution in the 2D area is given in **Figure 4.24**. Although the scenario without a sabo dam (S0) generally gave a higher frontal velocity in the 2D simulation area, the effect of the slit-type sabo dam (S2) on water depth was not different than the no sabo dam scenario. In these two scenarios, lahars reached their maximum water depth at elevations higher than the downstream area, making the upstream area more prone to lahar disaster.

On the other hand, the closed-type sabo dam gave a relatively same water depth within the stream. As the water depth decreased in the downstream area in the other two scenarios to 1.13 m depth and elevation lower than 950 m amsl, the water depth in the closed-type sabo dam (S1) scenario still reached the height of 2 m. This means that the frontal velocity in the closed sabo dam scenario was higher than those of the other two scenarios, which is confirmed by **Figure 4.21**. In **Figure 4.21**, the first surge in the 2D simulation of the closed-type scenario with a frontal velocity of 5 m/s started at the time when the other two scenarios were becoming slower and relatively stable at a velocity of 3–4 m/s. This is the main reason for the flow increment in the closed type sabo dam (S1) scenario.
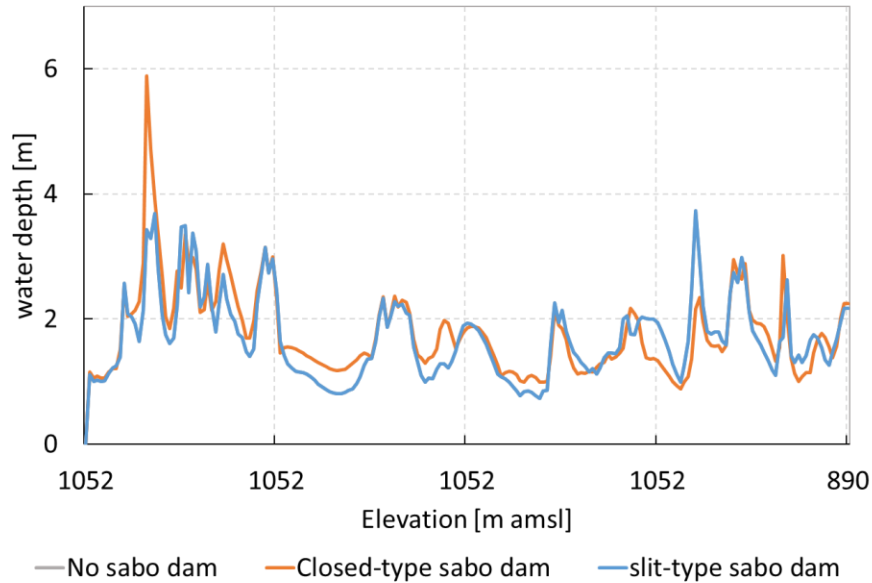
**Figure 4.24** Water depth of lahar based on 2D simulation.

The 2D simulation was performed in the downstream area where the slope was relatively flatter (**Table 4.6**). Therefore, the simulation considered the flow to behave as bed load transport. In the flatter area, the calculation was based on the Newtonian fluid principle. This made the flow move slower when the yield concentration of the solid phase increased. Sedimentation in the no sabo dam and the slit-type sabo dam scenarios was higher than in the closed-type scenario, which explains the lower velocity and shallower water depth in the downstream area compared to the closed-type scenario.

## 4.6 Summary

An example of applying a debris flow numerical model at the catchment scale was done in Gendol catchment of Mt. Merapi. Application of the model required rainfall information for the upstream catchment that could be provided by X-MP radar. The rainfall amounts from X-MP radar were mostly underestimate compared to the rainfall amounts measured by ARR. Therefore, we applied the maximum rainfall intensity, $R$, estimated from X-MP radar to generate discharge in the boundary condition in the numerical model of debris flow, HyperKANAKO.

The simulation was able to estimate the occurrence of a historic lahar at almost the exact time. It was also shown that applying a closed-type sabo dam could reduce the frontal velocity and sediment accumulation in the downstream area of 1D calculation. However, the erosion happened in 2D simulation was greater compared to other scenarios, as we assumed that the

efficiency of closed-type sabo dam was decreased after it was filled with the sediment which led increasing frontal velocity at the end of the simulation. Although quantitative validation is still required, this study provides benefits for remote disaster management of lahar in terms of evacuation time and for lahar countermeasures due to the use of the sabo dam.

# CHAPTER V
# SHORT-TERM ENSEMBLE RAINFALL FORECASTING AT Mt. MERAPI

## 5.1 Introduction

Numerous studies have agreed that debris flow and/or lahar events could happen rapidly as a response to intense rainfall events. According to de Belizal et al. (2013), the duration of lahar occurrence in Gendol River of Mt. Merapi usually happens in less than 1 hour. Moreover, Levigne et al. (2003) also found that the lahar peak in Kaliurang River (Boyong River) occur 30 minutes before or after the peak of a rainfall event.

Previously, very limited debris flow studies have been conducted in term of short response toward short-range rainfall forecast. Most of the studies are concentrated in the regional long-range forecast of debris flow (Wei et al., 2006). Cannon (1982) was concentrated in regional rainfall-threshold condition for debris-flow. Other studies were also based on the study cases of real debris flow/lahar events by several methods such as remote sensing (Wilson, 1997) or direct observation of rainfall and following lahar events (Lavigne et al., 2000b) without incorporation of model simulation.

However, many recent studies have found the importance of short-term rainfall prediction for real-time urban basins response for severe rainfall event. Short-term rainfall forecasting or known as now-casting deals with a short-term prediction for a few hours of rainfall in contrast to the medium-term (few hours out to 14 days) and long-term (2-weeks out to 3-months or more).

Unlike the long-term forecast, which is usually applied for agriculture planning or drought management (Syarifuddin et al., 2015), the short-term forecasting is essentially required for real-time flash-flood forecasting in an operational hydrology (Hapsari, 2011). However, its application on debris flow and lahar monitoring is relatively unexplored. Wei et al. (2006) prove the ability of Numerical weather forecast for regional debris flow forecast. However, they also do not recommend its application for debris flow happens due to the local rainfall or storm rainfall induced by local severe convection weather.

Considering the tendency of tropical rainfall characteristic at Mt. Merapi and the rapid time of lahar surges occurrence, applying a short-term rainfall prediction is a promising method for early monitoring of lahar. This idea is also similar to the basic concept of the warning of sediment disaster method in Japan (Chen and Fujita, 2013). The basic concept of sediment disaster warning method in Japan is determined by the long-term rainfall index of rainfall related to its short-term rainfall index. A warning will be issued if the forecasted rainfall exceeds the critical line (**Figure 5.1**).
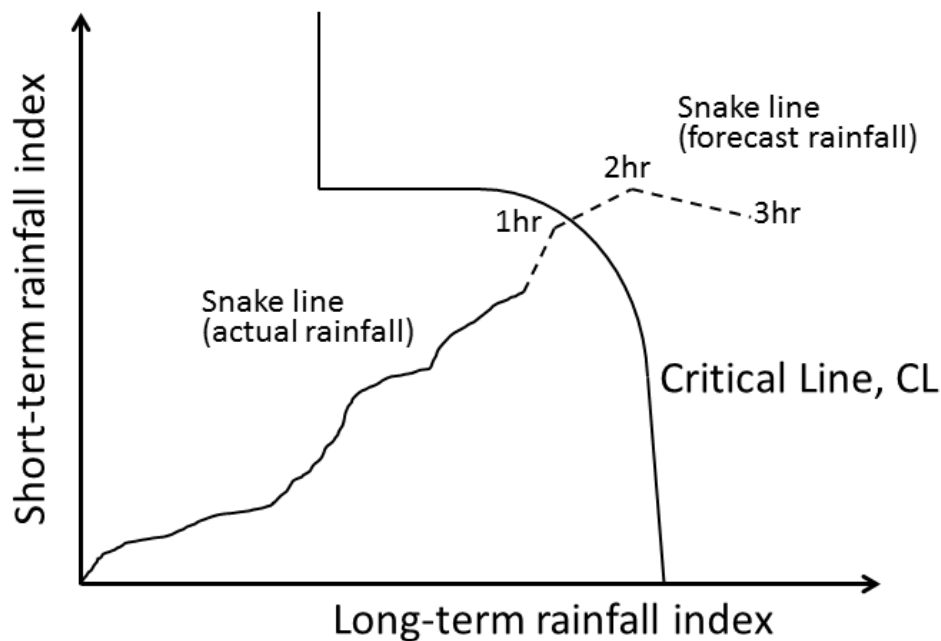


**Figure 5.1** Basic concept used for the warning models of sediment disaster in Japan (MLIT, 2004).

In this chapter, a short-term rainfall prediction by advection model developed by Shiiba et al. (1984) and its ensemble forecast developed by Hapsari (2011) is applied to a rainfall event happened at Mt. Merapi. This method could give valuable information of severe hydro-meteorological condition in a small catchment that is required by a small-scale event of lahar.

This chapter objective is to do a short-term lahar potency assessment based on the rainfall prediction. The rainfall prediction is done according to the short-term rainfall by ensemble model. The result of the ensemble rainfall prediction is plotted to draw the snake line. The study case used is the real lahar event happened in Gendol catchment on 17 February 2016. This application is done to know the feasibility of short-term rainfall forecasting and the existing critical line equation in the early warning system of lahar.

## 5.2 Critical Rainfall for Lahar Assessment

5.2.1 Critical line based on MLIT (2004) method

Rainfall intensity is the main factor of the secondary lahar generation in Indonesia. The studies of lahar generation and the optimal rainfall to initiate lahar were conducted statistically and numerically. Most of the studies were concentrated in the critical rainfall assessment in terms of warning and evacuation process (Fitriyadi, 2013; Yulinsa, 2015; Kusumawardhani et al., 2016).

The critical rainfall is useful to identify the critical line that analyzes the relationship between rainfall intensity and working rainfall for lahar or debris flow initiation. Rainfall intensity is the depth of rain falling into the ground surface per unit time, usually in mm/h and mm/day, while working rainfall (RW) is a cumulative rainfall which affected by the antecedent rainfall. In general, debris flows or lahars occur under the influence of not only rainfall intensity but also antecedent rainfall. This method is composed by Ministry of Land Infrastructure and Transportation (MLIT) of Japan (2004), as given in **Figure 5.2**.
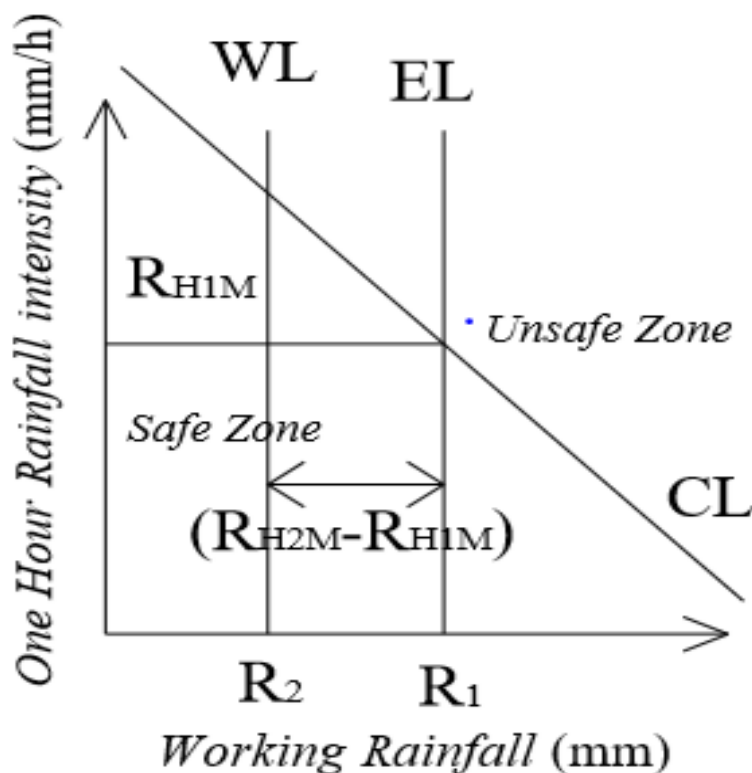


**Figure 5.2** Critical line based on MLIT (2004)
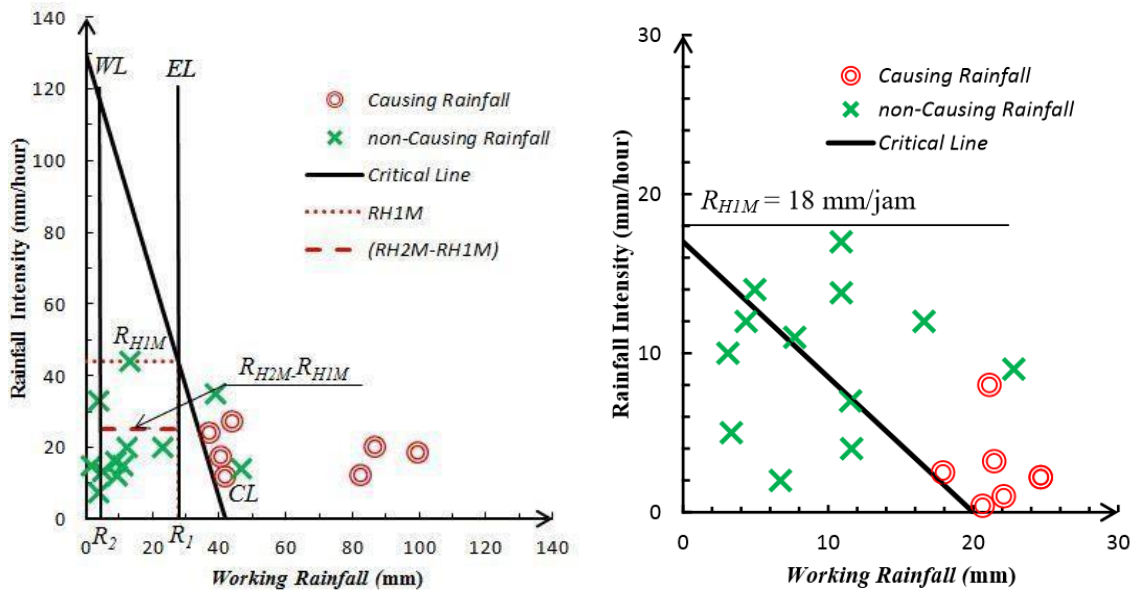
**Figure 5.3** Critical line estimation in based on MLIT method in Putih River (Yulinsa, 2015)
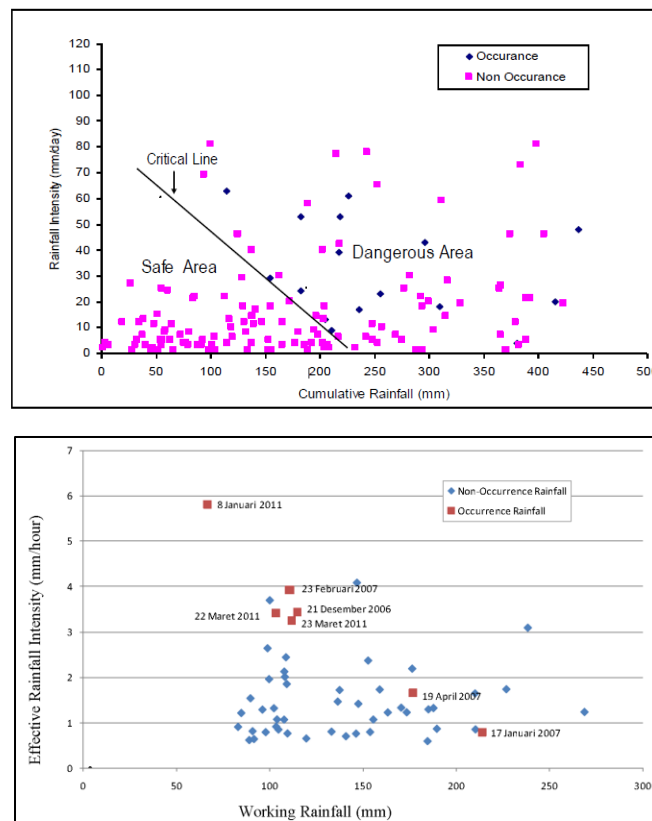


**Figure 5.4** Rainfall characteristic vs. sediment migration at Gendol River by Manonoma (2009) (above), and by Fitriyadi (2010) (below).

Critical line (CL) is the boundary line drawn between rainfall events either causing the lahar or non-causing the lahar (MLIT, 2004). Determining the CL means to make a boundary line between rainfall events causing the lahar or non-causing the lahar. The maximum rainfall from hourly rainfall (RH1M) from the line is drawn horizontally then being intersected with CL to

get $R_2$, in which the vertical line serves as the evacuation line (EL). The evacuation line (EL) extends a bit to the left as much as RH2M-RH1M in which RH2M is the maximum rainfall from bi-hourly rainfall resulted in the warning line (WL) and $R_1$ as the triggering rainfall for disaster signals. Snake line is a line showing the changes of cumulative rainfall and rainfall intensity as shown in **Figure 5.1**. Some other studies about the lahar's critical line analysis by using the MLIT method in Merapi volcanic area had been done and presented in **Figures 5.3-5.5**.



**Figure 5.5** Critical line at Gendol River (above) and setting of CL, WL and EL at Gendol River (below). The rainfall series used in the analysis was based on rainfall data collected from Batur Station (Fibriyantoro, 2015)

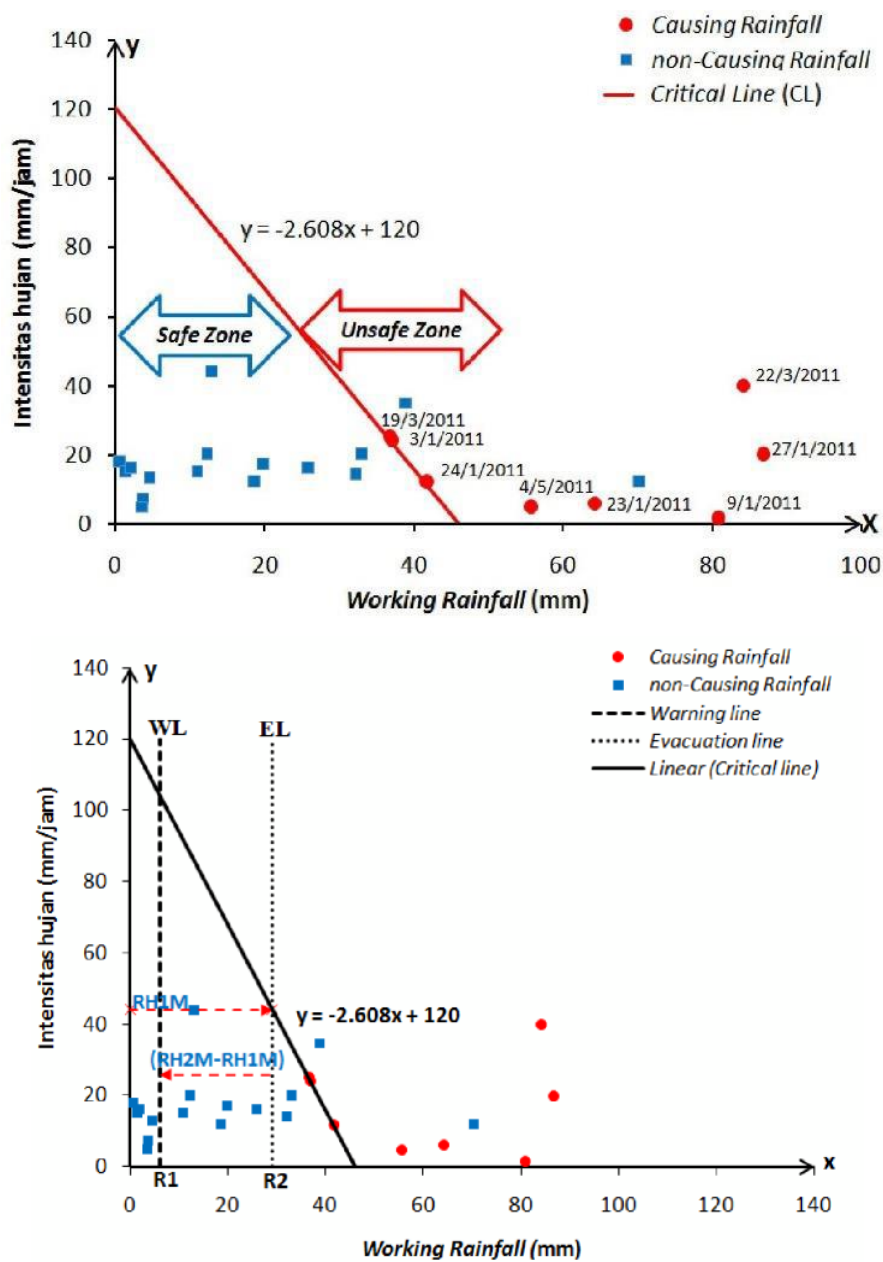**Figure 5.4** and **Figure 5.5** belong to the same catchment, which is Gendol catchment. The critical rainfall analysis by Fitriyadi (2013) used six lahar events at Mt. Merapi from rainfall data in the rainy season of 2006-2007 and 2010-2011. It applied 7 days working rainfall compared with their effective rainfall intensity. Fitriyadi (2013) followed the assumption given by MLIT where the sediment disaster especially debris flow happened after the depth of rainfall exceeds 80 mm or the rainfall intensity is higher than 20 mm/hr. However, no clear pattern showing the significance of those rainfall values to the higher possibility of lahar occurrence, as many lahars occur even under rainfall depth less than 80 mm.

Fibriyantoro (2015), then argued that the rainfall threshold of 80 mm cannot be used to determine the occurrence of lahar at Mt. Merapi, due to the geographical and climatic condition in Indonesia, which is different with Japan. The critical rainfall analysis in Gendol River done by Fibriyantoro (2015) found that the critical line of lahar in Gendol catchment is following the linear equation given by Equation (5.1).

$$Rainfall\ depth\ [\text{mm}] = -2.608R + 120 \qquad (5.1)$$

where, $R$ represents the short-term values of rainfall, which is the rainfall intensity.

It is clear that by following equation (5.1) the rainfall depth values is lower than the rainfall values proposed by MLIT and Fitriyadi (2013). This finding is supported by other studies that mentioned that lahars behaviour at Mt. Merapi changed after the 2010 eruption where it could be easily triggered even by rainfall intensity less than 20 mm/h (Legowo et al., 2012). These behavioral changes happened due to the change of river morphology caused by volcanic materials deposit.

5.2.2 The procedure of critical line.

The procedure of critical line analysis of lahar adopts the critical line analysis procedure for debris flow by MLIT (2004). The procedure is summarized as follows.

1) Analysis of a series of rain.

   Rain series is a continuous rainfall that is isolated by the absence of rain for 24-hours or more, both before and after occurrence (**Figure 5.6**). The total amount of rainfall during that period is defined as Continuous Rainfall (RC). The Antecedent Rainfall (RA) is one-week rainfall before the start of the series. The 24-hour rainfall is calculated from the start of the series of rain determined as antecedent rainfall in one day before ($d_1$), the rainfall occurred within 24 to 48 hours prior to the series of rainfall is defined as antecedent rainfall

two days previous ($d_2$), and so on to seven earlier days ($d_7$). Working rainfall is the cumulative rainfall influenced by the antecedent rainfall calculation. Antecedent working rainfall (*RWA*) is the sum of all antecedent rainfall.
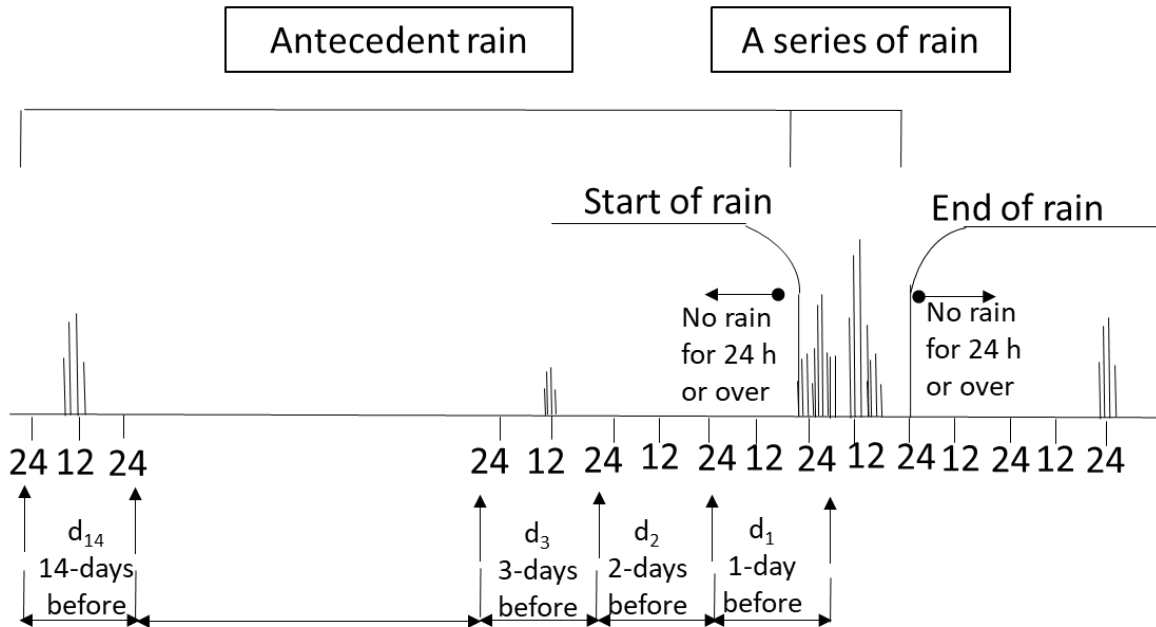


**Figure 5.6** Rain series and antecedent rainfall concept (Ministry of Land, Infrastructure, and Transport (MLIT), 2004).

2) The calculation of antecedent working rainfall (*RWA*) and working rainfall (*RW*).

RWA is obtained by summing up the multiplication between deduction coefficient $\alpha_2$ with $d_2$ and so forth until $\alpha_7$. *RW* is obtained by calculating the cumulative rainfall and *RWA*. Equations (5.2) present the RWA and RW calculation.

$$RWA = \alpha_1 d_1 + \alpha_2 d_2 + \cdots + \alpha_{14} d_{14} = \sum_{t=1}^{14} \alpha_t d_t$$

$$\alpha_i = 0.5^{t/T}$$

$$RW = cumulative\ rainfall + RWA$$

(5.2)

where $\alpha_t$ is deduction coefficient "$t$" days before, $d_t$ is antecedent rainfall "$t$" days before (mm), "$t$" is time before the rainfall (day), $T$ is half-time (day) = 1 day.

3) Calculation of rainfall intensity.

Rainfall intensity causing lahar is analyzed using 1-hour rainfall intensity prior to lahar occurrence, whereas non-causing rainfall was calculated using maximum hourly rainfall intensity in a series of rain, which did not cause a lahar flow.

4) Plotting graph of working rainfall vs. rainfall intensity

The causing rainfall data used "working rainfall up to 1-hour before the flood" as the x-axis and "1-hour rainfall intensity immediately before the flood" as the y-axis. The non-causing rainfall data used "the working rainfall before the start of maximum hourly rainfall" as the x-axis, while the maximum hourly rainfall intensity in a series of the rain as the y-axis.

5) Calculation if RH1M and RH2M

The past maximum 1-hour rainfall is shown by RH1M and the past maximum 2-hour rainfall is shown by RH2M.

6) Generating critical line (CL), warning line (WL) and the evacuation line.

Critical line is drawn by separate in collection points of causing rainfall and non-causing rainfall in the graph of working rainfall vs. rainfall intensity by a straight line. EL is set from RH1M by drawing a horizontal line intersection with CL. EL is perpendicular to a vertical line from that intersection point. While WL is a straight line obtained by paralleling displacement of the EL towards the left side by "RH2M-RH1M".

7) Generating standard rainfall for warning $(R_1)$ and standard rainfall for evacuation $(R_2)$.

$R_1$ is the value of working rainfall at the intersection of the WL on the x-axis, while R2 is the value of working rainfall at the intersection EL on the x-axis.

5.2.3 Another critical line method for lahar assessment at Mt. Merapi

Previously, critical rainfall analysis is also done by analyzing the relationship between rainfall intensity and rainfall duration (Levigne et al., 2000). At Mt. Merapi, analysis of the cumulative rainfall at Plawangan station showed that about 75% of lahars in the Boyong valley reached Kaliurang during the phase of the strong increase of rainfall (40%) or just after the period of peak intensity (35%). A proportion of 25% of the lahars reached Kaliurang during the 10 min period of the peak rainfall intensity and 80% occurred within 30 min before or after this peak period. Thus, it is assumed that most lahars are generated from pyroclastic source deposits at a short distance (about 1–3 km) upstream from Kaliurang, probably at or below 1500–1700 m elevation. During the 1994–1995 rainy season, only one lahar was generated during or at the end of a long period (more than 150 min) of small-intensity rainfall. Based on **Figure 5.7**, a critical line with both parameters, defined as follows.

$$T_r = 0.143D \tag{5.3}$$

where $T_r$ is the triggering rainfall, and $D$ is the triggering rainfall duration. Thus, the minimum threshold for lahar triggering rainfall is 1 mm for 7 min or 9 mm/h.
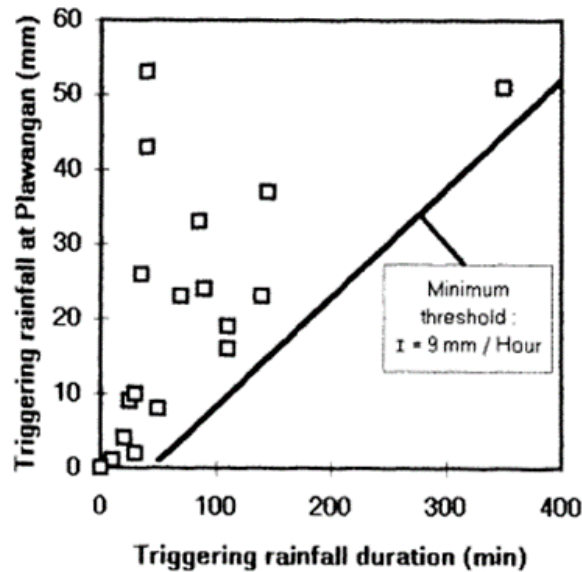
**Figure 5.7** Critical rainfall for triggering lahar in Boyong (1994-1995), based on Lavigne et al. (2000)


## 5.3 Ensemble Rainfall Prediction

Lahar occurrence as a response to severe rainfall intensity is very uncertain. This uncertainty causes by difficulties in rainfall prediction. Precipitation is one of the most uncertain weather parameters, which caused the prediction to be challenging and difficult. In short-term rainfall prediction, the problem is mainly caused by small errors in the initial conditions of a forecast that lead to a loose of skill in the forecast after a finite forecast length (Hapsari, 2011).

Ensemble prediction offers more possibilities of the rainfall pattern evolution, and have been applied for many quantitative precipitation forecasts (QPF). This technique can develop a reliable probabilistic forecasting where the output contains some predictive uncertainties (Fujita et al., 2008; Kim et al., 2009; Hapsari, 2011).

Hapsari (2011) developed an ensemble short-term rainfall prediction by perturbation of initial conditions (IC). In the ensemble forecasting, several forecasts were run by slightly perturbing the control IC, created according to their errors. Thus, the initial state of one of the ensemble members might correspond to the truth of the growth of tiny error in the IC will inevitably lead to a loss of forecast skill in the future.

An overview of a typical ensemble system is presented in **Figure 5.8**. Because rainfall prediction is nonlinear, the error of the ensemble member initially further away from the truth

may tend to grow more slowly than the error of the member initially closer to the truth (shown by the white circle and a black circle respectively).

The ensemble model by Hapsari (2011) was developed by applying the singular vector (SV) and the time-lagged ensemble forecast. The SV is used in meteorology to compute the largest error growth rates for a specified norm. This technique searches the perturbation that, when added to a given basic state will achieve maximum linear perturbation growth. The ensemble lagged forecast is a technique that used various sets of time-lagged starting at different initial times and being verified at the same time. These two techniques combination is an efficient and simplification techniques for the ensemble model.
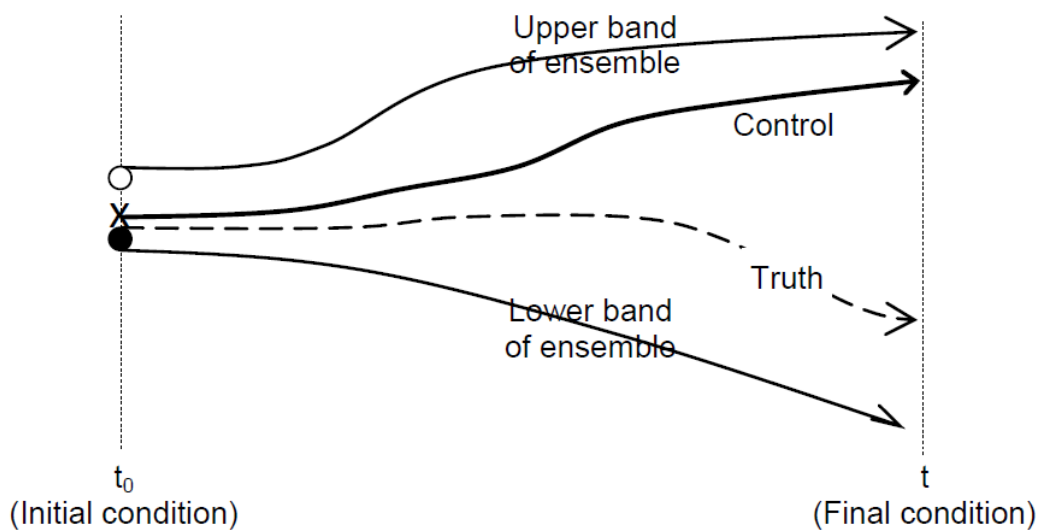


**Figure 5.8** Schematic of the components of a typical ensemble (Hapsari, 2011)

## 5.4 Data and Methodology

Rainfall intensity information is estimated from X-MP radar data at Mt. Merapi. The rainfall data used are from 13-17 February 2016. A real lahar event was reported happened and swept 2 vehicles in the upstream of Gendol catchment on 17 February 2016. The X-MP radar recorded the maximum rainfall intensity higher than 90 mm/h.

Average 1-hour and 2-hour rainfall intensity are given in **Figure 5.9**. The rainfall was concentrated in the summit of Mt. Merapi rather than in the lower elevation, and the average rainfall intensity for 1 hour was 36.58 mm/h. The accumulated rainfall depth in upstream Gendol catchment for 2-hour was 42 mm.

(a) 1 hour mean rainfall intensity  (b) 2 hours mean rainfall intensity

**Figure 5.9** Average rainfall intensity, $r$ [mm/h] for 1 hour (a) and 2 hours (b) monitored by X-MP radar

5.4.1 The short-term rainfall forecast

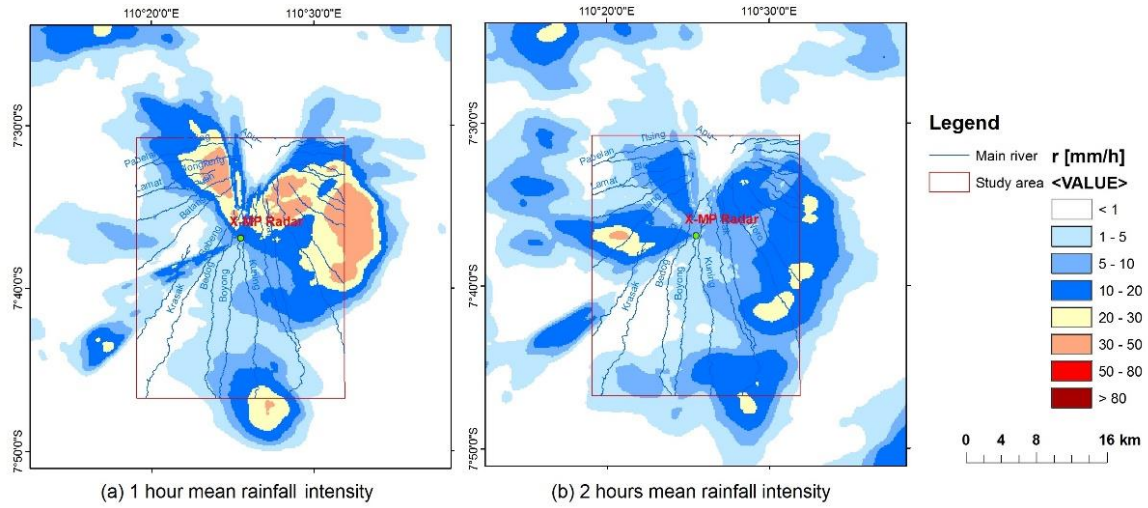The short-term rainfall forecast was based on the translation model developed by Shiiba et al., (1984). The dynamic of the horizontal rainfall intensity distribution $R(x,y,t)$ with the spatial coordinate $(x,y)$ at time $t$ is describe in Equations (5.4) and (5.5).

$$\frac{\partial R}{\partial t} + m\frac{\partial R}{\partial x} + n\frac{\partial R}{\partial y} = w \tag{5.4}$$

where,

$$m = \frac{dx}{dt}, n = \frac{dy}{dt}, w = \frac{dz}{dt} \tag{5.5}$$

where, $m$ and $n$ are advection vector (AV) by which the horizontal rainfall distribution is assumed to be translated, and $w$ is the growth/decay rate of rainfall intensity along its movement. The method assumed that $m$, $n$, and $w$ formations are specified on each grid linearly in the manner of

$$m(x,y) = c_1 x + c_2 y + c_3 \tag{5.6a}$$
$$n(x,y) = c_4 x + c_5 y + c_6 \tag{5.6b}$$
$$w(x,y) = c_7 x + c_8 y + c_9 \tag{5.6c}$$

The $c_1$ to $c_9$ parameters are optimized by linear least square using past observed X-MP radar data approximated by central difference scheme according to a method explained by Hapsari (2011).

Extrapolated pattern of rainfall for a time step, $\sigma$ into the future $(t_0+t)$, is given by equations (5.7) and (5.8)

$$r(x, y, t_0 + t) = r(x(t_0), y(t_0), t_0) - X(\sigma; c_1, \dots, c_9) \begin{bmatrix} x \\ y \\ 1 \end{bmatrix} \tag{5.7}$$

$$\begin{bmatrix} x(t_0) \\ y(t_0) \end{bmatrix} = Y(-\sigma; c_1, \dots, c_6) \begin{bmatrix} x \\ y \\ 1 \end{bmatrix} \tag{5.8}$$

where *X* and *Y* are 3×3 and 2×3 matrices respectively.

This translation vector is able to identify the horizontal movement of rainfall intensity distribution. **Table 5.1** gives the examples of sets of parameters that can be used to different model phenomena.

The rainfall prediction results would be verified quantitatively by using the Pearson correlation method. Three past rainfall observation sheets were used, and the initial prediction time was 15:50 local time (UTC+7). The calculation domain was within radar observation and the mesh size was resampled to be 1 km. We applied an ensemble lagged forecast from 2 minutes to 6 minutes and assumed the phenomena is parallel, translation, and rotation. The singular vector (SV) method to create the initial condition perturbations was also used to increase the accuracy of the forecasting (Hapsari, 2011; Palmer & Zanna, 2013).

**Table 5.1** Combination of advection vectors parameter for different rainfall phenomena

| Phenomena | $c_1$ | $c_2$ | $c_3$ | $c_4$ | $c_5$ | $c_6$ | $c_7$ | $c_8$ | $c_9$ |
|---|---|---|---|---|---|---|---|---|---|
| Parallel and translation only | | | √ | | | √ | | | |
| Translation and rotation only | √ | √ | √ | √ | √ | √ | | | |
| Parallel, translation, growth decay | | | √ | | | √ | √ | √ | √ |
| Translation, rotation, growth-decay | √ | √ | √ | √ | √ | √ | √ | √ | √ |

The perturbation of *m* and *n* from equations (5.3) and (5.4) is analyzed by SV method following Jacobian Matrix, *J*:

$$J = \begin{pmatrix} \partial m / \partial x & \partial m / \partial y \\ \partial n / \partial x & \partial n / \partial y \end{pmatrix} \tag{5.9}$$

The optimization time is done over $t_0 = 0$ hour to $t = 3$ hours as previous studies said that this duration gave better prediction. The error matrix of Jacobian matrix is given by

$$L = (3hr, 0\ hr) = \Pi \begin{pmatrix} e^{3\lambda_2} & 0 \\ 0 & e^{3\lambda_2} \end{pmatrix} \tag{5.10}$$

In the translation model, the analysis scheme could be referred to the process of finding the proper $c_1$-$c_9$ from past observed radar rainfall data standing for the AV of the system. The error of AV is found by using several past observed radar-rainfall sheets, which are used for determining $c_1$ to $c_9$ for future prediction (equations (3.5) – (3.8)). In this method, if the AV as the initial condition (IC) is perfectly correct, the computed rainfall movement would thus provide an exact forecast compared with the available observation. However, the deviation based on rainfall echo position is always happened, hence the average of this deviation over the grid-point space is regarded as $e_\delta$. The $\delta$ in the initial time is regarded as the scaled $v_i$ according to the $e_\delta$, both in $x$ and $y$-direction.

The forecasting scheme in the translation model is performed by tracking the backward along the characteristic curves of the simultaneous differential equation (in this case, a linear model):

$$\frac{dx(t)}{dt} = c_1 x(t) + c_2 y(t) + c_3 \tag{5.11}$$

$$\frac{dy(t)}{dt} = c_4 x(t) + c_5 y(t) + c_6 \tag{5.12}$$

The SV method is applied into the 2-dimensional forecasting model. This 2-dimensional SV represents the 2-variables at the translation model, i.e. $x$ and $y$. Initial ensemble states are created by adding and subtracting the $\delta$ to the control/unperturbed IC in the forecasting scheme. Hence, the equations (5.10) and (5.11) would be changed due to $\delta$ in orthogonal $x$ and $y$-dimension:

$$\frac{d(x \pm \delta_x)}{dt} = c_1(x \pm \delta_x) + c_2(y \pm \delta_y) + c_3 \tag{5.13}$$

$$\frac{d(y \pm \delta_y)}{dt} = c_4(x \pm \delta_x) + c_5(y \pm \delta_y) + c_6 \tag{5.14}$$

Where, $\delta_x$ and $\delta_y$ is the scaled SV in $x$ and $y$-dimension.

### 5.4.2 The snake line analysis

Snake line is a line showing the changes of cumulative rainfall and rainfall intensity as shown in **Figure 5.1**. In this study, the snake line analysis is done by plotting the relationship of effective antecedent rainfall depth (mm) in the $x$-axis, and the rainfall intensity in the $y$-axis.

The MLIT procedure (2004) has suggested the use of 14 days prior to landslide or debris flow occurrence to consider the contribution of antecedent rainfall in the occurrence of debris flow. However, more studies found that the definition of the period over which to accumulate

precipitation is the key difficulty in this kind of studies. Review of the literature reveals a significant scatter in the considered periods. Kim et al. (1991) considered 3 days, Heyerdahl et al. (2003) considered 4 days, Crozier (1999) and Glade et al. (2000) considered 10 days and Aleotti (2004) selected 7, 10 and 15-days. Terlien (1998) tested 2-, 5-, 15- and 25-days periods and found best results for the longest rainfall periods. Pasuto and Silvano (1989) tested rainfall periods from 1 to 120-days and found the best correlation with landslide occurrence is given by the 15-day antecedent rainfall. Hasnawir and Kubota (2008) found that debris flow at Mt. Bawakaraeng Caldera, South Sulawesi of Indonesia is triggered by short duration precipitation events (1-3 days).

This large variability can be attributed to different factors: (i) diverse lithological, morphological, vegetation, and soil conditions; (ii) different climatic regimes and meteorological circumstances leading to slope instability; (iii) a heterogeneity and incompleteness in the rainfall and landslide data used to determine the thresholds.

On the other hand, another study argues the importance of antecedent rainfall for debris flow occurrence, especially when dealing with the very high rainfall intensity in tropical areas. Corominas and Moya (1999), working in the Pyrenees, observed that slopes covered by coarse debris exhibiting large interparticle voids were likely to generate debris flows without any significant antecedent precipitation.

Based on the results by previous studies, the rainfall accumulation used for the snake line analysis in this study obtained by using 4-days effective antecedent rainfall data estimated from X-MP radar for each 10-minutes interval. The plotting was done by applied the predicted values from ensemble short-term rainfall prediction. The prediction would be done if the values showed increasing rainfall tendency at the $R_2$ (EL), as suggested by MLIT procedure (MLIT 2004). However, another study does not recommend the used of CL and EL for lahar potency analysis by snake line (Yulinsa, 2015). In her research, she found that the score of WL and EL is not significant, due to the intermittent rain condition at Mt. Merapi. On the other hand, lahar sometimes occurs as a result of rainfall accumulation instead of rainfall intensity. Thus, in this study, the short-term rainfall forecast would be done if the snake line trend was going to approach the critical line.

5.4.3 Critical rainfall based on the statistical approach

For the comparison, another statistical method for the critical rainfall analysis is done by dummy regression. This method used some lahar events happened after the 2010 eruption.

The dummy regression is a regression analysis done by involving a dummy variable, which is also known as an indicator variable, design variable, Boolean indicator, binary variable, or qualitative variable. Dummy variable takes the value 0 or 1 to indicate the absence or presence of some categorical effects that may be expected to shift the outcome.

In dummy regression, the dependent variables it not only influenced quantitatively by the independent variables, but also qualitatively. A dummy independent variable, which for some observations is given the value of 0 and cause the variable's coefficient to have no role in influencing the dependent variable. When the dummy is given the value of 1, its coefficient acts to alter the intercept.

A simple model with one continuous variable $(x)$ and one dummy $(d)$ takes the form of:
$$y = \beta_0 + \delta_0 d + \beta_1 x + \varepsilon \tag{5.15a}$$
This can be interpreted as an intercept shift as follows.

$$\text{If d} = 0, \text{ then } y = \beta_0 + \beta_1 x + \varepsilon \tag{5.15b}$$
$$\text{If d} = 1, \text{ then } y = (\beta_0 + \delta_0) + \beta_1 x + \varepsilon \tag{5.15c}$$

where $y$ is the dependent variable, $x$ is the independent variable, $(\beta_0 + \delta_0)$ acts as an intercept, $\beta_1$ is the constant of independent variables, and $\varepsilon$ is the residue of regression.

Rainfall data used are from seven rain gauge stations: Pabelan, Ngepos, Pos Kaliurang, Ngandong, Sorasan, Sukorini, and Kaliadem. The causing rainfall lahar is when lahar happened nearby the stations and when lahars were not reported in nearby rivers from the stations; those rainfalls are classified as non-causing rainfall. Both the causing-and non-causing rainfall were collected from the same stations and from the same days of lahar events.

The rainfall intensity acted as the dependent variable (output), while the duration is the independent variable. The rainfall duration is the dummy variable, where qualitatively were classified into three classes based on Wang and Shao (2000). Those classes are warning, disastrous, and critical.

**Table 5.2** summarizes the critical rainfall threshold analysis and **Figure 5.10** gives the classification of rainfall based on the Dummy regression. According to **Figure 5.10**, if the precipitation values (RD) were below the warning line, the risk for the lahar occurrence would be small and no measure needs to be taken. If the observed/predicted values fell between the warning and the disastrous rainfall lines, the lahar potency would be higher, then the preventive measures should be considered. The critical rainfall classifies the precipitation values that exceed the disastrous rainfall line. If the rainfall were classified as critical rainfall, then the lahar is about to occur. In this situation, people must be evacuated from the hazard-prone area.

Although this statistical method is applicable for determining the critical rainfall of debris, there are still some uncertainties. The first is because of the quality of the rain gauge data, as most of the stations are located in the downstream. The second is the decreasing source of lahar in the upstream due to the massive mining activity happens at Mt. Merapi (Ikhsan et al., 2010). The previous study also highlights that the statistical method gives lower reliability than physical distributed based method (Wang and Shao, 2000).
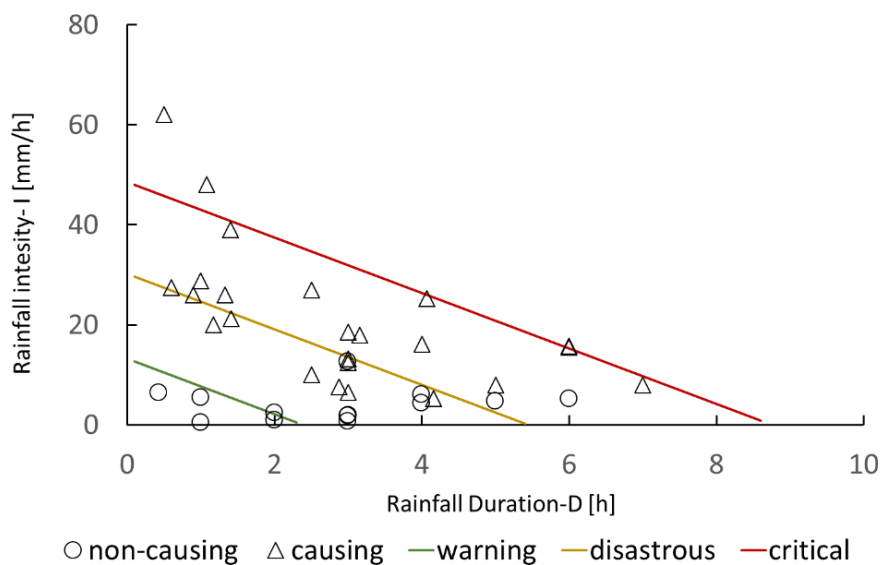


**Figure 5.10** Critical rain analysis based on statistical approach.

**Table 5.2** Equations for critical rainfall of debris flow at Mt. Merapi

| Equation | $R^2$ | Rainfall class | |
|---|---|---|---|
| $I = 13.23-5.55D$ | 0.86 | Warning | (5.16a) |
| $I = 30.21-5.55D$ | 0.86 | Disaster | (5.16b) |
| $I = 48.57-5.55D$ | 0.86 | Critical | (5.17c) |

## 5.5 Results and Discussion

5.5.1 Rainfall prediction

The best-predicted areal rainfall intensity in Gendol catchment is given in **Figure 5.11**, and the spatial correlation between predicted and observed rainfall are given in **Table 5.3**. In general, the short-term rainfall prediction was still unable to predict the spatial movement of rainfall. However, the temporal variation for the areal rainfall showed a similar pattern.

Using the time lag (-4) at 15:46 with second perturbation or SV(+2) gave the closest rainfall pattern with the observed rainfall (**Figures 5.11** and **5.12**). All of the first singular vectors (SV(+1)) gave the tendencies of rainfall to have negative growth, which showed that the second singular vector results were more likely to project the leading eigenvalue in its transient time (Palmer & Zanna, 2013).

**Table 5.3** Spatial correlation between predicted values and observed rainfall

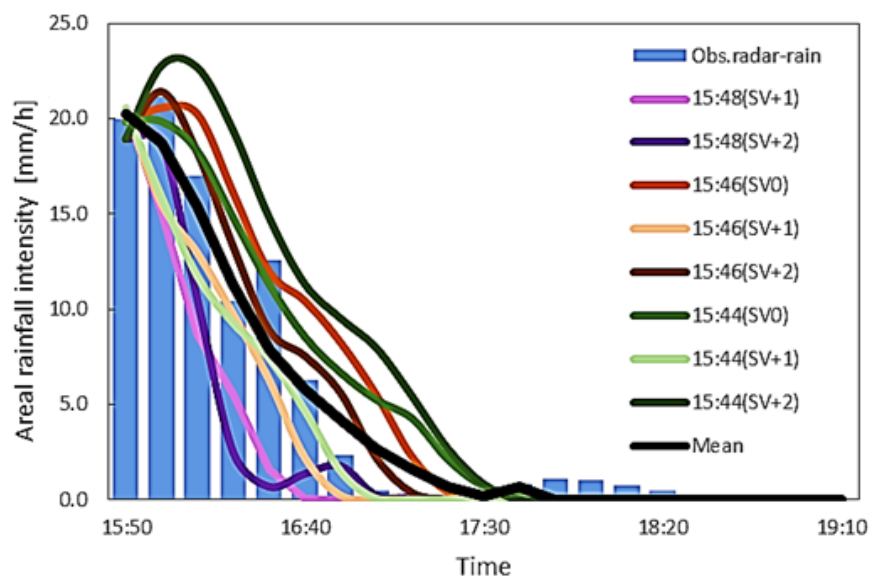| Time | Pearson Correlation | |
|------|-------------|----------------|
|      | **15:46 (SV+2)** | **Mean-ensemble** |
| **16:20** | 0.10 | 0.36 |
| **16:50** | 0.19 | 0.18 |
| **17:20** | 0.01 | 0.04 |
| **17:50** | 0.05 | -0.02 |



**Figure 5.11** The Areal rainfall intensity [mm/h] prediction in Gendol catchment by various methods of singular vector and its mean values compares to the observed rainfall with the real observed rainfall
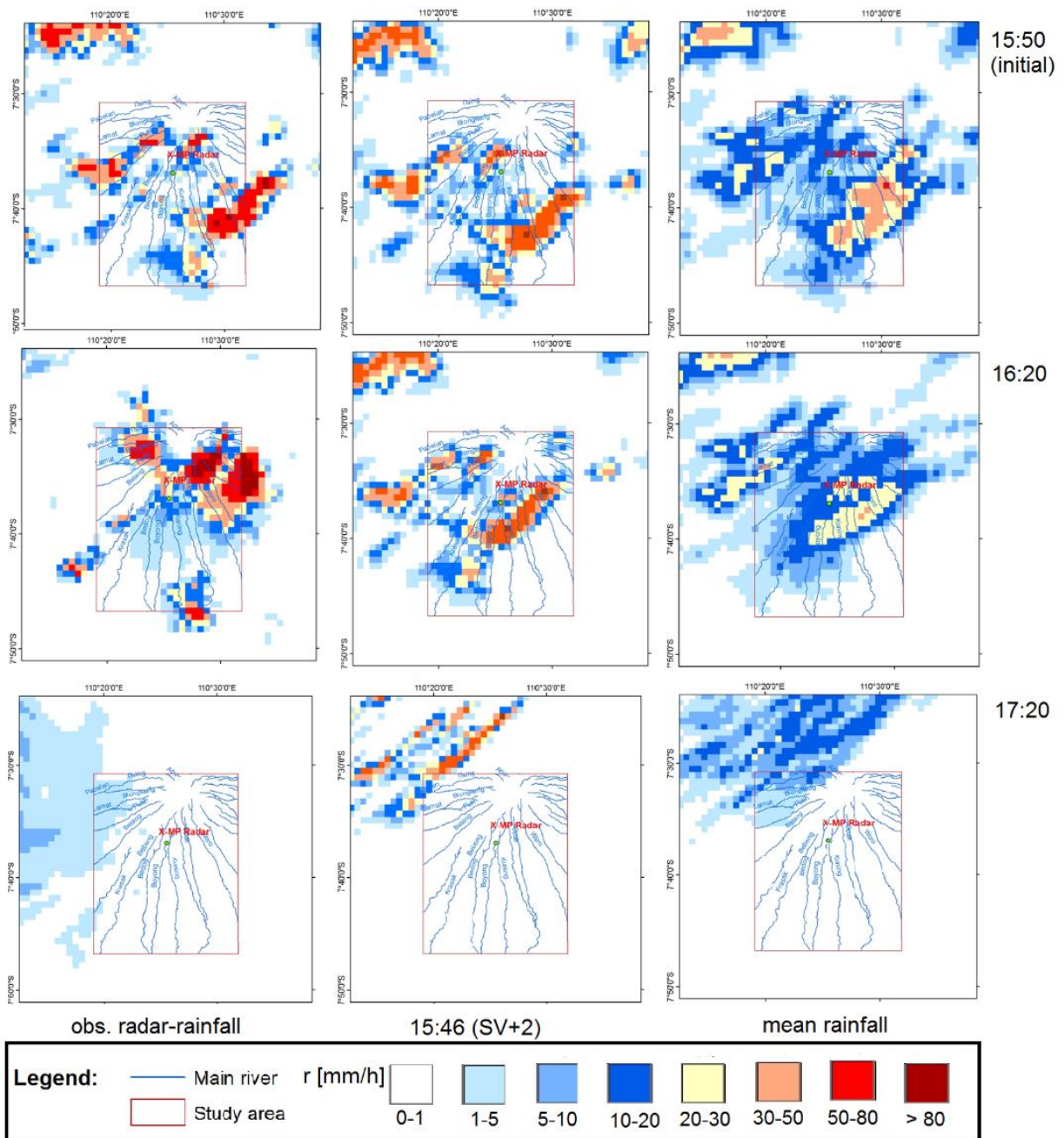
**Figure 5.12** Spatial rainfall intensity, $r$ [mm/h] distribution of predicted rainfall compares

Future error correction is required for getting a proper scale of the SV. The observed rainfall values also showed great decay rate, which could not be predicted by the model. This made the correlation between predicted and observed to be linearly weaker as simulation period went longer. These two factors, which are the growth decay rate and applying the second perturbation of SV, should be the main consideration for further model improvement.

Due to the poor results of the spatial analysis, while the timely area rainfall gives a similar pattern to the actual average rainfall, the further analysis of snake line and lahar potency is

done by assuming the rainfall in Gendol catchment to be represented by the average values of the prediction model, given by the mean ensemble values. The analysis assumed rainfall to be uniform in entire catchment using the mean ensemble of rainfall intensity and rainfall depth. Another reason is the analysis relied on a critical line given by Batur station, which also assumed the uniformity of rainfall (Fibriyantoro, 2015).

5.5.2 Snake line analysis based on predicted values

The critical rainfall analysis followed previous studies by Fibriyantoro (2015) and is statistically based according to equation (5.14). The snake line assessment based on previous studies showed that the predicted values could show the potency of rainfall to trigger the lahar occurrence in Gendol River (**Figures 5.13** and **5.14**).

Based on the snake line given by **Figure 5.14**, the lahar occurrence would happen due to the rainfall event on 17 February 2016, after 15:40 local time. Using one day prior rainfall series and four days rainfall series resulted in the relatively same snake line plotting. The plotting of snake line by mean ensemble prediction was also able to show the potency of lahar similar to the real data. This result indicates that the antecedent rainfall effects on Mt. Merapi does not require long-term rainfall data for the analysis.

The prediction was started when the rainfall accumulation is closed to the CL. It was because of the rainfall intensity at EL shows decreasing trend, which again confirmed the insignificance of EL and WL. The insignificant of EL and WL on lahar estimation could be the result of the lack of data used by previous studies, as it only based on three lahar events. The analysis was based on assuming the rainfall to be uniform, hence the accumulation of rainfall plays more important role (Yulinsa, 2015). Another aspect that the 1-hour rainfall and 2-hour rainfall might be not a good indicator as the lahar at Mt. Merapi can happen within less than 1-hour after the event rain starts. In the future, it is recommended to analyze the critical rainfall on a smaller scale by using X-MP radar data. However, as the lahar events have been significantly decreased, the main problem is insufficient data.
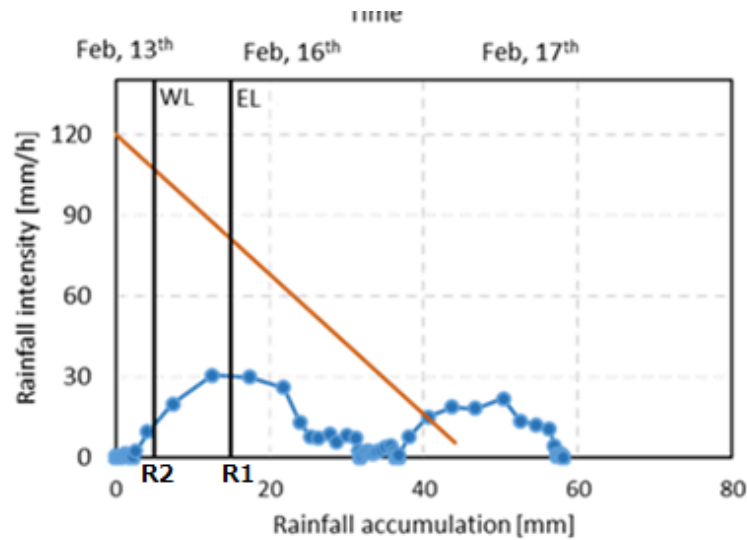
**Figure 5.13** Snake line assessment based on previous critical line (orange line) analysis by Fibriyantoro (2015) using 4-days rainfall data prior to lahar occurrence. The Rainfall data are based on actual rainfall accumulation and rainfall intensity.
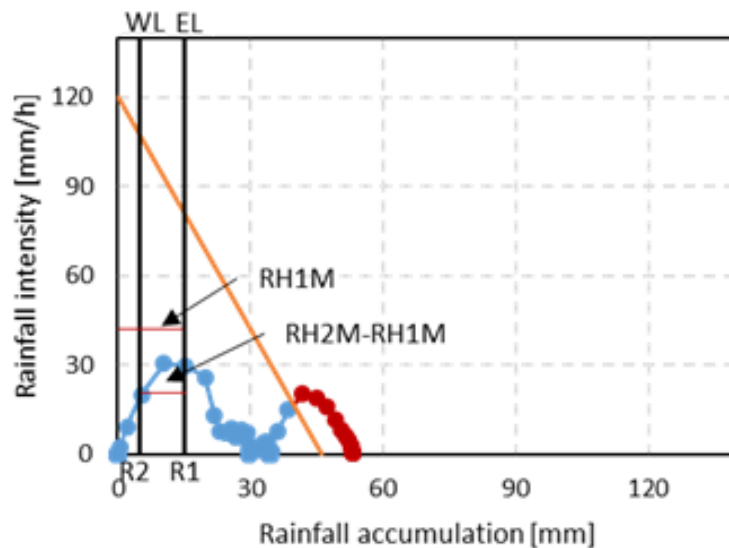


**Figure 5.14** Snake line assessment based on previous critical line (orange line) analysis by Fibriyantoro (2015) using 1-day rainfall data prior to lahar occurrence. The red line and markers show the predicted values of rainfall based on short-term rainfall prediction. Rainfall intensity for predicted values is given by mean values ensemble prediction

The rainfall forecasting and real X-MP radar showed that rainfall was started at 15:30 and stopped at 17:30 local time, which meant the duration of rainfall was 2-hours. Applying the duration into equations (5.17) gave a result of the rainfall intensity was 19.21 mm/h and 37.75 mm/h respectively for disastrous line and critical line (**Figure 5.10**). The values indicate that rainfall has the potency to trigger lahar in Gendol catchment. As both statistical methods and

the MLIT method were in agreement that lahar was about to occur based on the predicted rainfall values, the short-term rainfall prediction proved to be a valuable method for early lahar analysis at Mt. Merapi.

## 5.6 Summary

Short-term rainfall prediction had been done at Mt. Merapi based on advection model. The predicted values still had a poor spatial correlation, however; the timely average rainfall intensity could follow the pattern of real observed data. This prediction could be applied to show the potency of rain-triggered lahar by the application to the snake line analysis. The antecedent rainfall series for snake line purpose should be obtained by at least 24-hours rainfall prior to the lahar occurrence.

# CHAPTER VI

# EMPIRICAL METHOD FOR REAL-TIME LAHAR MONITORING AT Mt. MERAPI

## 6.1 Introduction

Lahar is a wet mass of volcanic fragments flowing rapidly downhill, which covers three kinds of flow: debris flow, hyper-concentrated flow, and mudflow (Lavigne et al, 2000). Most studies classifies lahar flow as debris flow happens in volcanic regions (Takahashi, 2014). Therefore, the hydraulic models of debris flows are usually applicable for lahar simulation.

A single-phase continuum model by assuming the mixture of solid particles and fluid as a kind of continues fluid is adopted by many studies to simplify the complexity of physical mechanism of debris flow. Most of those models are based on three consecutive equations: Bingham fluid, Newtonian fluid, and dilatant fluid model (Takahashi, 2014).

The Bingham fluid model assumes debris flow is triggered if the operating shear stress is higher than its yield stress. Once it exceeds the yield stress, the fluid will behave as a Newtonian fluid. Bingham rheology for the application of debris flow simulation is limited to mud-rich debris flows (Takahashi, 2014; de Blazio 2016; Whipple, 2014).

Even so, debris flow is a non-Newtonian fluid, but some studies have succeeded to apply Newtonian rheology to debris flows studies (Takahashi, 2014; Arattano and Savage, 1994). The previous study used Newtonian fluid approach by the application of Manning formula to a kinematic wave model for debris flow simulation. Although it succeeded in simulating the stage hydrographs from two debris flows happened at Mt. St. Helens in October 1981, but it could not predict the travel distance of debris flow (Arattano and Savage, 1994).

The dilatant fluid model considers the quadratic acceleration of debris flow is equal to its shear stress and depends on equilibrium concentration. The application of the dilatant fluid model is adopted by HyperKANAKO model, a graphical user interface of debris flow. The model could simulate dynamic debris flow, immature debris flows, and turbulent bed load. HyperKANAKO could simulate lahar events in Gendol catchment at Mt. Merapi, but increasing flow velocity in the down-stream area was resulted from the simulation. This

problem caused by the small Manning roughness coefficient used as the model's parameter (**Chapter IV**).

Even so, the Manning formula is applicable to debris flow models, but values between 0.05-0.1 are recommended for Manning roughness coefficient, and the uncertainties regarding the proper values are still remaining (de Haas et al., 2016). After 1994 eruption, Boyong River in Mt. Merapi had Manning coefficients ranged from 0.194 to 0.641(Lavigne et al., 2003).

The lahar simulation at Mt. Merapi has been done previously by applying HyperKANAKO model. However, the study used rain gauge data, which has poor spatial information, and further development applied a semi-distributed model of rainfall as the triggering force for the boundary condition (Syarifuddin et al, 2015; Syarifuddin et al., 2017). Recent studies have underlined the importance of weather radar for debris flow studies due to the small scale of debris flow events occurrences (Marra et al., 2014) and applying distributed model of rainfall-lahar models have not been developed previously.

In this chapter, a proposed model for lahar is presented by a modification of a shallow water open channel model. The modification is done to Rainfall-runoff and Inundation (RRI) model so that it is able to calculate lahar properties such as the flow velocity, travel distance, and total volume of the sediment. Because rainfall distribution is an important input for RRI model, better rainfall input is provided by X-MP radar and integrated to improve the model performance.

## 6.2 Rainfall-Runoff Inundation Model

The RRI model is a two-dimensional model for the simultaneously rainfall-runoff and flood inundation simulation (Sayama et al., 2015). The 2D diffusive wave model calculates the flow on the slope grid cells, and the channel flow is calculated with the 1D diffusive wave model. The RRI model also simulates lateral sub-surface flow, vertical infiltration flow, and surface flow. The flow interaction between the river channel and slope is estimated based on the different overflowing formulae, depending on water level and levee height conditions

Previous RRI applications are for large-scale and relatively flat basins (Sayama et al., 2015; Bhagabati and Kawasaki, 2017). The application is more suitable for short-term events, although some studies also succeeded in the long-term simulation. However, the application of RRI model in the mountainous area is relatively unexplored.

In the mountainous area, a kinematic wave model is considered to be more suitable than a diffusive model. In debris flow case, the flow is not only influenced by the intercollision particles but also due to the gravitational force (Iverson, 1997).

## 6.3 Empirical Method for Lahar Estimation

Models for debris flow initiation in channels have been studied by dynamic and empirical approaches. (Takahashi, 1978; Rice et al., 1998; Gregoretti, 2000; Tognacca et al., 2000; Gregoretti and Fontana, 2008). These methods are chosen due to the impracticability of conducting in-situ observations and experiments for debris-flow occurrences. The key factors determine the debris flow generation are the availability of loose materials, slope gradients, median particle diameter ($D_{50}$), and flood discharges (Takahashi, 1978; Cui, 1992; Martin and Moody, 2001).

In **Chapter IV**, the application of HyperKANAKO model gave increasing flow velocity on the flatter area, due to the turbulent Newtonian rheology was used at slope lower than 3°. The simulation used small Manning roughness coefficient at 0.03, which is the value of the Manning roughness coefficient of the natural stream (Chow, 1959).

Rickenman (2013) compared the flow-resistant coefficient and its relationship to the peak discharge between debris flow and clear water flow. The relationship is used to formulate new Manning roughness coefficient for turbulent flow as given in Equation (6.1).

$$n_* = 0.077 q_*{}^{1/15} \tag{6.1}$$

$q*$ is dimensionless discharge calculated by a method proposed by Takahashi (1999) as follows.

$$q* = (Q/D)g^{0.5}D_m{}^{1.5} \tag{6.2}$$

Where $Q$ (m³s⁻¹) is the surface water discharge, $g$ (ms⁻²) is the acceleration due to the gravity, $D_m$ (m) is the mean particle size, and $D$ (m) is the width of the channel bed. This equation was later used by Chui et al. (2014) by setting up some experimental test of debris flow initiation under different slope in China. They came to a conclusion that debris flow was easily triggered at steeper slope by small discharge threshold. However, in the flatter area, higher discharge was required to initiate debris flow. They later formulated an empirical equation for dimensionless discharge in flatter area as follows.

$$q_* = \frac{40}{\tan\theta^{0.1}} \tag{6.3}$$

Applying equation (6.3), we can determine the Manning roughness coefficient in turbulent flow as an inverse proportion to the slope, which caused the unit width discharge and the flow velocity to be smaller comparing to the applying a constant Manning roughness coefficient at 0.03.

This method is very useful as the previous studies also arguing about the uncertainty of Manning roughness coefficient and the difficulties in determining the proper values for debris flow studies.

## 6.4 Methodology

The development of lahar estimation by RRI model and X-MP radar coupling is done according to the flowchart in **Figure 6.1**.

6.4.1 Governing equations

The RRI model consists of diffusive-wave approximation and kinematic-wave model. Kinematic-wave model (kine-wave) is one of the approximations of the dynamic-wave model for one-dimensional shallow-water waves (unsteady, gradually varied, open-channel flow). It is a 1D model that consists of the continuity equation and the equation of motion as given in equations (6.4) and (6.5)

$$\frac{\partial h}{\partial t} + \frac{\partial q_x}{\partial x} = R - f \tag{6.4}$$

$$\frac{\partial q_x}{\partial x} + \frac{\partial u q_x}{\partial x} = -gh\frac{\partial H}{\partial x} - \frac{\tau_x}{\rho_w} \tag{6.5}$$

where $h$ is water (flow) depth, $q$ is unit width discharge in the $x$ and $y$-direction, $u$ and $v$ are the flow velocity components perpendicular to the $x$-axis direction, $g$ is the gravitational acceleration, $H$ is elevation, $\rho$ is the water density, $r$ is rainfall rate, $f$ is the infiltration rate and $\tau$ is shearing stress.

In the kinematic-wave approximation, the discharge is the friction of the slope equals to the bed slope, calculated by the Manning equation. However, the model also considers the unsaturated and saturated condition of soil by equation (6.4).

$$q = \begin{cases} -k_a(\dfrac{h}{d_m})^\beta h\tan\theta & (h \leq d_a) \\[2mm] -k_a(h-d_a)^{\frac{5}{3}}\sqrt{\tan\theta} - k_a h\tan\theta & (d_m < h \leq d_a) \\[2mm] -\dfrac{1}{n}(h-d_a)^{\frac{5}{3}}\sqrt{\tan\theta} - k_a(h-d_m)\tan\theta - k_m d_m\tan\theta & (d_a < h) \end{cases} \qquad (6.6)$$

where $k_a$ is the lateral saturated hydraulic conductivity, $k_m$ is conductivity in the unsaturated zone, $d_m$ is total soil depth, $d_a$ is the soil depth times the effective porosity, and $n$ is the Manning roughness coefficient. In term of debris flow calculation and stoppage mechanism, equations (6.1) and (6.3) is applied to update the Manning roughness coefficient, $n$ at equation (6.6) in each river cell.
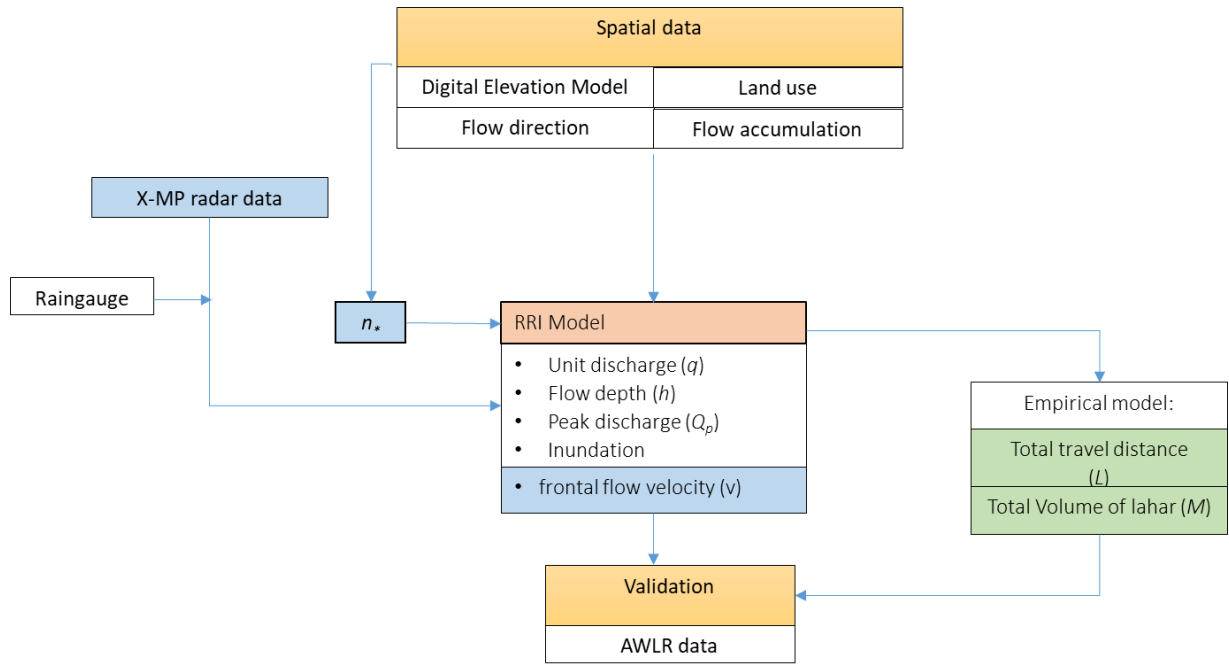


**Figure 6.1** Coupling of X-MP radar and modified RRI for lahar estimation

This modification makes the Manning roughness coefficient in each river cell to have an inverse proportion to the slope, $\theta$.

The infiltration rate is calculated based on Green-Ampt infiltration model:

$$f = k_v\left[1 + \frac{(\emptyset - w_c)S_f}{F}\right] \qquad (6.7)$$

where $k_v$ is the vertical saturated hydraulic conductivity, $\emptyset$ is the soil porosity, $w_c$ is the initial water volume content, $S_f$ is the suction at the vertical wetting front, and $F$ is the cumulative infiltration depth.

The mean frontal velocity, $v$ and total travel distance, $L$ were calculated based on equations from the previous study (Rickenmann, 1999) as follows.

$$v = 2.1q^{0.33}(\tan\theta)^{0.33} \tag{6.8}$$

$$L = 1.9M^{0.16}H^{0.83} \tag{6.9}$$

where the volume of flow, $M$ is defined by an empirical equation at Mt. Merapi area (Jitousono et al., 1995).

$$M = 170Q_p^{1.2} \tag{6.10}$$

the peak discharge, $Q_p$ is calculated by the kinematic wave model.

6.4.2 Model's Limitations and Assumptions.

The model is unable to calculate the process of erosion and sediment happened during the simulation, hence could not give an understanding of lahar behavior and the changing states from debris flow to hyper-concentrated flow. Another forthcoming of this model is the fact that debris flow behaves as a non-Newtonian flow. Hence, this kind of method could only be applied where we assumed lahar takes form as a hyper-concentrated flow at Mt. Merapi due to the decreasing amount of remaining volcanic materials. The lack of volcanic materials and the small particle size of volcanic ash, caused the calculation considering lahar to behave as the turbulent muddy flow. This assumption is supported by Takahashi (2009), which stated that if the ratio of mean particle diameter and water depth is higher than 30 ($D_m < 2$ mm), the debris flow calculation could be approached by turbulent Newtonian method. The model assumed lahar as a hyper-concentrated flow which is initiated in the river stream, which follows the definition of lahar by Lavigne et al. (2003).

Despite those limitations, this model combined the distributed model and empirical method, which is able to perform a fast calculation of discharge and flow velocity. This aspect is useful and important for early warning of disaster assessment, as lahar usually occurred rapidly within 1-hour from the rainfall peak. The model could also estimate the inundation area caused by lahar flow.

# CHAPTER VII

# APPLICATION EXAMPLE FOR
# THE PROPOSED METHOD

## 7.1 Introduction

In order to know if the proposed method can be applied for remote lahar monitoring, the modified model is tested to study lahar occurrence in Gendol catchment that happened on 17 February 2016 (Figure 7.1). The system is also applied in the Putih catchment for calibration, even there is no report of lahar occurrence in this area (BPPTKG, 2016). However, according to de Belizal et al. (2013), Putih River experienced the most lahar occurrences after 2010 eruption, where more than 50 lahar events have happened in this catchment during the rainy season in 2010.

Another aspect that would be applied is the short-term rainfall prediction. This aspect is important because the simulation of the distributed hydrological model requires a lot of time. Hence, by getting earlier rainfall information from the rainfall prediction model, the monitoring of lahar could be specified in the area where the lahar events have the higher potency to happen. This step will require the critical threshold of rainfall that is obtained from the literature review.



**Figure 7.1** Lahar event happened in Gendol River on 17 February 2016 (pikiranrakyat.com)

## 7.2 Study Area

### 7.2.1 Gendol Catchment

Gendol catchment is located on the southeastern flank of Mt. Merapi (**Figure 7.2**). The catchment area is 67 km$^2$, with 21.7 km river length. During the 2010 eruption, the catchment received most of the pyroclastic materials. Although the source of this material has decreased significantly, some of them remain at the elevation higher than 1200 m amsl. At this elevation, lahar initiations were mostly reported.

The catchment's rainfall is represented by Sorasan station which is located in the downstream area (300 m amsl), hence it could not monitor rainfall condition at the higher risks area in the upstream.
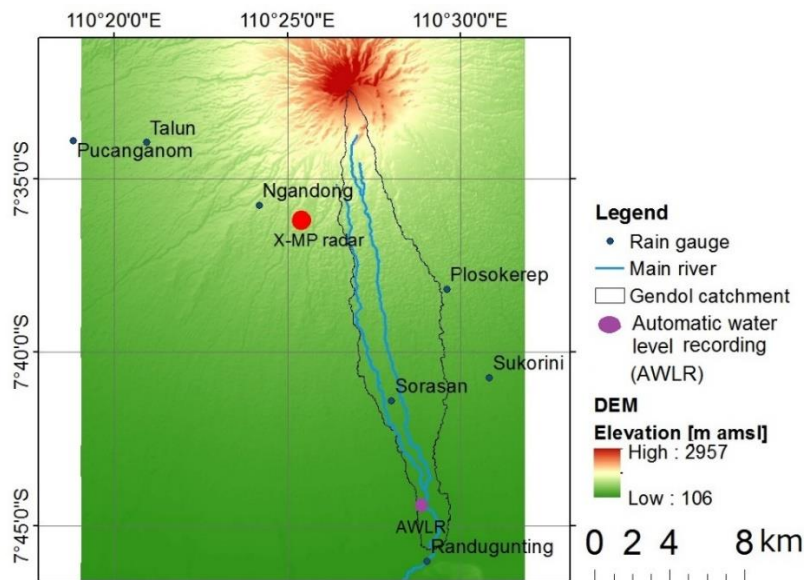


**Figure 7.2** Gendol catchment and the location of ARR station manage by Sabo dam Agency and the position of X-MP radar

### 7.2.2 Putih catchment

The calibration of the model is done in Putih catchment (**Figure 7.3**). Putih catchment has 144.50 km$^2$ area with an average slope of 4.30°. At elevation higher than 400 m amsl, Putih catchment, has an average slope of 8.08°, which makes it steeper comparing to the Gendol catchment which has 6.8° at elevation higher than 900 m amsl (see **Chapter III** and **IV**).

The main river is 28 km length and flowing along the south-western slope of Mt. Merapi. The catchment has long been known as one of the most volcanic deposited areas due to the periodic

eruptions happen at Mt. Merapi. In the upper reaches of the Putih River, the total depth of volcanic ash deposition during the 2010 eruption was estimated to be more than 10 cm. Putih River was the most frequently affected by lahars with 55 events reported from October 2010 to October 2011 at a recurrence of approximately two lahars per week during the period (de Belizal et al., 2013).
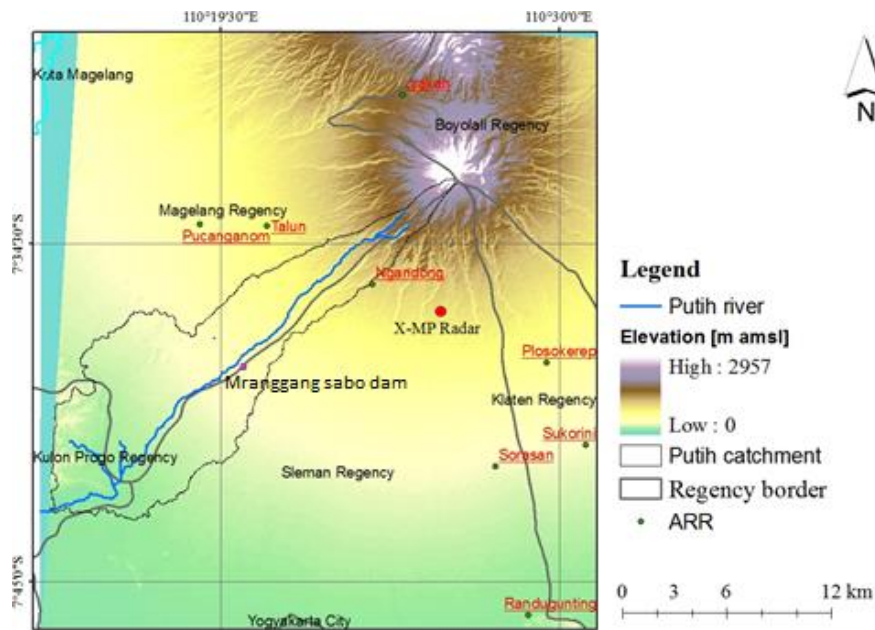


**Figure 7.3** Putih catchment and the location of ARR station manage by Sabo dam Agency (ARR Sabo) and the position of X-MP radar

Putih and Gendol lahar corridors are the main deposit areas with respective volumes estimated at $4.9 \times 10^6 \, m^3$ and $3.6 \times 10^6 \, m^3$ and contain the most exploited quarries at Mt. Merapi with 1674 workers (63%) of the total number of workers estimated at more than 2600 people per day. Quarrying sand and boulders from volcaniclastic sediment in the lahar corridors are quite dangerous. Villagers are dependent on the resource, which is brought by the hazard. For twenty years, hundreds of trucks and thousands of workers have traveled daily through areas of high lahar hazard.

The rainfall in Putih catchment measured by a rain gauge at Ngandong station, which is located about 5 km from the summit of Mt. Merapi. The average slope based on DEM analysis is 5°, which makes it steeper comparing to the Gendol catchment.

## 7.3 Data and Methodology

7.3.1 Data used

This system used rainfall intensity estimates from X-MP radar, which is installed at Mt. Merapi Museum. The rainfall intensity was estimated by using radar-rainfall algorithms of composite data of specific differential phase ($K_{DP}$) and radar reflectivity factor ($Z_h$), as explained in **Chapter IV**.

The comparison of rainfall estimated from X-MP radar and the rain gauge data is given in **Figure 7.4** (Gendol catchment) and **Figure 7.5** (Putih catchment). In this study rainfall radar adjustment is done by linear equation resulted from the rainfall rain gauge and rainfall radar. Another data used in this study is land use map, terrain data obtained from Digital surface model (DSM), and water depth information from Automatic water level recording (AWLR). Detail information about the data is presented in **Table 7.1**.

Ngandong station is located closer to the location of X-MP radar, which explains the better relationship between the rainfall measured by rain gauge and estimated from X-MP radar. In **Chapter IV**, no adjustment was made as the analysis used the semi-distributed rainfall model. It was assumed that the rainfall in the upstream area triggered the debris flow. In this chapter, the rainfall needs to be adjusted because it is applied to a distributed hydrological model, which is intended to compare the effectiveness of X-MP radar toward the rain gauge.
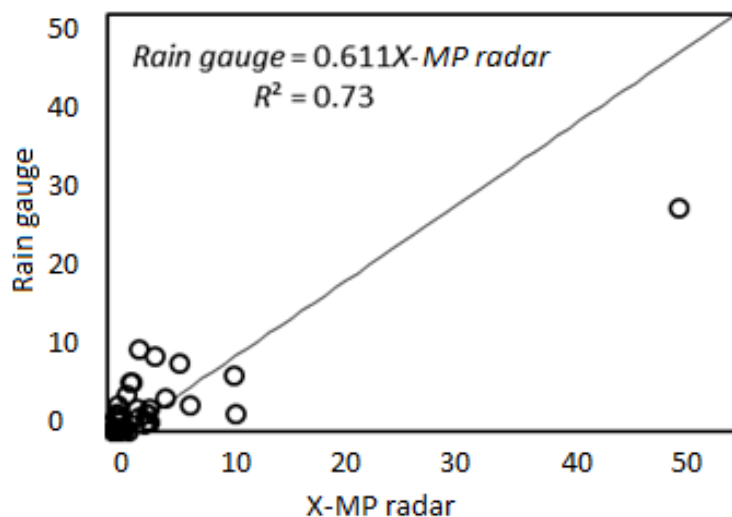


**Figure 7.4** Hourly average rainfall intensity comparison between rain gauge dan X-MP radar (X-radar) for period of Dec. 2015 at Sorasan Station
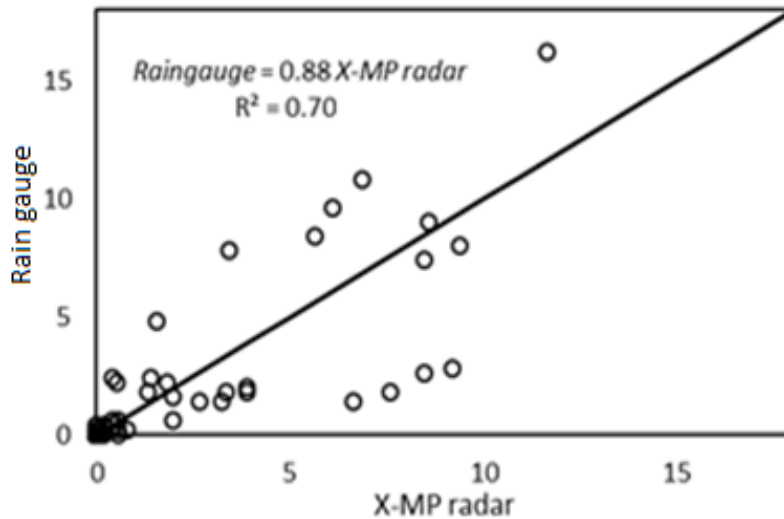
**Figure 7.5** Rainfall intensity [mm/h] comparison between X-MP radar and rain gauge at Ngandong station for the period of February 2016.

**Table 7.1** Data used in the study

| Data | Description | Preparation | Source |
|---|---|---|---|
| X-MP radar data | Rainfall intensity, R [mm/h] at 150 m mesh/2 min | Temporal resolution decrease to be 10 min | X-MP radar cloud system |
| Rain gauge data | Hourly rainfall intensity [mm/h] | | Sorasan Station, Sabo office |
| Terrain data | 5 m mesh, Digital Surface Model (DSM) | Resampled to be 15 m mesh | Japan eXploration Agency (JAXA) |
| Land use | Land use and land cover map, 2013 | Re-class to be 2 classes | Ministry of Forestry of Indonesia |
| Water depth | AWLR measurement of water height from dam crest | | Gadjah Mada University |

7.3.2 Method

The study was conducted by first adjusting the X-MP radar with ground measurement. The short-term rainfall prediction is done according to the description in **Chapter V**. The critical rainfall is calculated based on the method for lahar estimation is based on the description in **sub-chapter 5.3**. The parameters used in the simulation are given in **Table 7.2**.

**Table 7.2** Parameters used in the simulation

| Parameters | Value | Unit |
|---|---|---|
| Simulation time | 40 | h |
| Time step | 1 | s |
| Manning roughness coefficient (river) | 0.06 | |
| Manning roughness coefficient (slope) | 0.5 | |
| Soil depth | 5 | m |
| $k_a$ | $6.06 \times 10^{-6}$ | m/s |

## 7.4 Results

7.4.1 Short-term rainfall prediction and snake line analysis

The ensemble prediction results for Gendol catchment has been presented in **Chapter V**, **Figure 5.11** and the result for Putih catchment is given in **Figure 7.6**. **Figure 7.7** and **Figure 7.8** present the snake line and the critical rainfall analysis for Putih catchment and Gendol respectively.
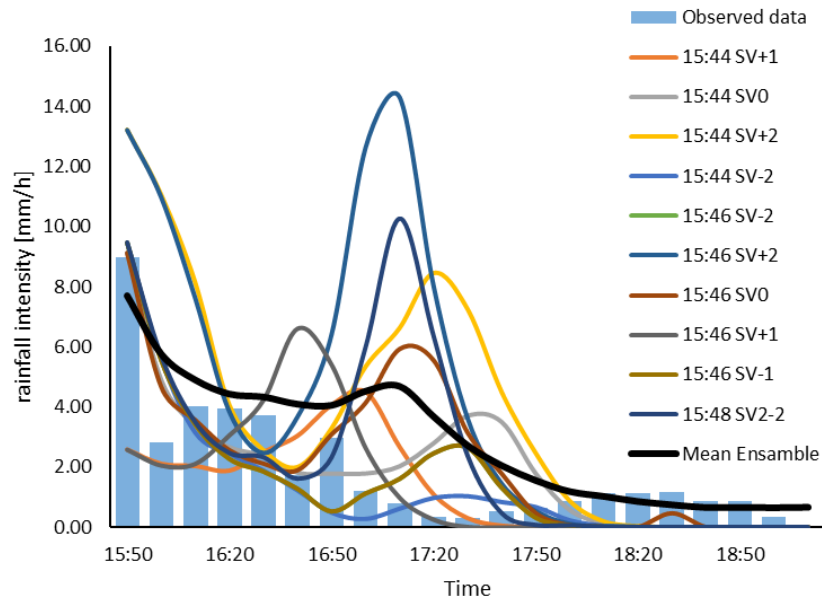


**Figure 7.6** The ensemble prediction of rainfall at Putih catchment
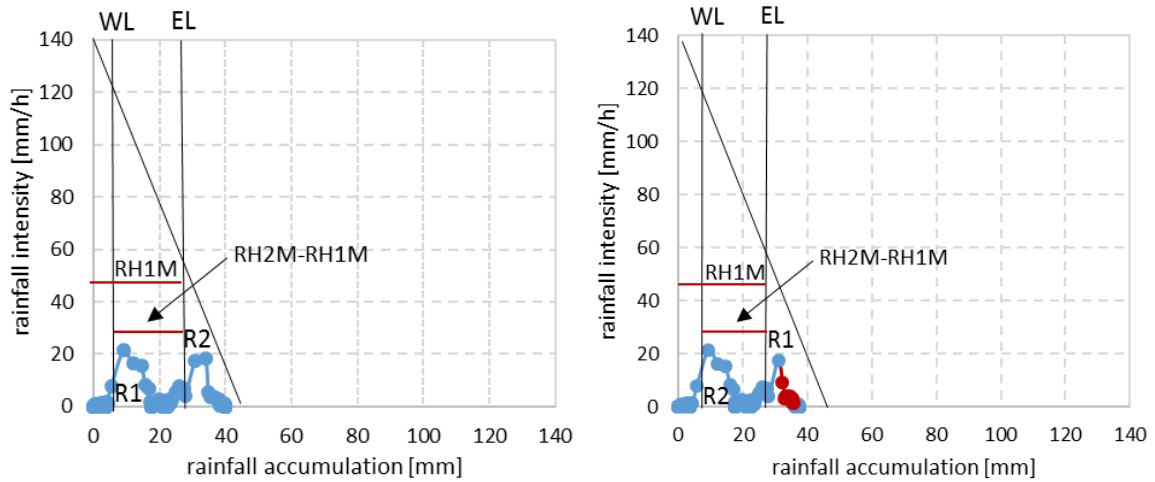
**Figure 7.7** Snake line analysis at Putih catchment based on real X-MP radar data (left) and prediction (right). The red marks and lines show the ensemble prediction values, while the blue marks and line show the rainfall estimate from X-MP radar. The critical line used here is based on Yulinsa (2015)
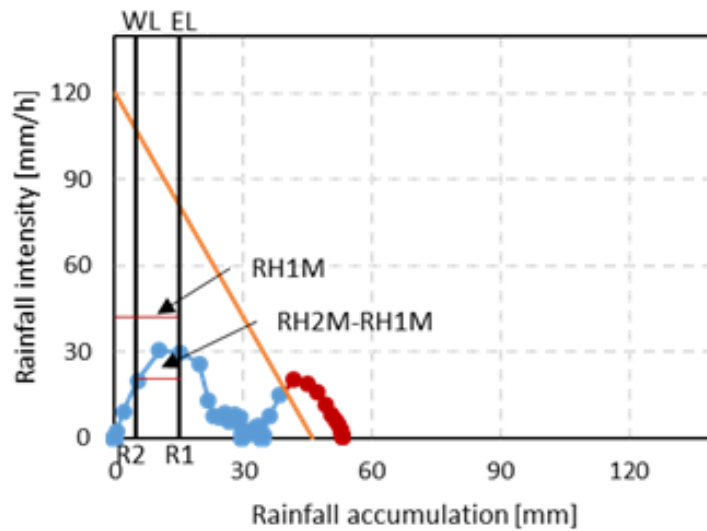


**Figure 7.8** Snake line analysis at Gendol catchment based on ensemble prediction. The red marks and lines show the prediction values, while the blue marks and line show the rainfall estimate from X-MP radar. The critical line used here is based on Fibriyantoro (2015)

Based on the snake line analysis, it is clear that the potency of lahar occurrence is higher at Gendol catchment comparing to the Putih catchment. Hence, the lahar properties calculation is concentrated in Gendol catchment. However, the RRI model and the modified RRI model is also applied to the Putih catchment for analyzing the performance of model and simulation.

7.4.2 Rainfall situation during the simulation period

The hyetograph of rainfall intensity during simulation for Gendol catchment is presented in **Figure 7.9**, while the Putih catchment hyetograph is given in **Figure 7.10**. After the adjustment, the rainfall by X-MP radar in Gendol catchment decreases more than 100 mm/h comparing to the real observed values. On the other hand, rainfall intensity at Putih catchment already shows a similar pattern between the rain gauge and the X-MP radar rainfall. This condition caused by the location of Ngandong station, which is closer to the X-MP radar comparing to the Sorasan station in Gendol catchment. An indication of attenuation of X-MP radar as suspected in **Chapter IV** needs to be investigated more. However, the tendency of attenuation has encouraged the adjustment of X-MP radar rainfall before it is applied to a hydrological model.

The X-MP radar was better to monitor the spatial variability of rainfall, while rain gauges data treated the catchment had uniform rainfall (**Figure 7.11** and **Figure 7.12**). In the Gendol catchment and Putih catchment, the upstream received more rainfall than the downstream area during the period of simulation. More rainfall happened in Gendol catchment compared to Putih catchment. The snake line analysis did not give a recommendation of warning and evacuation at Putih catchment, hence, the potency of lahar in this area was lower than in Gendol catchment.
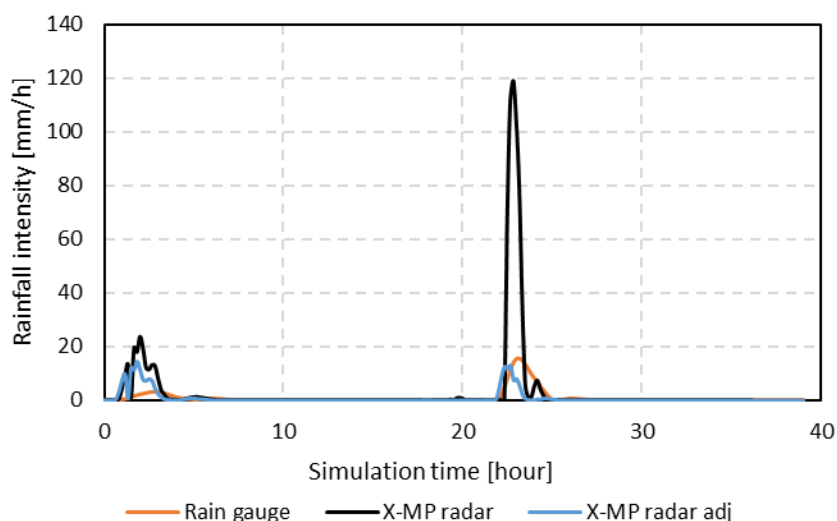


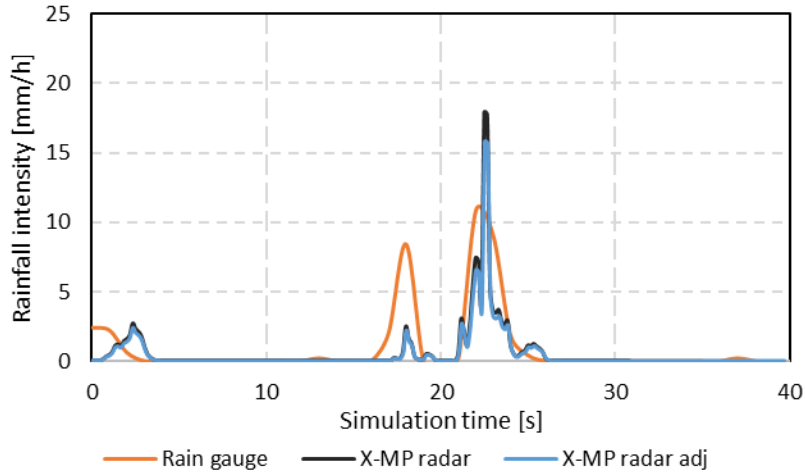**Figure 7.9** Hyetograph of Gendol catchment during the period of simulation

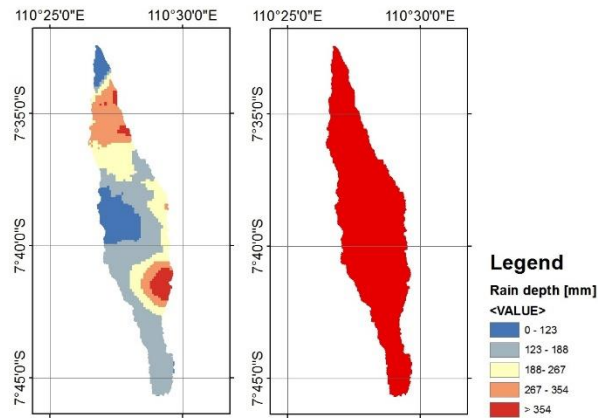**Figure 7.10** Hyetograph of Putih catchment during period of simulation



**Figure 7.11** Spatial distribution of rainfall accumulation from adjusted X-MP radar (left) and rain gauge (right) during simulation at Gendol catchment
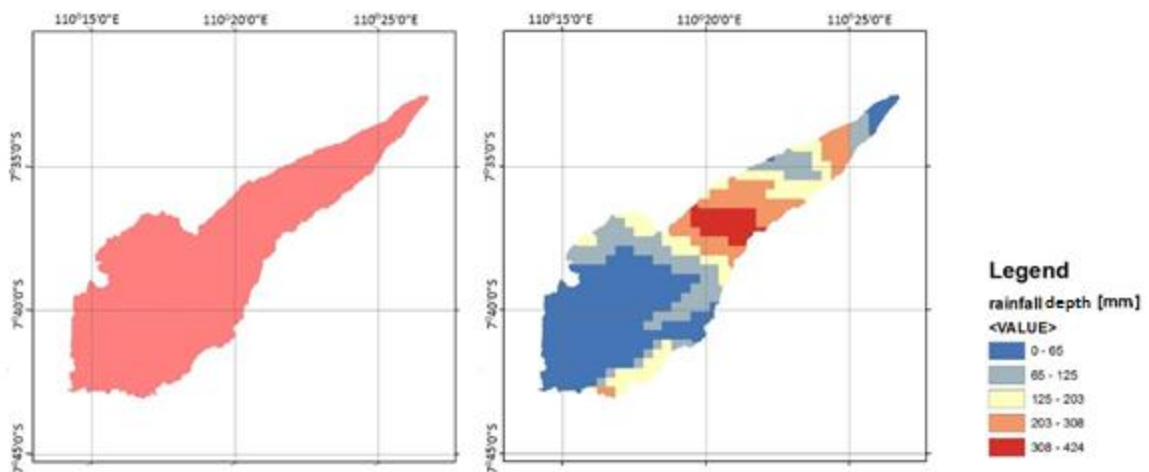


**Figure 7.12** Spatial distribution of rainfall accumulation during period of simulation from rain gauge data at Ngandong Station (left) and adjusted X-MP radar (right)

(2) Ensemble rainfall prediction results.

The Hyetograph of adjusted ensemble rainfall prediction and the adjusted real data estimated by X-MP radar is given in **Figure 7.13**. The adjusted ensemble rainfall prediction shows slight delay compared to the real data. However, both rainfall shows a similar pattern in terms of the rainfall fluctuation.
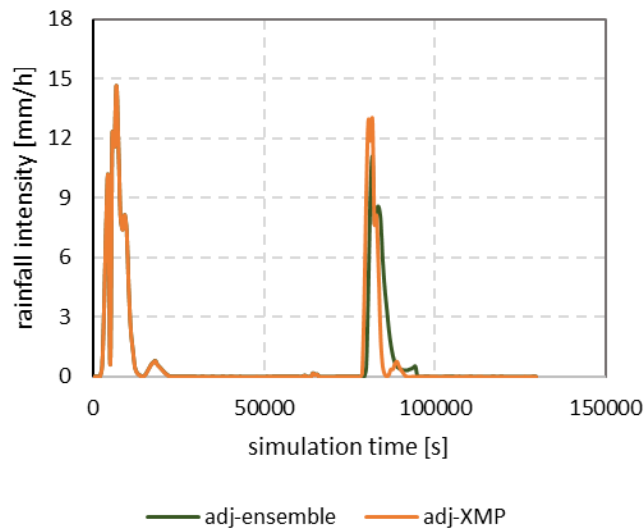


**Figure 7.13** Rainfall hyetograph of the adjusted ensemble prediction and the adjusted X-MP radar

7.4.3 Discharge calculation in the down stream

The discharge and mean velocity in the downstream of Gendol (AWLR point, **Figure 7.2**) are presented in **Figure 7.14**, while **Figure 7.15** is the simulation result for Putih catchment. In the Putih catchment, the AWLR data did not measure the water depth; hence, the point of observation was selected near the Mranggan sabo dam (**Figure 7.3**). The modified model is consistent in giving the lower rate of the unit width discharge and the mean frontal velocity compared to the kinematic wave model. This rate caused by the Manning equation adjustment which slowed down the flow.
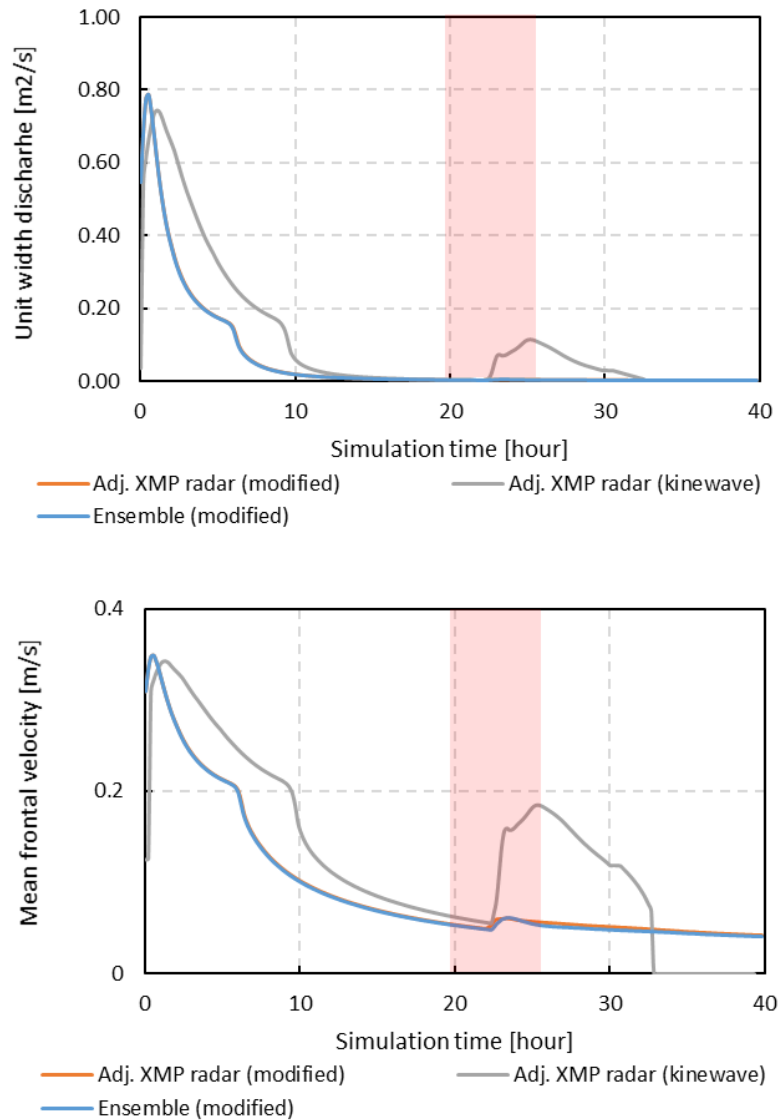
**Figure 7.14** The unit width discharge and mean frontal velocity from adjusted X-MP radar rain rate at Gendol catchment, the red shade indicates the lahar occurrence time in the upstream area.

### 7.4.4 Water depth results

The comparison of flow depth from different models and real observed data are given in **Figure 7.16** (Gendol catchment) and **Figure 7.17** (Putih catchment). In the Gendol catchment, the observed water depth data was not continued, where water depth was not recorded at 18:00-18:50. The comparison time is 12:00 to 21:00 local time, which is equal to 19 to 27-hours of the simulation time. The modified model slightly underestimated the flow depth calculation but managed to give close results to the observed data. In Putih catchment, the modified model also gave significant decrement compared to the kinematic wave model.
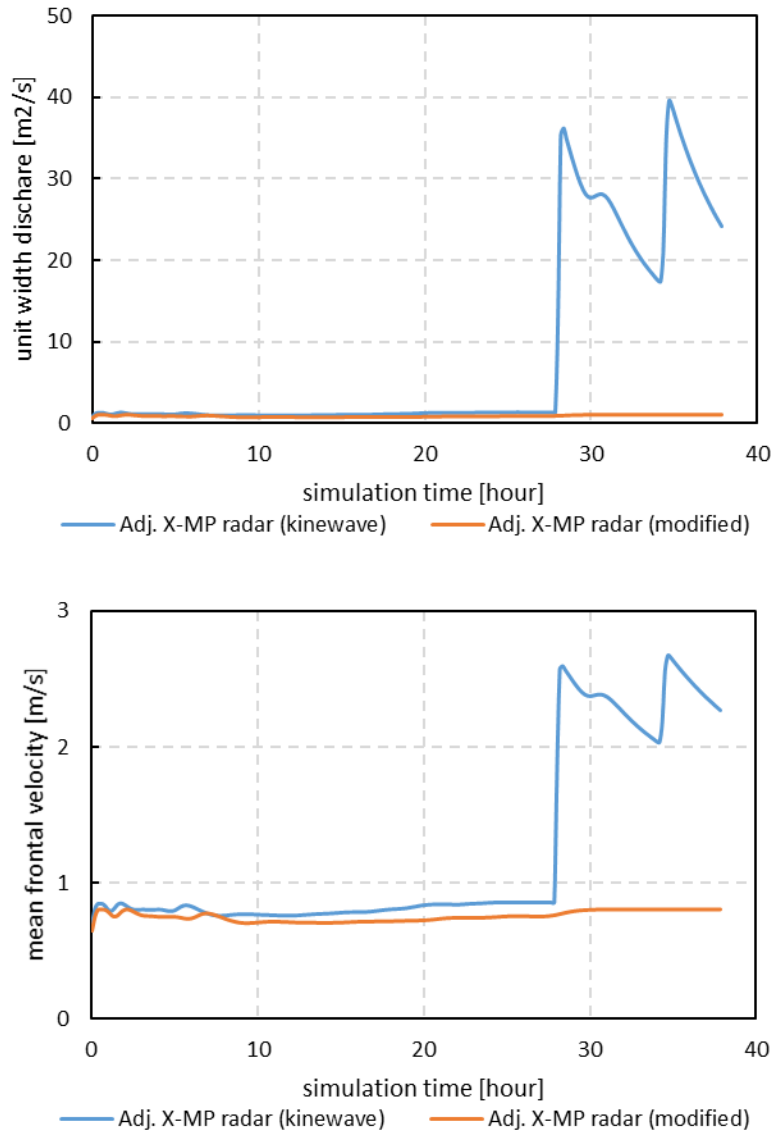
110

**Figure 7.15** The unit width discharge and mean frontal velocity during the simulation period in Putih catchment

### 7.4.5 Lahar properties estimation

Since the potency of the lahar event was higher in Gendol catchment, the analysis of lahar properties was focused on the Gendol catchment. The peak discharge, volume, and travel distance estimated from the coupling of RRI and empirical models are given in **Table 7.3**. Both the ensemble prediction rainfall based model and the adjusted X-MP radar modified model gave close results which are less comparing to the original model.
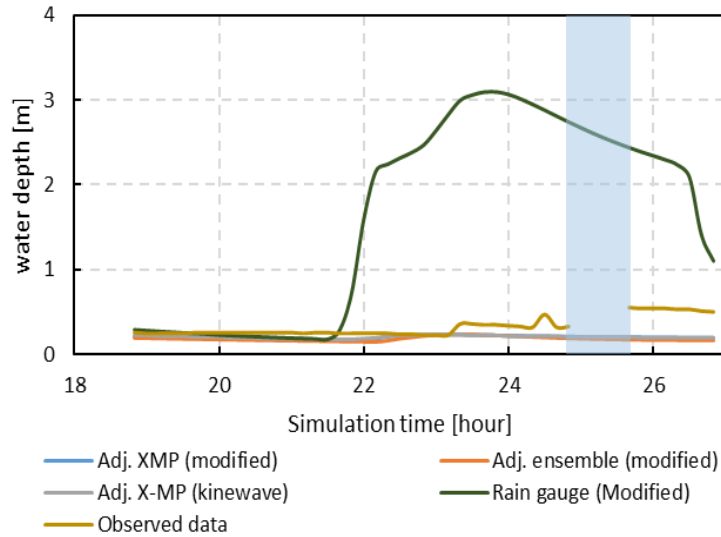
**Figure 7.16** The water depth comparison between models and observed data in the downstream of Gendol catchment, the blue shade shows time were water depth data was not recorded
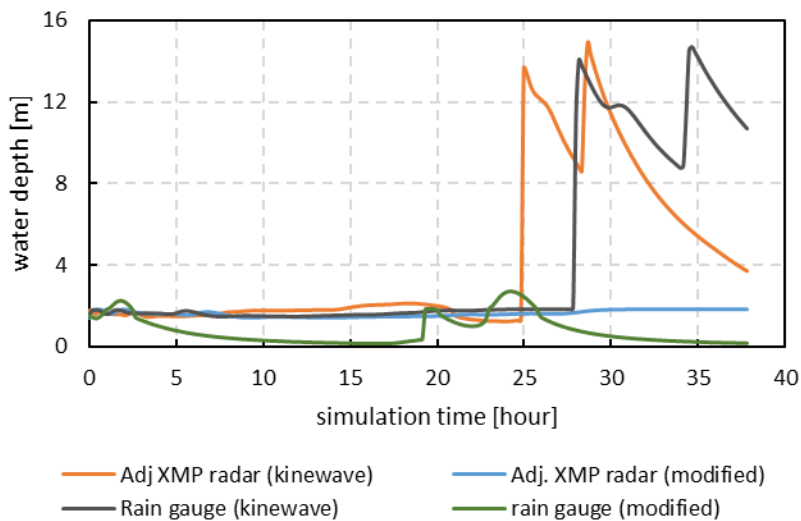


**Figure 7.17** The water depth [m] during the simulation period at an observation point in Putih catchment

The travel distance (*L*) from modified model was 4 km distance (elevation > 1100 m amsl), so the downstream flow belonged to the normal streamflow. This result is similar to the weekly report by BPPTKG (BPTTKG, 2016) which said that the lahar flow only occurred in the upstream area, while the downstream river only experienced flow depth increment (**Appendix 5**). This information also explains why the discharge and velocity were less at the end of the simulation. The reports also did not indicate any lahar potency happened in Putih River.

**Table 7.3** Lahar properties for the period of 17 February 2016, at 15:00-17:00

| Rainfall/Model | Peak Discharge ($Q_p$) [m$^3$/s] | Volume ($M$) [m$^3$] | Travel distance ($L$) [km] |
|---|---|---|---|
| Rain gauge/ modified | 78.7 | 32,000 | 3.9 |
| X-MP radar/ modified | 89.9 | 38,000 | 4.1 |
| Adj. X-MP/ modified | 80.26 | 33,000 | 4.0 |
| Adj. Ensemble/modified | 79.86 | 33,000 | 4.0 |
| Adj. X-MP/ Kinematic wave | 469.7 | 273,296 | 5.8 |

## 7.5 Discussion

7.5.1 Ensemble rainfall prediction and the snake line analysis

The mean ensemble rainfall for Gendol and Putih catchment showed relatively similar fluctuation following the observed data. In Putih catchment the initial condition (IC) perturbation plays important role, as lag-2 minutes gave the poorest results comparing to the mean observed data (**Table 7.4, Appendix 6**).

In general, the statistical analysis for short-term rainfall prediction in Putih catchment showed higher correlation due to the earlier time lag, as lag-6 minutes gave the highest coefficient of determination. On the other hand, Gendol catchment showed that the higher correlation and coefficient of determination was given by the short-time lag (lag-2 minutes). None of the initial conditions for Gendol catchment was statistically different compared to the mean observed data.

In **Table 7.4**, Putih catchment showed increasing reliability by using earlier time lag and the negative singular components gave better result and closer to the real observed data. The opposite happened in Gendol Catchment, where earlier time lag and negative SV showed less correlation, $R^2$, and contrast different variance compared to the real data.

The statistical results indicates that the advection vectors of the rainfall in Merapi catchment works in the different or opposite direction between the southeastern side (Gendol catchment) and the southwestern side (Putih catchment). It seems that the rainfall movement was faster in the southeastern side and slower in the southwestern side. It also showed that the rainfall in those sides of Mountain comes from the different direction, similar to the theory of orographic

rain. Although previous study by Shuin et al. (1996) indicate the tendency of convective cloud formation at Mt. Merapi but the orographic process could also be the main process that influence rainfall at Mt. Merapi and should be investigated more. However, almost no study has been conducted in understanding spatial movement of rainfall at Mt. Merapi

It is recommended to delineate this pattern of rainfall into two different areas if the similar statistical approach of advection vector is used for rainfall prediction. Hence, the movement on the eastern side and the western side could be analyzed differently.

**Table 7.4** Statistical analysis of short-term rainfall forecast based on the IC selection and SV

| IC/SV | Putih catchment | | | Gendol catchment | | |
|---|---|---|---|---|---|---|
| | Pearson | $R^2$ | $P(T \leq t)$ | Pearson | $R^2$ | $P(T \leq t)$ |
| Lag-2 | 0.57 | 0.33 | 0.00 | 0.98 | 0.96 | 0.61 |
| Lag-4 | 0.72 | 0.52 | 0.28 | 0.97 | 0.93 | 0.39 |
| Lag-6 | 0.81 | 0.66 | 0.18 | 0.92 | 0.79 | 0.39 |
| SV0 | 0.45 | 0.20 | 0.00 | 0.96 | 0.91 | 0.34 |
| SV+1 | 0.54 | 0.29 | 0.12 | 0.96 | 0.92 | 0.23 |
| SV-1 | 0.72 | 0.52 | 0.15 | 0.79 | 0.63 | 0.46 |
| SV+2 | 0.54 | 0.29 | 0.01 | 0.96 | 0.76 | 0.49 |
| SV-2 | 0.67 | 0.45 | 0.37 | 0.88 | 0.96 | 0.29 |

Annotation: analysis was done by comparing model results and real data, t-test analysis was done by assuming equal variance (**Appendix 6**).

7.5.2 The effect of Manning roughness coefficient to the flow discharge.

Adjusting the Manning roughness coefficient on the modified model gives the tendency of the coefficient will have greater values in the flatter area. The greater values of Manning roughness coefficient are better to represent the bed roughness in natural streams caused by the presence of bed-forms, step-pools and large boulders in the channel.

Previous study (de Haas and van Woerkom, 2016) has argued the uncertainty of the application of this coefficient into a sediment transport model. Some application then conducted by prior experimental results. Hence, the uncertainty of proper Manning roughness values for the stream is varied at 0.05-0.1.

Although proper values usually obtained by experimental studies, this study has demonstrated a new approach on the Manning roughness coefficient adjustment as a function of slope. In the modified model, the slope has an inverse proportion to Manning roughness coefficient, resulting in gentler slope will have greater resistant and slower flow movement. It also implicitly means that more sediment is carried by the flow.

This technique acts as a stoppage mechanism, which is similar to debris flow behavior, where it usually becomes slower in the gentle slope. **Figure 7.18** shows the relationship between slope and the adjusted Manning roughness coefficient ($n*$) based on equation (6.1) and (6.3).
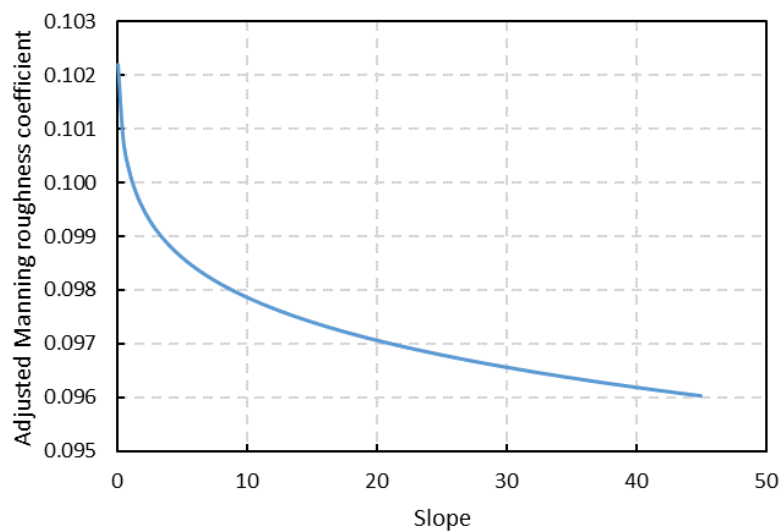


**Figure 7.18** Adjusted Manning roughness coefficient relative to the change of slope.

During the velocity decrement, the materials carried are usually deposited in an alluvial fan. However, the current method could not simulate the deposition process.

The peak discharge and the rainfall peak happened almost in the same time, which strengthen previous research findings about the peak discharge of lahar at Mt. Merapi usually happened within one hour after peak rainfall (de Belizal 2014). As lahar could happen shortly after the rainfall peak, it is clear that getting earlier information of rainfall by rainfall prediction is essential on lahar mitigation.

The MLIT suggests the use of 1-hour rainfall and 2-hour rainfall intensity for getting enough time in issuing the warning and the evacuation to prevent material and especially human loss. As the ensemble prediction is able to give 3-hour rainfall prediction, this method proves to be a useful short-term analysis tool for issuing the early warning. Another aspect that is also

important is even though the spatial correlation of ensemble prediction and real X-MP radar data is still low (**Chapter V, Figure 5.10**), but the application of distributed hydrological model shows similar fluctuation with the real X-MP radar data and closer to the observed values (water depth) as given in **Figure 7.16**.

7.4.3 The effect of Manning roughness coefficient to the water depth.

The simulation in Gendol catchment showed that rain gauge based model overestimated the flow depth. The overestimations mainly caused by the rain gauge-based model treated all the area of the catchment to have uniform rainfall values (**Figure 7.16**).

Putih catchment showed the more significant fluctuation of water depth between the modified model and the original kinematic wave model (**Figure 7.17**). Putih catchment has steeper average slope compared to the Gendol catchment, which causes this significant difference of the water depth. The average slope of Putih catchment is $5.00^o$ and the average slope of Gendol catchment is $3.68^o$. Because of the adjustment of Manning roughness coefficient is done only on river cell, causing the modified model application in Putih River gave slower flow, which is significant compared to Gendol River's flow and the original kinematic-wave model.

Another fact that Gendol River has more sabo dam comparing to the Putih River should also be taken into consideration. The model used DSM which does not ignore the existence of sabo dam in the river stream. The sabo dam modified the riverbed, causing the slope of the river to be flatter, in order to reduce the flow velocity.
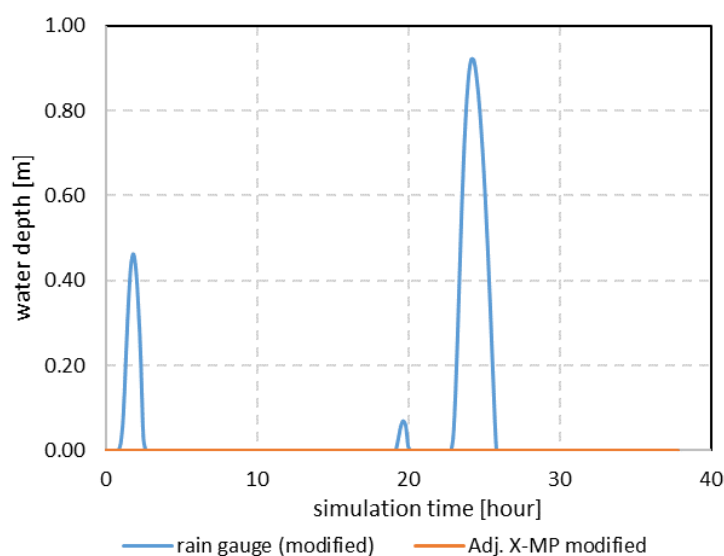


**Figure 7.19** The inundation depth at the point of observation in Putih catchment based on the modified model.

116

Although the rain gauge based model in the Putih River shows a more similar pattern to the kinematic wave model, but it is suspected to be an overestimation values during the increment happened at earlier simulation and between the $20^{th}$ to the $30^{th}$ hour of the simulation (**Figure 7.17**). This condition could be explained by further analysis of water depth on the non-river cell in the same point, where an inundation of 0.01-0.92 m has resulted from the simulation (**Figure 7.19**). Relying on the fact that the lahar on 17 February 2016 were only reported in Gendol Catchment, it is more convincing to decide that the X-MP radar-based model gives more reliable result compared to the rain gauge-based model.

## 7.6 Recommendation

Although the proposed system can give faster calculation and earlier information, the model has some limitation as mentioned in **Chapter VI**. This method is only effective to be applied if the remaining material of volcano has decreased significantly, hence the lahar could be treated as hyper-concentrated flow. It also assumed that lahar occurs only in river cell, hence the other debris flow occurrence in the non-river cell cannot be estimated by this method.

Moreover, the method did not separate the solid constituent from the fluid constituent, hence it cannot give a mechanistic understanding about the movement of sediment within the flow. In the future, better mechanistic lahar flow model should be developed; hence, the behavior of lahar could be understood better. However, this current developed method that is proposed by this research will be useful in terms of early warning and evacuation recommendation, which require faster response and recommendation.

# CHAPTER VIII
# SUMMARY AND FUTURE WORK

## 8.1 Summary

Lahar is a rapidly flowing, high-concentration, poorly sorted sediment-laden mixture of rock debris and water from a volcano that is usually triggered by rainfall. It is one of the most disastrous sediment hazards, which has caused lots of devastation. Between the 17th and 19th century, lahars are responsible for 17% of deaths due to volcanic disasters, essentially in Indonesia.

The behavior of lahar covers debris flow, hyper-concentrated flow, and bed stream. Debris flow is a mixture of clastic material including boulders and woody debris, where the lubricated inter-particle collision is the dominant mechanism for energy dissipation. A hyper-concentrated flow is an intermediate flow between fluvial flow and debris flow with sediment concentration ranges between 5-60 %.

Most studies about lahar and debris flow have been conducted by analyzing the relationship between lahar occurrence and behavior under severe rainfall intensity. Thus, rainfall information becomes a very important aspect for lahar and debris flow studies. The small-scale disaster as debris flow requires higher spatial information of rainfall. Debris flow and lahar can occur in a small scale within less than 1 km$^2$, hence the application of weather radar which is able to give not only fine spatial resolution but also higher temporal resolution becomes desirable for lahar monitoring and assessment.

At Mt. Merapi of Indonesia, lahar occurs as the secondary disaster that requires proper disaster management system. An installation of X-band multi-parameter radar (X-MP radar) to monitor rainfall in this volcano is expected to give better rainfall information and real-time rainfall-induced lahar potency comparing to the ground-based measurement.

This study focused on the utilization of X-MP radar for rainfall monitoring and lahar estimation at Mt. Merapi. The rainfall intensity derived from X-MP radar still has some uncertainties where it is generally smaller than rain gauges' data. However, several problems like data

discontinuity and great bias between each station at Mt. Merapi has encouraged the utilization of X-MP radar for better rainfall information spatially and temporally.

The study is conducted by analyzing the rainfall-lahar relationship by some hydrological models application. First, rainfall data from rain gauge and X-MP radar is applied to the HyperKANAKO model for lahar simulation. The second step is application of ensemble short-term rainfall prediction for defining the potency of lahar occurrence under critical rainfall values. Last is combining the rainfall prediction values into a modified distributed rainfall-runoff inundation (RRI) model. The modification is done empirically so that this model becomes more suitable for lahar simulation.

The application of rain gauge data for lahar studies is able to simulate the lahar occurrence, just if a finer terrain data is used. It is also known that lahar occurs within less than 1-hour from the recurring event. Hence, the real-time rainfall information by short-term ensemble rainfall forecasting is also required for the earlier warning.

An application of short-term rainfall forecasting to rainfall intensity obtained by X-MP radar is able to predict lahar occurrence. Applying the values to rainfall-runoff distributed, earlier information of lahar occurrence can be obtained. However, the modified model still has some limitations as it cannot calculate the erosion and deposition happened, and assuming lahar behaves as hyper-concentrated flow.

## 8.2 Conclusions

The results showed that the remote monitoring of lahar prediction by X-MP radar and hydrological and numerical model was well performed to deal with the problems of rainfall data unavailability and inaccessible location of rain triggered lahar generation. The results show this method is feasible for lahar mitigation in terms of fast response and earlier warning information.

The outcomes of this work are concluded based on the sub-objectives as follows.

1. By applying rainfall information and terrain data (DEM and DSM), the lahar could be simulated by a numerical and hydraulic model of HyperKANAKO. The rainfall intensity is important for 1D simulation. This indicates rainfall role on triggering lahar, as the model assumes debris flow or lahar initiated as a 1D model, which later transforms into a 2D model for the deposition. Terrain data quality is important to analyze the inundation and the deposition area. False deposition area was resulted by

119

using the lower resolution of 30 m and 90 m resolution, while the finest resolution at 5 m could identify the channel stream and give better simulation results.

2. The X-MP radar is known to be an important and useful tool for giving higher spatial and temporal resolution of rainfall. The X-MP radar could be used to replace the rainfall data from rain gauges directly. Integrating the X-MP radar to a numerical and hydraulic model of HyperKANAKO was able to simulate lahar occurrence based on a real event on 17 February 2016. However, increasing flow velocity was monitored in the downstream area, where it should have a slower rate of discharge and velocity.

3. An application of short-term ensemble rainfall prediction is a useful study in order to give earlier lahar potency information. The analysis was done by applying the ensemble rainfall prediction to a critical line. The predicted rainfall in Gendol catchment, showed the potency of lahar occurrence in this catchment after the snake line exceeded the critical line. Relying on this result, further analysis of the hydrometeorological condition in the catchment for lahar occurrence is recommended by applying the predicted rainfall values into a modified distributed model of the RRI.

4. The modification of RRI model for lahar estimation was done by applying some empirical equations and X-MP radar rainfall integration. The Manning roughness coefficient was modified as an inverse proportion to the slope, caused the model becoming able to perform stoppage mechanism of lahar. The modified model was able to give the similar result to the real condition, and so was the predicted rainfall values obtained by the ensemble model. The ensemble prediction correctly confirmed the lahar event based on the real condition in Gendol catchment, while in Putih catchment were the lahar occurrence was not reported, the predicted rainfall and the snake line analysis did not give a false alarm. An application of adjusted ensemble prediction model gave a similar result with the real data of adjusted X-MP radar. The simulation also showed the superiority of X-MP radar comparing to the rain gauge based model, as the later mention overestimated the water depth, resulting in Putih River to have some inundation area which had never been reported.

## 8.3 Recommendations

Besides some findings achieved by this proposed method, some suggestions for future study improvement are given as follows.

1. Due to some limitation of the models and a very dynamic condition of the volcanic area, some similar studies are still required. A better physical lahar model is required for understanding the mechanism and behavior of lahar.

2. Improvement is also required for dealing with the uncertainty of rainfall-radar data which is used in this study.

3. The advection model used by the ensemble prediction was developed in Japan. The rainfall characteristic and movement caused by the convective rainfall happens at Mt. Merapi will be different with rainfall in the sub-tropical area. The effect of mountainous area also indicated the orographic effect also works at Mt. Merapi. Analysis of rainfall characteristic and movement diurnally and seasonally by X-MP radar is important to develop better rainfall prediction model with higher spatial accuracy.

# REFERENCES

Awal, R., Nakagawa, H., Kawaike, K., Baba, Y., Zhang, H. Prediction of flood/debris flow hydrograph due to landslide dan failure by overtopping and sliding. Annu. Disas. Prev. Res. Inst., Kyoto Univ. 51B, 603–611. 2008. Available from. http://www.dpri.kyoto-.ac.jp/nenpo/no51/ronbunB/a51b0p61.pdf.

Aghakouchak, A., Habib, E., Bardossy, A. Modelling Radar Rainfall Estimation Uncertainties: Random Error Model, J.Hydrol. Engineering, Vol. 15, No. 4, 265-274, 2010

Aleotti, P. A warning system for rainfall-induced shallow failures. Eng Geol 73. pp. 247–265, 2004.

Arrattano, M., Savage, W.Z. Modelling debris flows as kinematic waves, Bull. of the International Association of Engineering Geology, No. 49. pp.3-13, 1994.

Bagnold, R.A. Experiments on a gravity-free dispersion of large solid spheres in a Newtonian fluid under shear stress. Proc. R. Soc. Lond. 225, pp. 49-63. 1954, .https://dx.doi.org/10.1098/rspa.1954.0186.

Berenguer, M.,Sempere-Torres, D., & Hurlimann, M. Debris-flow Forecasting at Regional Scale by Combining Susceptibility Mapping and Radar Rainfall, J. Nat. Hazard Earth Sys, 15, 587-602, 2015.

Berne, A., Krajewski, W.F. Radar for hydrology: unfulfilled promise or unrecognized potential? Adv. Water Resour. 51, 357–366, 2013. https://dx.doi.org/10.016/j.advwaters.2012.05.005.

Beverage, J.P., Culbertson, J.K. Hyperconcentrations of suspended sediment, J. Hydaul. Div. Am. Soc. Civ. Eng., 90 (HY6), pp. 117-128, 1964.

Bhagabati, S.S., Kawasaki, A. Consideration of the rainfall-runoff-inundation model for flood mapping in a deltaic area of Myanmar. Hydrological research Letter. Vol. 11, Iss.3, 2017. https://dx.doi.org/10.371/hrl.11.155

Castruccio, A., Clavero, J. Lahar simulation at active volcanoes of the Southern Andes; implications for hazard assessment. J. Nat. Hazards 693–716, 2015. http://dx.doi.org/10.1007/s11069-015-1617-x.

Cannon, S. H. Regional rainfall-threshold conditions for abundant debris- flow activity. Landslides, floods, and marine effects of the storm of January 3-5, 1982, in the San Francisco Bay region, California, U. S., Geological Survey Professional Paper no. 1434, eds. Ellen, S. D. & Wieczorek, G.. F. pp. 35-42, 1988.

Centre for Research and Technology, Development of Geology Disaster (BPPTKG). Weekly Report of Mount Merapi (in Bahasa Indonesia). http://www.merapi.bgl.esdm.go.id/aktivitas_terakhir.php, 2016. [Accessed Feb,27. 2016].

Chen., J.C., Chuang, M.R. Discharge of landslide-induced debris flows: case studies of Typhoon Morakot in southern Taiwan. Nat. Hazards Earth Sys. Sci., 14., pp. 1718-1730. 2014.doi:10.5194/nhess-14-1719-2014.

Chen, J.C., Jan, C.D., Huang, W.S. Characteristic pf rainfall triggering of debris flows in the Chenyulan watershed, Taiwan. Nat. Hazards Earyh Syst. Sci., 14, 1015-1023, 2013. Doic:10.5194/nhess-13-1016-2013.

Chen, C.Y., Fujita, M. An analysis of rainfall-based warning systems for sediment disasters in Japan and Taiwan. International Journal of Erosion Control Engineering. Vol. 6, No. 2, pp. 47-57, 2013. https://dx.doi.org/10.13101/ijece.6.47.

Chen, C.Y., Lin, L.Y., Yu, F.C., Lee, C.S., Tseng, C.C., Wang, A.H., Cheung, K.W.. Improving debris flow monitoring in Taiwan by using high-resolution rainfall products from QPESUMS. Nat. Hazards. 40 (2), 447–461, 2007. http://dx.doi.org/10.1007/s11069-006-9004-2.

Chiang, S.H., Chang, K.T. Application of radar data to modelling rainfall induced landslides. eomorphology 103 (3), 299–30., 2009. http://dx.doi.org/10.1016/j.geomorph.2008.06.012.

Chow, V.T. Open Channel Hydraulics, McGraw-Hill College, 1959.

Corominas, J., Moya, J. Reconstructing recent landslide activity in relation to rainfall in the Llobregat river basin, Eastern Pyrenees, Spain. Geomorphology, 30, pp. 79-93, 1999

Crozier, M.J. Prediction of rainfall-triggered landslides: a test of the antecedent water status model. Earth Surf Proc Land 24, pp. 825–833, 1999

Cui, P., Cuo X.J., Zuong, J.Q..2016 Determination of the runoff threshold for triggering debris flows in the area affected by the Wenchuan earthquake. Nat. Hazards Earth Syst., Vol. 2., pp. 4659-4684.

Cui, P. Studies on condition and mechanism of debris flow initiation by means of experiment, Chinese Sci. Bull., 37, pp. 759–763,1992.

D'Agostino, V., Marchi, L. Debris flow magnitude in the Eastern Italian Alps: data collection and analysis. Phys. Chem. Earth 26 (9), 657–663, 2001. https://dx.doi.org/101.1016/S1464-1917(01)00064-2.

David-Novak, H.B., Morin, E., Enzel, Y. Modern extreme storms and the rainfall thresholds for initiating debris flows on the hyperarid western escarpment of the Dead Sea. Israel. Bull. Geol. Soc. Am. 116 (5–6), 718–728, 2004. http://dx.doi.org/10.1130/B25403.2.

de Belizal, E., Lavigne, F., Hadmoko, D.S., Degai, J.P., Dipayana, G.A., Bachtiar, W.M., Marfai, M.A., Coquet, M., Le Mauff, B., Robi, A.K., Vidal, C., Cholik, N., and Aisyah, N. Rain-triggered Lahar Following the 2010 eruption of Merapi Volcano Indonesia. J. Volcanol. Geoth. Res. Vol.261, pp.330-347, 2013.

De Blasio, F.V., Elverhoi, A., Issler, D., Harbitz, C.B., Bryn, P., Lien, R. Flow models of natural debris flows originating from overconsolidated clay materials. Mar. Geol. 213, 439–455, 2004. http://dx.doi.org/10.1016/j.margeo.2004.10.018.

de Haas, T., van Woerkoem, T. Bed scour by debris flows: experimental investigation of effects of debris-flow composition. Earth Surf. Process. Landforms 41, pp. 1951–1966, 2016. http://dx.doi.org/10.1002/esp.3963.

Fibriyantoro, E.A. Development of warning criteria for lahar flow disaster in Gendol River area of Mount Merapi. Journal of the Civil Engineering Forum. Vol.1 No. 1, Pp. 18-21, 2013.

Fitriyadi. Analysis of Effective Rainfall Intensity and working rainfall for Basic warning criteria Development on lahar flow event. Civil Engineering Forum. Volume XXII/1 - January 2013. pp. 1335-1340, 2013.

Fujita, T., Stensrud, D.J., Dowell, D.C. Using precipitation observations in a mesoscale shortrange ensemble analysis and forecasting system, Weather and Forecasting, Vol. 23(3), pp. 357-372, 2008.

Gonda, Y., Legono, D. & Santosa, U. B. *Debris Flow and Flash Floods after the 2010 Eruption of Mt. Merapi, Indonesia.* Yogyakarta, 2013.

Glade T, Crozier M.J, Smith, P. Applying probability determination to refine landslide-triggering rainfall thresholds using an empirical "Antecedent Daily Rainfall Model". Pure Appl Geophys, 157(6/8), pp. 1059–1079, 2000.

Gregoretti, C., Fontana, G. D. The triggering of debris flow due to channel-bed failure in some alpine headwater basins of the Dolomites: analyses of critical runoð, Hydrol. Process., 22, pp. 2248–2263, 2008.

Gregoretti, C. The initiation of debris flow at high slopes: experimental results, J. Hydraul. Res., 38, pp. 83–88, 2000.

Habib, E., Ciach, G.J., Krajewski, W.F. A method for filtering out raingauge representativeness errors from the verification distributions of radar and raingauge rainfall. Adv. Water Resour. 27, 67–980, 2004. http://dx.doi.org/10.1016/j.advwatres.2004.08.003.

Hapsari, R.I. Development of Probabilistic Hydrometeorological Prediction for Urban Flood Disaster Prevention. University of Yamanashi, Yamanashi. Doctoral Thesis, 2011.

Hardjosuwarno, S., Sukatja, C.B., Yunita, F.T. Early Warning System for Lahar in Merapi. Global Assessment Report on Disaster Risk Reduction, 2013. Available from. https://www.unisdr.org/we/inform/publications/50053, 2013.

Hasnawir, Kubota T. Analysis fof critical value of rainfall to induce landslide and debris-flow in Mt. Bawakaraeng Caldera, South Sulawesi, Indonesia. J. Fac. Agr., Kyushu Univ., 53 (2), 523–527, 2008.

Heiken, G., Wohletz, K. Tephra deposits associated with silicic domes and lava flows. Geological Society of America, Special Paper 212, pp. 55-76, 1987. Available from: http://www.lanl.gov/orgs/ees/geodynamics/Wohletz/Silicic_Dome_Tephra.pdf

Heyerdahl, H., Harbitz, C.B., Domaas, U., Sandersen, F., Tronstad, K., Nowacki, F., Engen, A., Kjekstad, O., Dévoli, G., Buezo, S.G, Diaz, M.R, Hernandez, W. Rainfall induced lahars in volcanic debris in Nicaragua and El Salvador: practical mitigation. Proceedings of International Conference on Fast Slope Movements – Prediction and Prevention for risk Mitigation, IC-FSM2003. Naples: Patron Pub, pp.275–282, 2003.

Huggel, C., Schneider D., Miranda, P.J., Granados, H.D., Kääb, A. Evaluation of ASTER and SRTM DEM DATA for lahar modeling: A case study on lahar from Popocatépetl Volcano, Mexico. J Volcanol Geoth Res. Vol.170, pp. 99-11, 2007.

Hsu, S.M., Chiou, L.B., Lin, G.F., Chao, C.H., Wem, H.Y., Ku, C.Y., Applications of simulation technique on debris-flow hazard zone delineation: a case study in Hualien County. Taiwan, Nat. Hazard. Earth. Sys. 10, 535–545. 2010. http://doi.org/10.5194/nhess-10-535-2010.

Hutter, K., Svendsen, B., Rickenmann. Debris flow modeling: a review. Continuum Mech. Thermodyn. 8, pp. 1–35, 1994. http://doi.org/10.1007/BF01175749.

Ikeya, H. Debris flow and its countermeasures in Japan, Bulletin of the International Association of Engineering Geology. No. 40. Paris, pp. 15-33, 1989

Ikhsan, J., Fujita, M., Takabayashi, H. Sediment disaster and resource management in the mount Merapi area, Indonesia. Int. J. Erosion Control Eng. 3 (1), 43–52, 2010.http://doi.org/10.13101/ijece.3.43.

Iverson, R. M. Debris flows: behaviour and hazard assessment. Geology Today, 30, pp.15–20, 2014. https://dx.doi.org/10.1111/gto.12037.

Iverson, R. M. The Physics of Debris Flow. Rev.Geophys. Vol.35, pp.245-296, 1997.

Iverson, R.M., Schilling, S.P. and Vallance, J.W. Objective delineation of lahar inundation hazard zones. GSA Bulletin. Vol.100, pp. 972–984, 1998.

Jakob, M., Hungr O. Introduction. In: Hungr O, Jakob M (eds) Debris-flow hazards and related phenomena. Springer-Praxis, Berlin, pp 1–7, 2005

Jarret, R.D. Water-Resources Investigation Report, 85-40004. US Geological Survey, Lakewood, Colorado, 1985.Available at. https://pubs.usgs.gov/wri/1985/4004/report.pdf.

Jitousono, T., Shimokawa, E., Tsuchiya, S., Haryanto, Djamal, H. Debris flow following the 1984 eruption with pyroclastic flows in Merapi volcano, Indonesia. Proc. Workshop on Erosion Control through Volcanic Hydrological approach (WEVCHA), Sabo Technical Center, Yogyakarta, 10-11 January, pp. 1-26, 1995.

Jones, R., Thomas, R.E., Peakall, J., Manville, V. Rainfall-runoff properties of tephra: simulated effects of grain-size and antecedent rainfall. Geomorphology, pp. 39–51, 2017. https://dx.doi.org/10.1016/j.geomorph.2016.12.023.

Jousset, P., Pallister, J., Surono. The 2010 eruption of Merapi Volcano, J. Volcanol. Geotherm. Res., Vol. 261, pp. 1-6, 2013. https://dx.doi.org/10.1016/j.volgeores.2013.05008.

Julien, P. Y., Leon, S.A.C. Mud floods, mudflows and debris flows classification, rheology and structural design, 2000.

Kato, A., Maki, M. Localized heavy rainfall near Zoshigaya, Tokyo, Japan on 5 August, 2008 observed by X-band polarimetric radar – preliminary analysis, SOLA, Vol. 5, pp. 89-92, 2009. https://dx.doi.org/10.2151/sola.2009-023.

Kim, S., Tachikawa, Y, Y., Sayama, T., Takara, K. Ensemble flood forecasting with stiochastic radar image extrapolation and a distributed hydrologic model. Hydrological Processess, vol. 23, pp. 597-61, 2009.

Kim, K., Nakagawa, H., Kawaike, K., Zhang, H. A study of debris flow outflow discharge at a Series of sabo dams. J. JSNDS 33, pp. 43–45, 2014. Available from. www.jsnds.org/ssk/ssk_33_s_043.pdf.

Kim, S., Tachikawa, Y., & Takara, K. Flood Forecasting System Using Weather Radar and Distributed Hydrological Model, Annuals of Disas. Prev. Res. Inst., Kyoto Univ., No. 49 B, 2006. pp. 55-65, 2006

Kusumawardhani, R., Kurniadhi, R., Mukhlisin, M., Legono, D. Rainfall threshold for triggering debris flow on Merapi volcano Area, Yogyakarta, Indonesia, AIP Conference Proceedings. Vol. 1818 (1), pp. 20-27, 2017, http://dx.doi.org/10.10631/1.4976891.

Lashari, Kusumawardani, R., Ferdia Prakasa. Rainfall distribution analysis at Mt. Merapi area by Aritmatic and Polygon Methods (In Bahasa Indonesia). Jurnal Teknis Sipil dan Perencanaan. Vol 19(1), Pp. 39-48, 2017

Lavigne, F., Thouret, J.C., Hadmoko, D.S., Sukatja, C.B. Lahars in Java: initiations, dynamics, hazard assessment and deposition processes. Forum Geografi 21, pp. 17-3, 2007. http://dx.doi.org/10.23917/forgeo.v21i1.1822.

Lavigne, F. Rate of sediment yield following small-scale volcaniceruptions: a quantitative assessment at the Merapi and Semeru stratovolcanoes, Java, Indonesia. Earth Surf. Process. Landforms 29, pp. 1045–1058, 2004. http://dx.doi.org/10.1002/esp.1092.

Lavigne, F., Suwa, H. Contrast between debris flows, hyperconcentrated flows and stream flows at a channel of Mount Semeru, East Java, Indonesia. Geomorphology, 61. Pp. 41-58, 2004.

Lavigne, F., Thouret, J.C. Sediment transportation and deposition by rain-triggered lahars at Merapi volcano, Central Java, Indonesia. Geomorphology 49 (1–2), 45–69, 2003 http://dx.doi.org/10.1016/S0169-555X(02)00160-5.

Lavigne, F., Thouret, J.C., Voight, B., Young, K., La Husen, R., Marso, J., Suwa, H., Sumaryono, A., Sayudi, D.S., Dejean, M.,. Instrumental lahar har monitoring at Merapi Volcano, Central Java, Indonesia. J. Volcanol. Geotherm. Res. 100, pp. 457–478, 2000a. http://dx.doi.org/10.1016/S0377-0273(00)00151-7.

Lavigne, F., Thouret, J.C., Voight, B., Suwa, H., Sumaryono, A. Lahar at Merapi Volcano, Central Java: an overview. J Volcanol. Geoth. Res. 100 (1–4), pp. 423–456, 2000b. http://dx.doi.org/10.1016/S0377-0273(00)00150-5.

Lee, S., Lee, C., Lee, S. A comparison of the Landsat image and LAHARZ-simulated lahar inundation hazard zone by the 2010 Merapi eruption. Bull Vulcanol 77(46), pp. 1–13, 2015. http://dx.doi.org/10.1007/s00445-015-0920-4.

Legono, D. and Pamudji, R.A. Lahar Flow Disaster, Human Activities and Risk Mitigation on Volcanic Rivers –Case Study of Rivers on Mt. Merapi Slope, Indonesia, Disaster Prevention Research Institute Kyoto University, 2015.

Legowo, D. Volcanic debris control applied in Indonesia. J. Hydrol. 20, pp. 122–134, 2003. Available from. http://www.hydrologynz.co.nz/downloads/JoHNZ_1981_v20_1_Djoko%20Legowo.pdf

Li, T. Mountain hazards in China. In: Owens PN, Slaymaker O (eds) Mountain geomorphology. Arnold, London, pp. 219–241, 2004.

Major, J.J., Pierson, T.C., Dinehart, R.L., Costa, J.E. Sediment yield following severe volcanic disturbance—A two-decade perspective from Mount St. Helens. Geology, (9), pp. 819–822, 2000. https://doi.org/10.1130/0091-7613(2000)28<819:SYFSVD>2.0.CO;2

Maki, M., Park, S.G., Bringi, V.N. Effect of natural variations in rain drop size distributions on rain rate estimator of 3 cm wavelength polarimetric radar. Journal of the Meteorological Societyof Japan, Vol. 83, No.5, pp.871-893, 2005. https://dx.doi.org/10.2151/jmsj.83.871

Mananoma, T., Wardoyo, W, The influence of rainfall characteristics change on sediment migriation patterm after Merapi Erupsion 2006. International Seminar on "Climate Change Impacts on Water Resources and Coastal Management in Developing Countries". Manado 11-13 May 2009, 2009.

Marchi, L., D'Agostino, V. Estimation of debris-flow magnitude in the Eastern Italian Alps. Earth Surf. Process. Landforms, 29, pp. 207–220, 2004. http://dx.doi.org/10.1002/esp.1027

Marra, F., Nikolopaulus, E.I., Creautin, J.D., Borga, M. Radar rainfall estimation for the identification of debris-flow occurrence thresholds. J. Hydrol. 519 (B), pp. 1607–1619, 2014. http://dx.doi.org/10.1016/j.jhydrol.2014.09.039.

Martin, D. A., Moody, J. A. Comparison of soil infiltration rates in burned and unburned mountainous watersheds, Hydrol. Process., 15, pp. 2893–2903, 2001.

Milliman, J.D., Syvitski, J.P. Geomorphic/Tectonic Control of Sediment Discharge to the Ocean: The Importance of Small Mountainous Rivers. The Journal of Geology 100. No. 5, pp. 525-544, 1992. https://dx.doi.org/10.1086/629606

Ministry of Land, Infrastructure, and Transport (MLIT). 2004. Guidelines for Construction Technology Transfer, Development of Warning and Evacuation System against Sediment Disaster in Developing Countries. Infrastructure Development Institute, Japan.

Mulyana, A.R.R., Sutanto, S.J., Akhyar, M. Utilization of X-band radar information for lahar early warning system (EWS) at Mount Merapi. Satreps Workshop in Kyoto of "Integrated Study on Mitigation of Multimodal Disasters Caused by Ejection of Volcanic Products", 24-25 October 2016, Kyoto University, p. 28, 2016. Available from: http://www.svo.dpri.kyoto-u.ac.jp/new2/wp-content/uploads/2016/11/AbstractsWorkshop2016.pdf

Muñoz-Salinas, E., Castillo-Rodriguez, M., Manea, V., Manea, M., and Palacios C. Lahar flow Simulations using LAHARZ program: Application for the Popocatépetl volcano, Mexico. J. Volcanol. Geoth. Res. Vol.182, pp.13-22, 2009.

Nagata, K., Hasan, M., Otani, K., Takeshi, W., Mizuno, N. Debris flow sediment discharge at the volcanic area of Mt. Merapi in Indonesia, 2003.

Nakagawa, H., Takahashi, T., Satofuka, Y., Kawaike, K.. Numerical simulation of sediment disasters causes by heavy rainfall in Camuri Grande basin, Venezuela. In: Rickenmann, D., Chen, C. (Eds.), Proceedings of the 3rd Conference on Debris-Flow, 2003

Nakano T. Natural hazards: report from Japan. In: White GW (ed) Natural hazards: local, regional, global. Oxford University Press, Oxford, pp. 231–243, 1974.

Nakatani, K.,Wada, T., Matsumoto, Y., Satofuka, Y., Mizuyama, T. Development and Application of GUI Equipped 1-D and 2-D Debris Flow Simulator, applied to Mixed-Size Grains. Ital. J. Eng. Geol. Eniviron. Vol.3, pp.735-743, 2011

Nakatani, K., Iwanami, E., Shigeo, H., Satofuka, Y., Mizuyama, T. Development of "Hyper KANAKO", a debris flow simulation system based on laser profiler data. In: 12th Congress INTERPRAEVENT, Grenobel, France, Conference Proceedings, 2012 Available from. http://www.interpraevent.at/palm-cms/uploadfiles/Publikationen/Tagungsbeitraege/2012_1_269.pdf.

Nakaya, K., Toyoda, Y. Comparison of the compact Doppler radar rain gauge and optical disdrometer. J. Agric. Meteorol. 67 (3), pp. 199–204, 2011. http://dx.doi.org/10.2480/agrmet.67.3.12.

Neall, V.E.. Lahar as major geological hazards. Bull. Int. Assoc. Eng. Geol 14, pp. 233–240, 1976. http://dx.doi.org/10.1007/BF02634799.

Nikolopaulos, E.I., Crema, S., Marchi, L., Marra, F., Guzzetti, F., Borga., M. Impact of uncertainty in rainfall estimation on the identification of rainfall thresholds for debris-flow occurrence. Geomorphology 221, pp. 286–297, 2014. http://dx.doi.org/10.1016/j.geomorph.2014.06.015.

O'Brien, J.S. "Physical Process, rheology and modelling of mudflows". Ph.D Dissertation, Colorado State University., at Fort Collins, CO, 1986.

O'Brien, J.S., Julien, P.Y. Laboratory analysis of mudflow properties. J/Hydr. Eng. ASCE, 114(8), pp. 877-887, 1988.

Over, T.M., Murphy, E.A., Ortel, T.W., Ishii, A.L. Comparisons between NEXRAD radar and tipping-bucket gage rainfall data: a case study for DuPage county. In:Illinois. Conference Paper on: World Environmental and Water Resources Congress, 2007. http://dx.doi.org/10.1061/40927(243)274.

Pallister, J.S., Schneider, D.J., Griswold, J.P., Keeler, R.H., Burton, W.C., Noyles, C., Newhall, C.G. Merapi 2010 eruption—chronology and extrusion rates monitored with satellite radar and used in eruption forecasting. J. Volcanol. Geotherm. Res. 261, pp. 1–9, 2012 http://dx.doi.org/10.1016/j.jvolgeores.2012.07.012.

Palmer, T.N., Zanna., L Singular Vectors, Predictability and Ensemble Forecasting for Weather and Climate, J. Phys., 46, 2013, 254018.

Park,S.G., Bringi, V.N., Chandrasekar, V., Maki, M, Iwanami, K. Correction of radar reflectivity and differential reflectivity for rain reflectivity for rain Attenuation at X band: Part I: Theoretical and Empirical Basis. Journal of Atmospheric and Oceanic Technology. Vol. 22, pp.1621-1631, 2005. https://dx.doi.org/10.1175/JTECH1803.1.

Pasuto, A., Silvano, S. Rainfall as a triggering factor of shallow mass movements. A case study in the Dolomites, Italy. Environ Geol 35(2-3), pp.184-189, 1998

Paul, D., Mandia, R., Sigh, T. Quantifying and modelling of stream network using digital elevation models. Ain Shams Engineering Journal, Vol. 8 (3), pp. 311-321, 2017 https://dx.doi.org19.1016/j.asej.2015.09.002.

Pierson, T.C. Distingushing between debris flows and floods from field evidence in small watersheds. U.S. Geological Survey Fact Sheet 2004-3142, 4, 2005. Available from: https://pubs.usgs.gov/fs/2004/3142/.

Pierson, T.C and Costa, J.E. A Rehologic Classification of subaerial sediment-water flows, in J.E Costa and G.F. Wieczorek (Eds). Debris Flows/Avalanches: Process, Recognition, and Mitigation, Rev. Eng. Geol., vol.7, pp. 1-12, 1987. Geol. Soc. Of Am., Boulder, Colo.

Procter, J.N., Cronin, S.J., Fuller, I.C., Sheridan, M., Neall, V.E, Keys, H., 2010. Hazard assessment using Titan2D for alluvial fan with rapidly changing geomorphology: Whangaehu River. Mt. Ruapehu. J. Geomorph. 116, 162–174. http://dx.doi.org/10.1016/j.geomorph.2009.10.016.

Rice, C. E., Kadavy, K. C., Robinson, K. M. Roughness of loose riprap on steep slopes, J. Hydraul. Eng., 124, pp. 179–185, 1998.

Rickenmann, D., Turowski, J.M., Fritschi, B., Wyss, C., Laronne, J., Barzilai, R., Reid, I., Kreisler, A., Aigner, J., Seitz, H., Habersack, H. Bedload transport measurments with impact plate geophones: comparison of sensor calibration in different gravel-bed stream. Earth surface processes and landforms, 39, pp. 928-942. https://dx.doi.org/10.1002/esp.3499, 2014.

Rickenmann, D., Chen, C.L. Debris Flow Hazards Mitigation: Mechanics, Prediction and Assessement. 2. pp. 671–682, 2003. Available from. http://www.gbv.de/dms/tib-ub-hannover/371015413.pdf.

Rickenmann, D. Empirical Relationships for Debris Flows. Natural Hazards., Vol. 19, pp. 47-77, 1999.

Santi PM, Hewitt K, VanDine DF, Barillas EM. Debris-flow impact, vulnerability, and response. NatHazards 56(1), pp. 371–402, 2010

Sayama, T., Tatebe, Y., Iwami, Y., Tanaka, S. Hydrologic sensitivity of flood runoff and inundation: 2011 Thailand floods in the Chao Phraya River basin, Nat. Hazards Earth Syst., Vol. 15, pp. 1617-1630, 2015.

Scharfenberg, K.A., Miller, D.J., Schuur, T.J., Schlatter, P.T. The joint polarization experiment: Polarimetric radar in forecasting and warning decision-making. Weather and Forecasting, Vo. 20, Iss. 5, pp.775-788, 2005. https://dx.doi.org/10.1175/WAF881.1.

Schneider, D., Delgado Granados, H., Huggel, C., Kääb, A. Modeling Potential Laharic Hazards Related to Ice-Melting in Case of Unrest of Iztaccíhuatl Volcano (Central Mexico). EGU Geophysical Research Abstracts, Vol. 8, 2006

Schuster RL, Salcedo DA, Valenzuela L. Overview of catastrophic landslides of South America in the twentieth century. In: Evans SG, DeGraff JV (eds). Catastrophic landslides: effects, occurrence, and mechanisms. Reviews in engineering geology. Geological Society of America, Boulder, pp 1–34, 2002.

Schuster, R.L., and Crandell, D.R, Catastrophic debris avalanches from volcanoes, in International Symposium on Landslides, 4th, Toronto, Canada, Proceedings: v. 1, p. 567-572, 1984.

Scrivenor J.B, The mudstreams (lahars) of Gunung Keloet in Java. Geol. Mag. 66, 433–434, 1929.

Segond, M., Wheater, H.S., Onof, C. The significance of spatial rainfall representation for flood runoff estimation: A numerical evaluation based on the Lee catchment, UK. J Hydrol., 347, pp. 116–131, 2007.. https://doi.org/10.1016/j.jhydrol.2007.09.040

Selby, M. Hillslope materials and processes, 2nd edn, 1993. Oxford University Press, Oxford

Shiiba, M., Takasao, T. & Nakakita, E. Investigation of Short-Term Rainfall Prediction Method by a Translation Model, Jpn. Conf. on Hydraul., 28th, pp. 423-428, 1984.

Simkin, T., Siebert, L. Volcanoes of the world, Geol. Mag., 134(I), pp. 121-142, 1997. http://dx.doi.org/10.1017/S001675689730613.

Shuin, Y., Shibano, H., Suzuki, M., Ohta, T. Temporal and spatial characteristics of rainfall on the southwest slope of Mt. Merapi in Indonesia. Int. J. Erosion Control Eng. 3–12, 1996. http://dx.doi.org/10.11475/sabo1973.48.Special_3.

Staley, D., Kean, J., Cannon, S., Schmidt, K., Laber, J. Objective definition of rainfall intensity–duration thresholds for the initiation of post-fire debris flows in southern California. Landslides 10 (5), pp. 547–562, 2013 http://dx.doi.org/10.1007/s10346-012-0341-9.

Stancanelli, L. M., Lanzoni, S., Foti, E. Propagation and deposition of stony debris flows at channel confluences. Water Resour. Res., 51, pp. 5100–5116, 2015. http://doi.org/10.1002/ 2015WR017116.

Sumaryono, Nakatani, K., Satofuka, Y., Mizuyama, T. One-dimensional numerical simulation for sabo dam planning using Kanako (Ver. 1.40): a case study at Cipanas, Guntur volcanoes, West Java, Indonesia. Int. J. Erosion Control Eng. 2 (1), pp. 22–32, 2009. http://dx.doi.org/10.13101/ijece.2.22.

Sumaryono, A., Hildasari, A. The development of sabo technology to mitigate disaster caused by debris flow in Indonesia. INTERPRAEVENT – Grenoble/france. Conference Proceedings, pp. 910-919, 2010.

Surono, M., Jousset, P., Pallister, J., Boichu, M., Buangiorno, M.F., Budisantoso, A., Rodriguez, F.C., Andreastuti, S., Prata, F., Schneider, D., et al. The 2010 explosive eruption of Java's Merapi volcano—A '100-year' event. J. Volcanol. Geotherm. Res. 241–242 (C), pp. 121–135, 2012. http://dx.doi.org/10.1016/j.jvolgeores.2012.06.018.

Syarifuddin, M., Oishi, S., Hapsari, R.I., Legono, D., and Iguchi., M., Integrating X-MP radar data to estimate rainfall induced debris flow in the Merapi volcanic area. Advances in water resource, Vol. 110, pp. 242-269, 2017.

Syarifuddin, M., Oishi, S., Legono, D. Lahar flow simulation in Merapi Volcanic Area by HyperKANAKO Model. Journal of Japan Society of Civil Engineers, Ser. B1 (Hydraulic Engineering), Vol. 72, No.4, pp.65-70, 2016

Syarifuddin, M., Oishi, S., Pramudia, A., Masria. Predicting Indonesian tropical moonsonal rainfall in west Timor. Journal of Japan Society of Civil Engineers, Ser. B1 (Hydraulic Engineering), Vol. 71, No.4, pp. 91-96, 2015. https://dx.doi.org/10.2208/jscejhe.71.I_91.

Takahashi, T,. Debris Flow: Mechanics, Prediction and Countermeasures, 2$^{nd}$ edition, 2014. Taylor & Francis, London.

Takahashi, T. A review of Japanese debris flow research. Int. J. Erosion Control Eng. 2 (1), pp. 15–21, 2009. http://dx.doi.org/10.13101/ijece.2.1.

Takahashi, T. Mechanics of viscous debris flow. In: Takahashi, T. (Ed.), Japan-China Joint Research On the Mechanism and the Countermeasures For the Viscous Debris Flow. Disaster Prevention Research Institute, Kyoto University, pp. 64–84, 1999.

Takahashi, T. Mechanical characteristics of debris flow, J. Hydr. Eng. Div.-ASCE, 104, pp. 1153–1169, 1978

Takahashi, T., Nakagawa, H, Harada, T., Yamashiki, Y. Routing debris flows with particle segregation. J. Hydraul. Eng-ASCE. 118 (11), 1490–1507, 1992. http://dx.doi.org/10.1061/(ASCE)0733-9429(1992)118:11(1490).

Takahashi, T., Nakagawa, H., Satofuka, Y., Kawaike, K. Flood and sediment disasters triggered by 1999 rainfall in Venezuela; a river restoration plan for alluvial plan. J. Nat. Disaster Sci. 23 (3), pp. 65–82, 2001. Available from. http://www.jsnds.org/jnds/23_2_2.pdf.

Terlien, M.T.J. The determination of statistical and deterministic hydrological landslide-triggering thresholds. Environ Geol 35(2-3), pp. 124–130, 1998.

Tian, S., Zhang, Z. Housing loss estimation study of urban debris flow disaster based on SPOT-5 data, A case study on Dongchuan District, Kunming, Yunnan Province. 2009 Urban Remote Sensing Joint Event, 2009

Tognacca, C., Bezzola, G. R., Minor, H. E. Threshold criterion for debris flow initiation due to channel bed failure, in: Debris-flow hazards Mitigation: Mechanics, Prediction and Assessment, edited by: Wieczoreck, G. F. and Nasser, N. D., A. A. Balkema, Rotterdam, pp. 89–97, 2000

USDA. Urban Hydrology for small watershed, 1984. Available from. https://www.nrcs.usda.gov/Internet/FSE_DOCUMENTS/stelprdb1044171.pdf.

Vallance, J.W. Lahars. In: Sigurdsson, H. et al., (Ed.), Encyclopedia of Volcanoes. Academic Press, San Diego, pp. 601–616, 2000.

Van Bemmelen, R.W. The Geology of Indonesia, vol. I(A). Government Printing Office, The Hague, 732 pp, 1949.

Varnes, D.J. Slope movement types and processes. In: Schuster RL, Krizek RJ (eds) Special report 176: landslides: analysis and control. Transportation Research Board, National Research Council, Washington, pp. 11–33, 1978.

Wang, F., Wu, Y.H., Yang, H., Tanida, Y., Kamei, A. Preliminary investigation of the 20 August 2014 debris flows triggered by a severe rainstorm in Hiroshima City, Japan. Geoenvironmental Disasters, pp. 2-17, 2015. http://doi.org/10.1186/s40677-015-0025-6

Wang, L. and Shao, S. Prediction Method of Debris Flows, INTERPRAEVENT – Grenoble/france. Conference Proceedings, 2000

Waldron, H.H. Debris flow and erosion control problems caused by the ash ruption of Irazu volcano in Costarica. U. S. Geological Survey Bulletin, 1241-I, 1967. Available from: https://pubs.er.usgs.gov/publication/b1241I.

Wardoyo, T.W., Legono, D., Jayadi, R., Fathani, T.F. Analysing sediment transport mechanism and related hydraulic structure damage after Mt. Merapi Eruption Gendol River. J. Basic. Appl. Sci. Res. 3 (1), pp. 849–855, 2013. Available from. https://www.textroad.com/pdf/JBASR/J.%20Basic.%20Appl.%20Sci.%20Res.,%203(1)849-857,%202013.pdf.

Whipple, K.X. Open-channel flow of Bingham fluids: applications in debris flow research. J. Geol. 105 (2), pp. 243–262, 1997. http://dx.doi.org/10.1086/515916.

Wei, K., Gao, P., Cu K.i., Hu, K.,Xu, J., Zhang, G., & Bi, B. Method of Debris Flow Prediction Based on A Numerical Weather Forecast and Its Application, WIT Trans. Ecol. Envir., Vol 90, pp. 37-46, 2006.

Widowati, A.P.A. Sensitivity Analysis of lahar flow simulation as affected by DEM resolutions – case of Kali Putih, Mt. Merapi Area. Satreps Workshop in Kyoto of "Integrated Study on Mitigation of Multimodal Disasters Caused by Ejection of Volcanic Products", 24-25 October, 2016, Kyoto University, p. 28, 2016. Available from: http://www.svo.dpri.kyoto-u.ac.jp/new2/wp-content/uploads/2016/11/AbstractsWorkshop2016.pdf

Wilson, R. C. Normalizing rainfall/debris-flow thresholds along the U. S. Pacific coast for long-term variations in precipitation climate. In Chen, C.L (ed). Proc. of the 1st Int. Conf. On Debris Flow Hazard Mitigation: Mechanics, Prediction, and Assessment. New York: ASCE, pp. 32-43, 1997.

Wu, Y.H., Liu, K.F., Chen, YComparison between FLO-2D and Debris-2D on the application of assessment of granular debris flow hazards with case study. J. Mt. Sci 10 (2), pp. 293–304, 2013. http://dx.doi.org/10.1007/s11629-013-2511-1.

Yulinsa, N. Snake line analysis for lahar flow warning system (Case study in Putih River, Mount Merapi. Journal of the Civil Engineering Forum. Vol.1 No. 1. Pp. 37-42, 2015.

Zanuttigh, B., Lamberti, A. Instability and surge development in debris flows. Rev. Geophys. 45, RG3006, 2007. http://dx.doi.org/10.1029/2005RG000175.

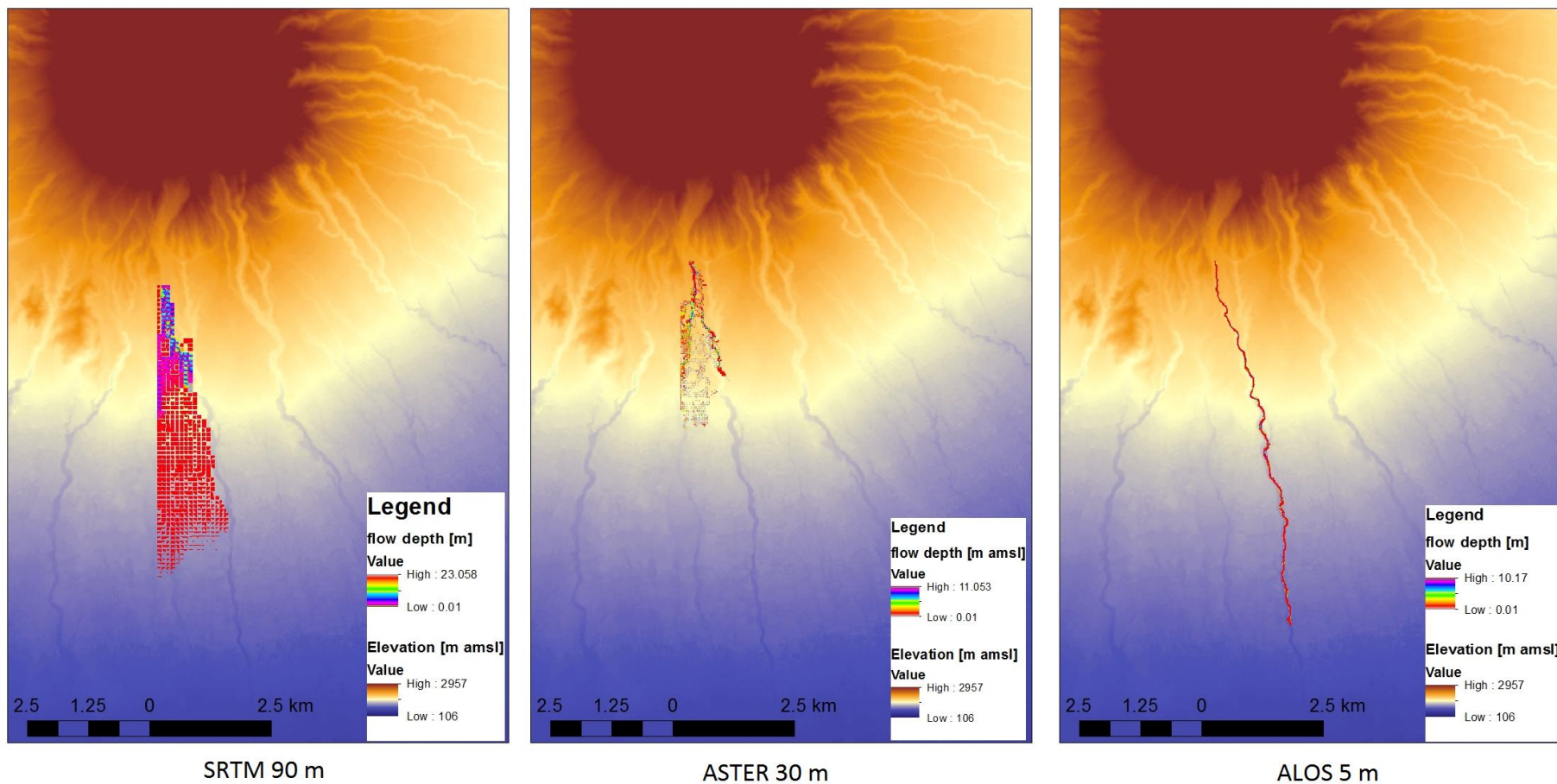# ACKNOWLEDGEMENTS

# The Appendices

1.  Upstream Gendol River Condition
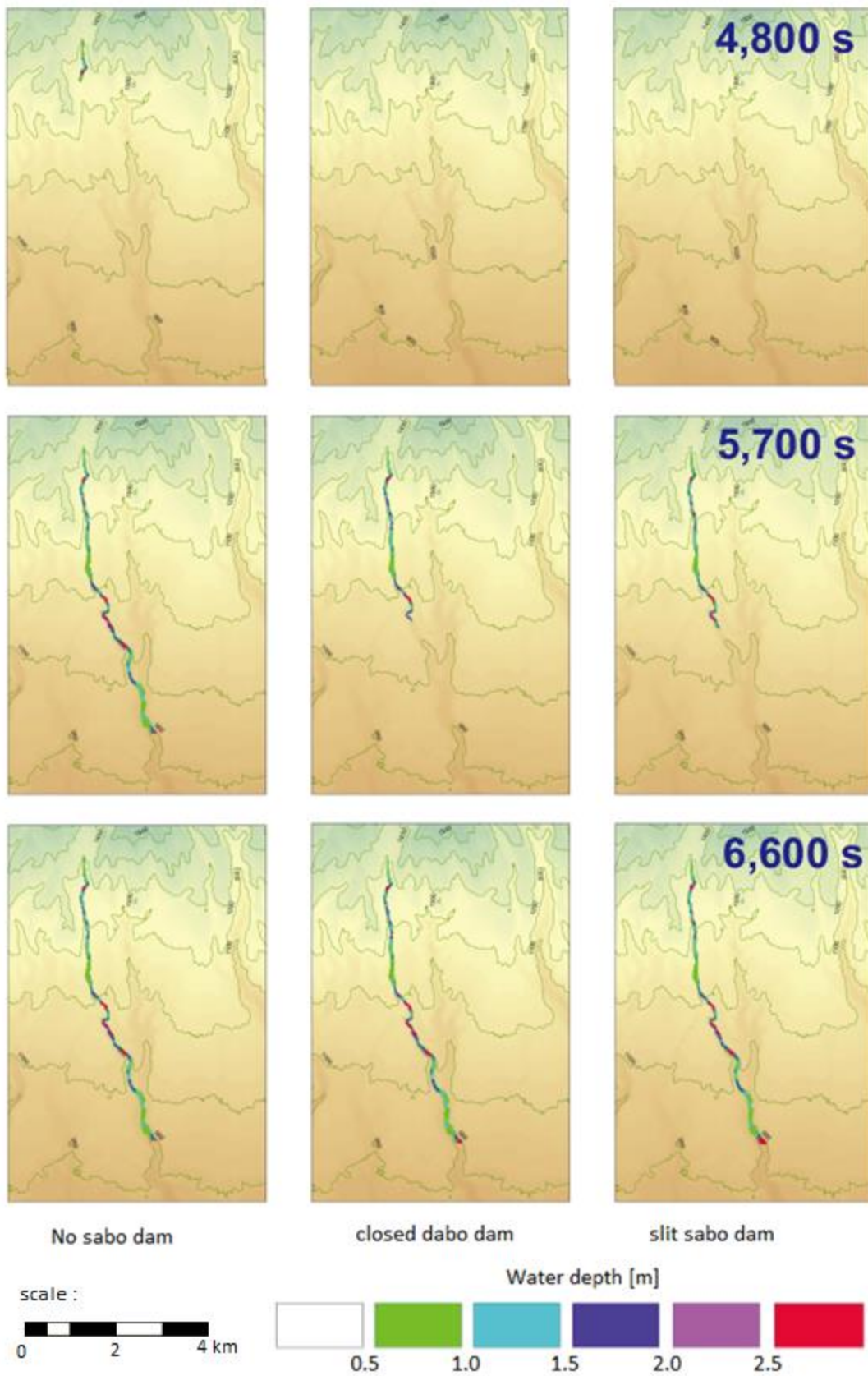




2.  Downstream Gendol River Condition

3. 2D lahar inundation based on DEM resolution (**Chapter III**)



2D lahar inundation simulation results of $R_2$ (15 February 2013)

4. 2D lahar inundation based on sabo dam effect (Chapter IV)



No sabo dam          closed dabo dam          slit sabo dam

scale :

0          2          4 km
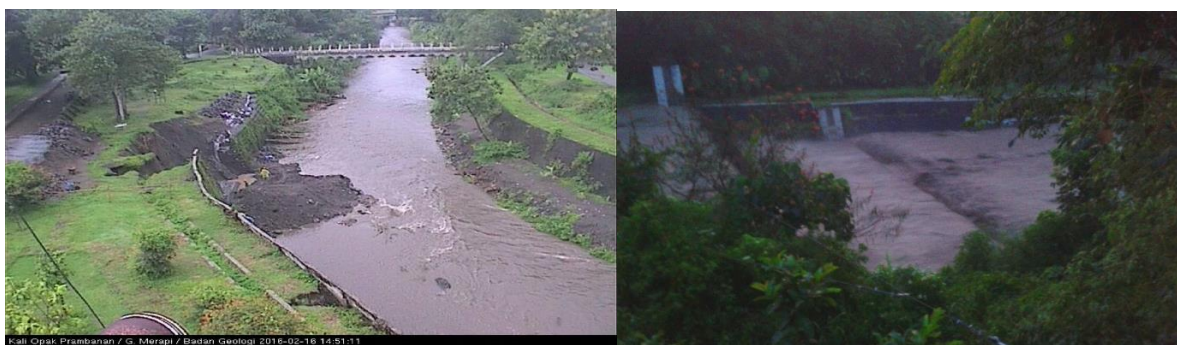
Water depth [m]

0.5    1.0    1.5    2.0    2.5

5. Documentations of Lahar Event on 17 February 2016 from BPPTKG (CVHGM) twitter account


View from 15 CCTV installed at Mt. Merapi on 17 February 2016


Upstream Woro River view captured by CCTV



View of Opak River near Prambanan area from two points observation on 17 February 2016

View of Gendol River at Bronggang sabo dam on 17 February 2016


View of Putih River captured by CCTV, negative lahar occurrence was reported


Seismograph at upstream Mt. Merapi shows increasing rainfall intensity on 17 February 2016

6. Statistical Analysis of Short Term Rainfall Prediction

T-test analysis summary of Short-term rainfall prediction in Gendol catchment assuming equal variance

| Ensemble parameters | Mean | Variance | $T_{critical}$ | $t_{stat}$ | $P (T \leq t)$ |
|---|---|---|---|---|---|
| Lag-2 | 3.32 | 28.32 | 1.68 | 0.61 | 0.27 |
| Lag-4 | 3.95 | 34.09 | 1.68 | 0.28 | 0.39 |
| Lag-6 | 5.05 | 34.88 | 1.68 | -0.26 | 0.39 |
| SV+2 | 4.56 | 47.58 | 1.68 | -0.02 | 0.49 |
| SV+1 | 3.01 | 34.58 | 1.68 | 0.74 | 0.23 |
| SV0 | 5.41 | 55.92 | 1.68 | -0.39 | 1.68 |
| SV-2 | 3.52 | 21.18 | 1.68 | 0.54 | 0.29 |
| SV-1 | 4.73 | 28.99 | 1.68 | -0.11 | 0.46 |

T-test analysis summary of Short-term rainfall prediction in Putih catchment assuming equal variance

| Ensemble parameters | Mean | Variance | $T_{critical}$ | $t_{stat}$ | $P (T \leq t)$ |
|---|---|---|---|---|---|
| Lag-2 | 3.97 | 3.61 | 1.68 | -3.50 | 0.000 |
| Lag-4 | 2.24 | 5.89 | 1.68 | -0.58 | 0.28 |
| Lag-6 | 2.44 | 5.19 | 1.68 | -0.91 | 0.18 |
| SV+2 | 4.36 | 21.66 | 1.68 | -2.28 | 0.01 |
| SV+1 | 2.55 | 3.56 | 1.68 | -1.08 | 0.122 |
| SV0 | 3.06 | 0.82 | 1.68 | -2.51 | 0.008 |
| SV-2 | 2.06 | 6.60 | 1.68 | -0.33 | 0.37 |
| SV-1 | 2.60 | 8.01 | 1.68 | -1.01 | 0.15 |

Regression analysis summary of Short-term rainfall prediction in Gendol catchment

| Ensemble parameters | $R^2$ | Intercept | Constant | F | P |
|---|---|---|---|---|---|
| Lag-2 | 0.97 | 0.14 | 1.32 | 297.49 | 0.00 |
| Lag-4 | 0.94 | -0.16 | 1.18 | 297.48 | 0.00 |
| Lag-6 | 0.85 | -1.11 | 1.11 | 106.9 | 0.00 |
| SV+2 | 0.95 | -0.08 | 1.00 | 367.03 | 0.00 |
| SV+1 | 0.92 | 1.02 | 1.17 | 210.85 | 0.00 |
| SV0 | 0.92 | -0.43 | 0.91 | 213.43 | 0.00 |
| SV-2 | 0.77 | -0.26 | 1.35 | 62.7 | 0.00 |
| SV-1 | 0.64 | -0.50 | 1.06 | 33.76 | 0.00 |

Regression analysis summary of Short-term rainfall prediction in Putih catchment

| Ensemble parameters | $R^2$ | Intercept | Constant | F | P |
|---|---|---|---|---|---|
| Lag-2 | 0.33 | -0.65 | 0.65 | 9.49 | 0.00 |
| Lag-4 | 0.52 | 0.46 | 0.61 | 20.57 | 0.00 |
| Lag-6 | 0.66 | 0.03 | 0.73 | 37.57 | 0.00 |
| SV+2 | 0.29 | 0.77 | 0.24 | 8.01 | 0.01 |
| SV+1 | 0.29 | 0.32 | 0.59 | 7.97 | 0.01 |
| SV0 | 0.20 | -1.33 | 1.03 | 4.95 | 0.03 |
| SV-2 | 0.45 | 0.72 | 0.53 | 15.54 | 0.00 |
| SV-1 | 0.52 | 0.46 | 0.52 | 20.76 | 0.00 |

Doctoral Dissertation, Kobe University
Development of remote monitoring system of rainfall-induced lahar at Mount Merapi, 138 pages
Submitted on January, 18 2018
The date of publication is printed in cover of repository version published in Kobe University
Repository Kernel.